ดีไฮเดรชัน และ ออกซิเดทีพดีไฮโดรจิเนชันของเอทนอลบนตัวเร่งปฏิกิริยาอะลูมินาที่ถูกปรับปรุงด้วยซิลเวอร์ลิเทียม

นายจักรพันธ์ จันละมูล

วิทยานิพนธ์นี้เป็นส่วนหนึ่งของการศึกษาตามหลักสูตรปริญญาวิศวกรรมศาสตรดุษฎีบัณฑิต
สาขาวิชาวิศวกรรมเคมี ภาควิชาวิศวกรรมเคมี
คณะวิศวกรรมศาสตร์ จุฬาลงกรณ์มหาวิทยาลัย
ปีการศึกษา 2557

DEHYDRATION AND OXIDATIVE DEHYDROGENATION OF ETHANOL OVER ALUMINA CATALYST MODIFIED WITH SILVER-LITHIUM

Mr. Jakrapan Janlamool

A Dissertation Submitted in Partial Fulfillment of the Requirements
for the Degree of Doctor of Engineering Program in Chemical Engineering
Department of Chemical Engineering
Faculty of Engineering
Chulalongkorn University
Academic Year 2014

Thesis Title	DEHYDRATION AND OXIDATIVE DEHYDROGENATION OF ETHANOL OVER ALUMINA CATALYST MODIFIED WITH SILVER-LITHIUM
By	Mr. Jakrapan Janlamool
Field of Study	Chemical Engineering
Thesis Advisor	Associate Professor Bunjerd Jongsomjit, Ph.D.

Accepted by the Faculty of Engineering, Chulalongkorn University in Partial Fulfillment of the Requirements for the Doctoral Degree

.....Dean of the Faculty of Engineering
(Professor Bundhit Eua-arporn, Ph.D.)

THESIS COMMITTEE

.....Chairman
(Varun Taepaisitphongse, Ph.D.)

.....Thesis Advisor
(Associate Professor Bunjerd Jongsomjit, Ph.D.)

.....Examiner
(Associate Professor Seeroong Prichanont, Ph.D.)

.....Examiner
(Chutimon Satirapipathkul, D.Eng.)

.....External Examiner
(Ekrachan Chaichana, D.Eng.)

จักรพันธ์ จันละมูล : ดีไฮเดรชัน และ ออกซิเดทีพดีไฮโดรจิเนชันของเอทนอลบนตัวเร่งปฏิกิริยาอะลูมินาที่ถูกปรับปรุงด้วยซิลเวอร์ลิเทียม (DEHYDRATION AND OXIDATIVE DEHYDROGENATION OF ETHANOL OVER ALUMINA CATALYST MODIFIED WITH SILVER-LITHIUM) อ.ที่ปรึกษาวิทยานิพนธ์หลัก: รศ. ดร.บรรเจิด จงสมจิตร, 97 หน้า.

งานวิจัยนี้มีวัตถุประสงค์เพื่อศึกษาคุณลักษณะและความว่องไวของตัวเร่งปฏิกิริยาอะลูมินาวัฏภาคผสมและตัวเร่งปฏิกิริยาอะลูมินาวัฏภาคผสมที่ถูกปรับปรุงด้วยซิลเวอร์ลิเทียม ในส่วนแรกของงานปฏิกิริยาดีไฮเดรชันของเอทานอลบนตัวเร่งปฏิกิริยาวัฏภาคผสมถูกนำมาศึกษา ตัวเร่งปฏิกิริยาวัฏภาคผสมขอแกมมา และไคของอะลูมินาที่ถูกเตรียมโดย วิธีโซลโวเทอร์มอลของสารละลายผสม (โทลูอีนและบิวทานอล) แสดงคุณสมบัติที่น่าสนใจทางเคมีและกายภาพสำหรับปฏิกิริยาดีไฮเดรชันของเอทานอลเป็นเอทิลีน ความหนา แน่นของตำแหน่งกรดที่มากส่งผลอย่างเห็นได้ชัดเจนต่อความว่องไวของปฏิกิริยาสำหรับตัวเร่งปฏิกิริยาวัฏภาคผสมของแกมมาและไคด้วยอัตราส่วน 50 เปอรเซ็นต์โดยน้ำหนัก (CHI50) นอกจากนี้ ปริมาณที่มากของน้ำที่ถูกดูดซับบนพื้นผิวของอะลูมินาส่งผลต่อการเพิ่มขึ้นของค่าการเลือกเกิดเป็นเอทิลีนสังเกตุได้จากสเปคโตรสโคปีของอนุภาคอิเล็กตรอนที่ถูกปลดปล่อยด้วยรังสีเอกซ์ (XPS) ในส่วนที่สองของงานผลกระทบของการปรับปรุงด้วยซิลเวอร์ลิเทียมบนอะลูมินาวัฏภาคผสมถูกนำมาศึกษาโดยปฏิกิริยาออกซิเดทีฟดีไฮโดรจิเนชันของเอทานอลเป็นแอซี*ทัลดีไฮด์* ผลการทดลองพบว่าค่าความว่องไวของปฏิกิริยาและค่าการเลือกเกิดเป็นแอซี*ทัลดีไฮด์*ที่สูงสำหรับตัวเร่งปฏิกิริยาที่ปรับปรุงด้วยซิลเวอร์ลิเทียมบนอะลูมินาวัฏภาคผสมของแกมมาและไคด้วยอัตราส่วน 50 เปอรเซ็นต์โดยน้ำหนัก (AgLi-CHI50) สอดคล้องกับสภาวะออกซิเดชันและพฤติกรรมการรีดักชัน นอกเหนือจากนี้เพื่อศึกษาความว่องไวของลักษณะพื้นผิวบนตัวเร่งปฏิกิริยาซิลเวอร์การดูดซับของน้ำบนระดับขั้นอะตอมชนิด A และ B บนโลหะซิลเวอร์ผลึกเดี่ยวโดยการคายน้ำด้วยการเพิ่มอุณหภูมิแบบตั้งโปรแกรมถูกนำมาศึกษา โลหะซิลเวอร์ผลึกเดี่ยวแบบผิวโค้งแสดงช่วงต่อเนื่องของโครงสร้างพื้นผิวตั้งแต่ [5(111)x(100)] ผ่าน (111) ไปยัง [5(111)x(110)] การเลี้ยวเบนของ*อิเล็กตรอนพลังงานต่ำ (LEED)* และ กล้องจุลทรรศน์แบบส่องกราดในอุโมงค์ (STM) สามารถตรวจสอบผิวโค้งของตัวอย่างส่วนใหญ่เป็นระดับขั้นหนึ่งอะตอม สำหรับการดูดซับแบบน้อยกว่าหนึ่งชั้น (submonolayer) ของปริมาณน้ำที่ปกคลุมพบว่าขนาดเล็กและเชิงเส้นของอุณหภูมิการคายซับที่ A และ B มีความหนาแน่นขั้นอะตอมที่ถูกสังเกตุ

ภาควิชา วิศวกรรมเคมี ลายมือชื่อนิสิต .....

สาขาวิชา วิศวกรรมเคมี ลายมือชื่อ อ.ที่ปรึกษาหลัก .....

ปีการศึกษา 2557

5371830921 : MAJOR CHEMICAL ENGINEERING
KEYWORDS: ETHANOL / DEHYDRATION / OXYDATIVE DEHYDROGENATION / SILVER / MIXED PHASE ALUMINA

JAKRAPAN JANLAMOOL: DEHYDRATION AND OXIDATIVE DEHYDROGENATION OF ETHANOL OVER ALUMINA CATALYST MODIFIED WITH SILVER-LITHIUM. ADVISOR: ASSOC. PROF. BUNJERD JONGSOMJIT, Ph.D., 97 pp.

The research was aimed to investigate the characteristic and catalytic properties of mixed-phase alumina catalysts and Ag/Li modified mixed-phase alumina catalysts. In the first part, ethanol dehydration over mixed-phase alumina catalysts was investigated. The mixed gamma and chi phase alumina prepared by the solvothermal method of the mixed solution (toluene and 1-butanol) displays the attractive chemical and physical properties for the catalytic dehydration of ethanol to ethylene. The high acid site density apparently results in high catalytic activity for the mixed γ- and χ-alumina with 50 wt% of γ- and χ phases (CHI50). Moreover, the large amount of the adsorbed water on alumina surface can result in increased ethylene selectivity as observed by XPS analysis. In the second part, the influences of Ag/Li modification on mixed-phase alumina was investigated for oxidative dehydrogenation of ethanol to acetaldehyde. The result shows that high catalytic activity and acetaldehyde selectivity for Ag/Li modified the mixed γ- and χ- alumina with 50 wt% of γ- and χ phases (AgLi-CHI50) corresponded to the oxidation state and reduction behavior. In addition, in order to investigate surface-structure sensitive on silver catalyst, the adsorption of H_2O onto the A and B type steps on an Ag single crystal by temperature programmed desorption was studied. A silver curved crystal represents a continuous range of surfaces structures ranging from [5(111)x(100)] via (111) to [5(111)x(110)]. LEED and STM studies verify that the curvature of sample results predominantly from monoatomic steps. For submonolayer of H_2O coverage, a small and linear dependence of the desorption temperature on the A and B step density were observed.

Department:	Chemical Engineering	Student's Signature	.....
Field of Study:	Chemical Engineering	Advisor's Signature	.....
Academic Year:	2014		

ACKNOWLEDGEMENTS

The author would like to express his greatest gratitude and appreciation to his advisor, Assoc. Prof. Dr. Bunjerd Jongsomjit for his invaluable guidance, providing kind supervision throughout this study. Moreover, he also would like to express his greatest gratitude and appreciation to Assistant Professor Dr. Ludo B.F. Juurlink from Leiden Institute of Chemistry, Leiden University, Netherlands for his invaluable guidance and his kind supervision throughout research internship.

In addition, the author is also grateful to Dr. Varun Taepaisitphongse, as the chairman, Associate Professor Seeroong Prichanont, Dr. Chutimon Satirapipathkul and Dr. Ekrachan Chaichana as the members of the thesis committee.

The author would like to thank the Royal Golden Jubilee Ph.D. scholarship from the Thailand Research Fund (TRF) and Office of the Higher Education Commission (CHE), National Research University (WCU-029-AM-57) and the National Research Council of Thailand (NRCT) for the financial support of this project.

Many thanks for kind suggestions and useful help to, Dr. Wanna Phiwkliang, Mr. Narongrat Poovarawan and many friends in the laboratory who always provide the encouragement and co-operate through the dissertation study. Moreover, the author would like to thanks for kind suggestions and useful help to Mr. Cansin Badan, Miss Angela den Dunnen and co-operate during the research internship in catalysis and surface chemistry laboratory at Leiden Institute of Chemistry, Leiden University, Netherlands.

Most of all, the author would like to express his highest gratitude to his parents who always pay attention to him all the times and for suggestions, support and encouragement.

CONTENTS

Page

Page

LIST OF TABLES

LIST OF FIGURES

CHAPTER I
INTRODUCTION

1.1 Introduction

Bio-ethanol, which is produced by fermentation of main sources such as bagasse from sugar cane and starch from maize, is an attractive alternative feedstock. The reaction of bio-ethanol which has been increasingly received more attention has many important technological applications. Bio-ethanol can be used to synthesize many chemical intermediates such as ethylene, diethyl ether, acetaldehyde, ethyl acetate and acetic acid.

Ethanol conversion can be acid and base catalyzed, therefore the selectivity to a desired product can be easily related to the characteristic of the catalyst surface [1]. In a number of papers, it was observed that the acidity over solid catalysts predominantly played an important role on alcoholic dehydration [2]. The alumina catalysts led predominantly to the formation of ethylene and diethyl ether with minor amount of acetaldehyde. Ethanol has been dehydrated through intramolecular route to produce ethylene or through intermolecular pathway to generate diethyl ether (DEE) [3]. The relationship between the acid sites on the catalyst and catalytic activity has been investigated. Nowadays, the widely used catalysts in this application is still γ-Al_2O_3 [3-5], and other catalysts such as zeolite [6, 7], heteropolyacid [8], transition metal oxides [9-11], acid carbon [1] have also been developed. On the contrary, the basic catalysts took place to produce acetaldehyde by dehydrogenation of ethanol [12]. The formation of acetaldehyde displayed the presence of redox sites on the catalyst [13]. The oxidative dehydrogenation of ethanol to acetaldehyde has been performed on the various basic catalysts such as V_2O_5 [14], graphite nanofibers [15], Ag-Al_2O_3 and Cu-Al_2O_3 [16], Au-Al_2O_3 [17].

Recently, the advanced solid materials, which were introduced into nanoscale possessed the attractive structures. The nanoscale HZSM-5 zeolite catalyst represents better catalytic stability and selectivity for ethylene than microscale HZSM-5 zeolite catalyst [18]. In addition, the nanocrystalline γ-Al_2O_3 has been well known as a

bifunctional oxide comprising acidic and basic sites [19]. It is one of the most widely used a inert carrier of metal catalysts in heterogeneous catalysis because of its fine particle size, high surface area, surface catalytic activity, high mechanical resistance, excellent thermal stability, and wide range of chemical, physical, and catalytic properties [20-22]. Besides the role of the surface area, the pore structure plays the important function in the catalytic activity. Several studies attempt to synthesize alumina that has uniform mesoporous distribution. The nanocrystalline Al_2O_3 has been generally synthesized by sol-gel [23], precipitation [24], flame spray pyrolysis [25] and solvothermal [20-22] methods. The solvothermal synthesis attracts the most attention because this application gives the products with nanoscale uniform morphology, homogeneous chemical composition, and narrow size distribution [26-30].

Nanocrystalline Al_2O_3 with mixed γ- and χ-crystalline phases prepared from the thermal decomposition of aluminium isopropoxide (AIP) in organic solvent has high thermal stability [22-24]. Nanocrystalline χ-Al_2O_3 is one of the metastable polymorphs based on hexagonal close packing (hcp) of the oxygen atom [20, 21]. The previous studies showed that highly stable nanocrystalline Al_2O_3 with mixed γ- and χ-crystalline phases prepared by the solvothermal method exhibited interesting results. It can be employed as catalyst and catalyst supports in many catalytic reactions such as DME synthesis [31], CO hydrogenation [21, 32], CO oxidation [22], and propane oxidation [33].

The goal of this research was to exhibit the effects of the nanocrystalline alumina with mixed γ- and χ-crystalline phases for catalytic behaviors via ethanol dehydration. The mixed γ- and χ-crystalline phase alumina such as CHI00, CHI30, CHI50 and CHI100 were prepared by the solvothermal method. Moreover, the influences of Ag/Li modification on nanocrystalline alumina for oxidative dehydrogenation of ethanol was investigated. The catalyst samples were prepared and characterized by several techniques, such as BET, XRD, SEM/EDX, TEM, TPR, TGA, NH_3-TPD, CO_2-TPD, and XPS. The obtained results from catalytic behaviors were used to evaluate the role of the different characteristics on the overall reaction activity and product selectivity.

1.2 Motivation

The nanocrystalline γ-Al_2O_3, χ-Al_2O_3 and mixed γ- and χ- Al_2O_3 can exhibit the important properties for dehydration and oxidative dehydrogenation of ethanol. The nanocrystalline γ-Al_2O_3, χ-Al_2O_3 and mixed γ- and χ- Al_2O_3 can be used as the catalysts for the ethylene production via the catalytic dehydration of ethanol and the Ag/Li modification on nanocrystalline alumina attractively produced acetaldehyde via oxidative dehydrogenation of ethanol.

1.3 Objective

The research objective is aimed to investigate the effects of mixed phases nanocrystalline alumina comprising γ- and χ- phases for dehydration and oxidative dehydrogenation of ethanol.

1.4 Research scopes

- Preparation of nanocrystalline γ-Al_2O_3, χ-Al_2O_3 and mixed γ- and χ- Al_2O_3.

- Characterization of nanocrystalline Al_2O_3 samples by BET surface area, X-ray diffraction (XRD), scanning electron microscopy and energy dispersive X-ray spectroscopy (SEM/EDX), X-ray photoelectron spectroscopy (XPS), ammonia temperature programmed desorption (NH_3-TPD).

- Investigation of the catalytic activites of different Al_2O_3 catalyst in catalytics dehydration of ethanol (C_2H_5OH) at the reaction temperature range between 200 to 400^oC and 1 atm total pressure.

- Preparation of supported Ag/Li catalyst on the nanocrystalline γ-Al_2O_3, χ-Al_2O_3 and mixed γ- and χ- Al_2O_3 using the incipient wetness impregnation method.

- Characterization of the Ag/Li catalyst using BET surface area, X-ray diffraction (XRD), carbon dioxide temperature programmed desorption (CO_2-TPD), temperature programmed reduction (TPR), scanning electron microscopy and energy dispersive X-ray spectroscopy (SEM/EDX), inductively coupled plasma-optical

emission spectroscopy (ICP-OES), UV-Vis spectroscopy, X-ray photoelectron spectroscopy (XPS) and transmission electron spectroscopy (TEM).

- Investigation of the catalytic activities of Ag/Li catalyst in catalytic oxidative dehydrogenation of ethanol (C_2H_5OH) at the reaction temperature range between 150 to 400^oC and 1 atm total pressure.

1.5 Benefits

- The nanocrystalline γ-Al_2O_3, χ-Al_2O_3 and mixed γ- and χ- Al_2O_3 catalysts for the production of ethylene via catalytic dehydration of ethanol had been developed.
- The Ag/Li modified mixed γ- and χ- nanocrystalline Al_2O_3 catalysts for via oxidative dehydrogenation of ethanol to acetaldehyde had been developed.
- The obtained catalysts was used as the novel rout for ethanol application.

CHAPTER II
THEORY AND LITERATURE REVIEWS

The dehydration and the oxidative dehydrogenation of alcohols on oxide catalysts have been frequently studied. Generally, alkene is yielded by the dehydration on acidic catalysts, whereas aldehyde and/or ketone is yielded by the oxidative dehydrogenation on basic and/or redox catalysts. The basic knowledge of ethanol dehydration reaction and the oxidative dehydrogenation were reviewed as follows in this chapter.

2.1 Dehydration Reactions

Ethanol consists of hydroxyl group in molecule. It can be dehydrated by using acid catalysts. The hydroxyl group is converted into water molecule. After the water molecule is emitted from ethanol molecule, the hydrocarbon rearranges into ethylene or diethyl ether (DEE) [32]. The reaction temperature ranges between 180 to 500°C in gas and liquid phase [6]. The heat of reaction for ethanol dehydration is shown as follows in equation (2.1) and (2.2)

$$C_2H_5OH \longrightarrow C_2H_4 + H_2O \qquad \Delta H = +44.9 kJ/mol \qquad (2.1)$$

$$2C_2H_5OH \longrightarrow C_2H_5OC_2H_5 + H_2O \qquad \Delta H = -25.1 kJ/mol \qquad (2.2)$$

Equation (2.1) reveals that the reaction of ethanol to ethylene, which requires high temperature, is endothermic reaction, while the reaction of ethanol to DEE, which occurs at the low temperature is exothermic as seen in equation (2.2).

As for the dehydration of ethanol, three reaction mechanisms illustrated in **Figure 2.1** have so far been proposed [34].

According to Mechanism 1 proposed on the basis of an experimental study of Al_2O_3. The ethanol adsorbs on a Brønsted acid site, i.e. a surface hydroxy group, and generates an ethoxy group and water. A β-hydrogen (H_β) of the group then shifts to a neighboring basic site (e.g. oxide ion, O_σ) and ethylene is yielded.

In Mechanism 2, a bond between the α-carbon (C_α) and oxygen of the ethoxy group breaks and ethylene is yielded.

According to Mechanism 3 proposed for the dehydration of Nb supported on SiO_2 by Iwasawa and coworkers [35], H_β of the ethoxy group shifts to the metal ion (M), and a hydroxyl group and ethylene is generated.

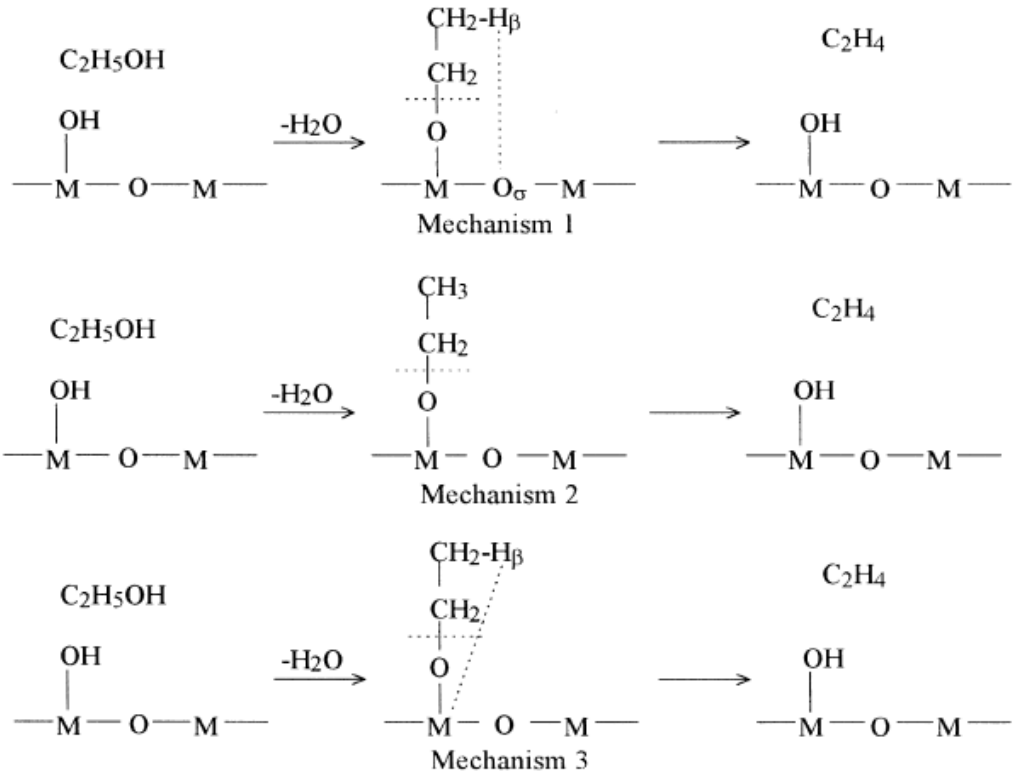

Figure 2.1 A proposed reaction mechanism of dehydration reaction of ethanol [34]

2.2 Oxidative Dehydrogenation Reactions

Oxidation catalysts belong to a wider class of materials having redox or oxidoreductive type characteristics. Presence of a transition metal as the principal active component (V, Mo, Cu, Fe, Pd, Pt, Rh, Ag). Often in these cases, a second element is also present which can be transition or post transition (for example, P, Sb or Bi), which contributes to establishing the reactive characteristics of the catalyst. The mild catalytic oxidation of aliphatic alcohols over simple metal oxides usually leads to the formation of carbonyl compounds. Thus, primary alcohols are selectively oxidized to aldehydes A classic mechanism example of this is the oxidative dehydrogenation of methanol to formaldehyde over the surface molybdenum trioxide are show in **Figure 2.2**. [36]

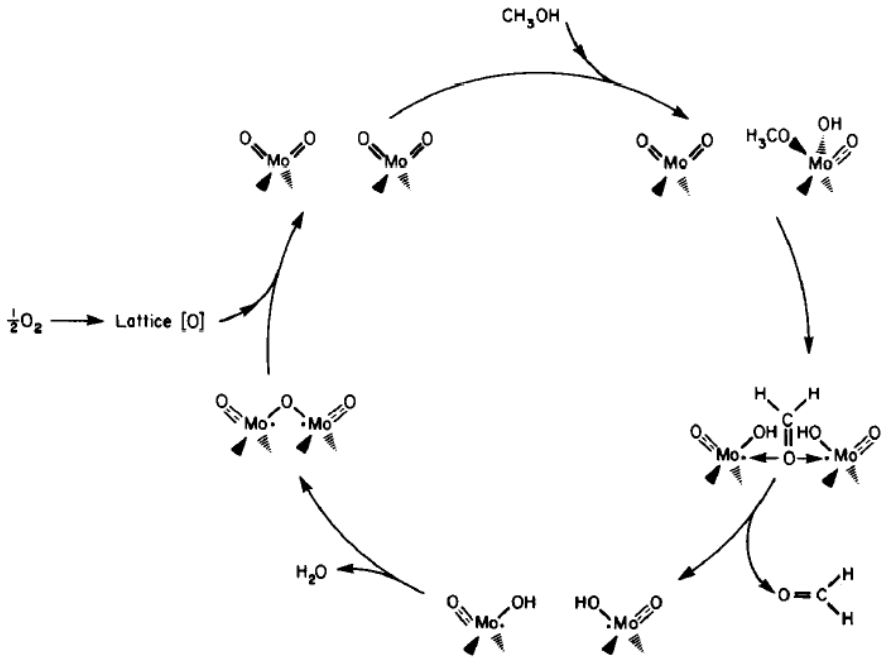

Figure 2.2 A proposed reaction mechanism oxidative dehydrogenation reaction of methanol

An important catalytic site involves two adjacent surface dioxo units (the dual dioxo site), with each dioxo site extracting one H in a sequence of steps. The required dual dioxo site exists on the (010) surface of MoO_3, but does not exist on the other low

index surfaces. This mechanism is supported by atmospheric pressure experimental studies which indicate that MoO_3 (010) is selective for CH_2O products [36].

2.3 Aluminum Oxide

2.3.1 Property of aluminum oxide

The structure of aluminum oxide consists of morphology and crystalline structure. The general form is Al_2O_3. The approximate surface areas are about 100 to 600 m^2/g. These properties depend on the synthesis method, water desorption, impurity and heat treatment. There are many phases of aluminum oxide as remarked with Greek alphabet as follows: beta phase (β-Al_2O_3), gamma phase (γ-Al_2O_3), eta phase (η-Al_2O_3), chi phase (χ-Al_2O_3), kappa phase (κ-Al_2O_3), delta phase (δ-Al_2O_3), theta phase (θ-Al_2O_3) and alpha phase (α-Al_2O_3). Each is a unique crystal structure with specific properties. The phase of aluminum oxide depends on the calcine temperatures of reactant (gibbsite, boehmite, and etc.) [32, 37-39]. For instance, gibbsite is calcined at 280°C to 650°C to obtain chi phase. When it is calcined at 750°C to 1150°C, it obtains the kappa phase alumina. Boehmite is calcined at 480°C to 780°C to obtain the gamma phase. Then, when it was calcined at 780°C to 920°C, it yields the delta phase. The calcined temperature of aluminum hydroxide are shown in **Figure 2.3** [37].

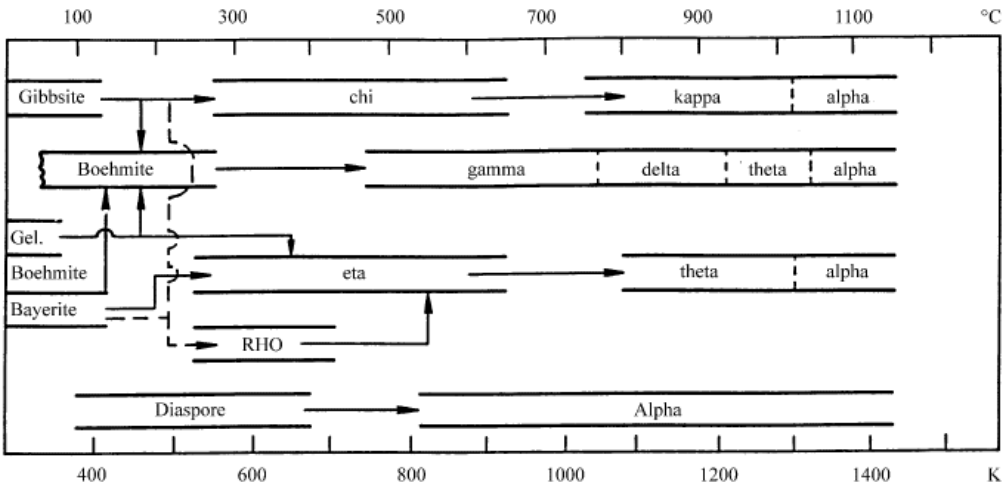

Figure 2.3 The temperature transformation sequence of aluminum hydroxide [37]

The surface of aluminum oxide contains acid and basic sites. The acid site on surface, which is Lewis and Brønsted acid site received from Al^{3+} ion and water molecule coordinated with cation [3], while the basicity on surface is derived from basic hydroxide group and O^{2-} anion [20, 21].

During aluminum oxide contacts with humidity, the water molecule adsorb on surface aluminum oxide and dried in air at temperature between 100°C to 150°C, the water molecule is emitted, but remains hydroxyl group on surface alumina. The role of hydroxyl group is Brønsted acid site as shown in **Figure 2.4**. The acid strength and concentration of aluminum oxide are low when calcined below 300°C, while calcination at 500°C decreases Brønsted acid site. The calcination temperature above 600°C results in adjacent hydroxyl group form into water molecule. Then, the water molecule releases and appears as Al^{3+} ion on surface, which is Lewis acid site [3, 40] as illustrated in **Figure 2.5**.

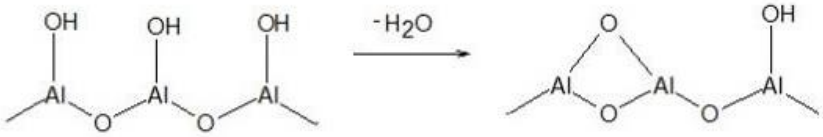

Figure 2.4 Water desorption on surface aluminum oxide

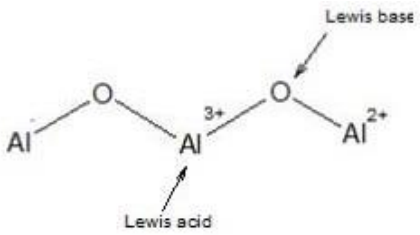

Figure 2.5 Lewis acid site on surface aluminum oxide

2.3.2 Synthesis of Aluminum Oxide: The Solvothermal Method

Aluminum oxide has been generally prepared by various method: sol–gel [41, 42], hydrothermal and sovolthermal methods [20-22, 31]. Usually, aluminum oxide is synthesized by calcination of suitable reactants but this method requires high thermal and it is difficult to control the particle size. The precipitation method is complex and takes long synthesis times (washing times and aging time) [24]. Usually, metal alkoxide was used as precursors to produce aluminum oxide via the sol-gel method [41, 42]. However, the limitation of sol-gel method is long gelation periods and high prices of alkoxide. The hydrothermal is very similar to the solvothermal method. It was different precursor in first step, the aqueous solution used as precursor in the hydrothermal method while the solvothermal method is usually not aqueous (but this is not always) [20, 26, 28].

The “solvothermal” method is a synthesis of inorganic compounds form organic compounds at temperatures between 200°C to 300°C under autogenous pressure of the organics. The suitable organic compounds such as ethanol, 1-butanol, toluene, and etc. were selected. In order to control the structures, grain sizes, shape distribution and morphologies, varied process conditions reaction temperature, reaction time, solvent type and precursor type were considered. The prefix “solvo-” means any type of solvent for example alcohol is used as the reaction media, the reactions is called “alcohothermal” reactions.

Generally, the definition of the solvothermal method is reactions at temperatures higher than the boiling point of the intermediary in liquid or supercritical media. The reaction is carried out in closed system using autoclaves, an apparatus shown in **Figure 2.6**.

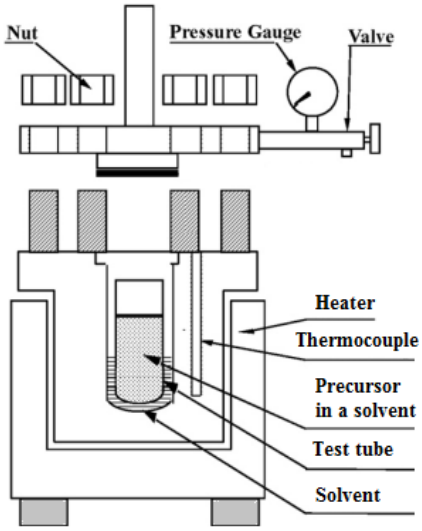

Figure 2.6 Autoclave reactor for solvothermal method**.** [20, 28, 29]

2.4 Silver (I) Oxide

Silver (II) Oxide (AgO) is a highly insoluble thermally stable Silver source suitable for glass, optic and ceramic applications. Silver oxide is a photosensetive fine black powder that decomposes above 280 °. Oxide compounds are not conductive to electricity. However, certain perovskite structured oxides are electronically conductive finding application in the cathode of solid oxide fuel cells and oxygen generation systems. They are compounds containing at least one oxygen anion and one metallic cation. They are typically insoluble in aqueous solutions (water) and extremely stable making them useful in ceramic structures as simple as producing clay bowls to advanced electronics and in light weight structural components in aerospace and electrochemical applications such as fuel cells in which they exhibit ionic conductivity. Metal oxide compounds are basic anhydrides and can therefore react with acids and with strong reducing agents in redox reactions. Silver Oxide is also available in pellets, pieces, powder, sputtering targets, tablets, and nanopowder (from American Elements' nanoscale production facilities).

2.5 Literature Reviews

The most heterogeneous catalysts are solids that react with substrates in a liquid or gaseous reaction mixture. Diverse mechanisms for reactions on surfaces are well known, depending on how the adsorption step takes place. Many industrial catalysts are metals and the simple single crystals provide an introduction to the more atomic metal structures used in industrial catalysts. The typical supports of the catalysts are robust porous solids, including metal oxides, such as alumina, zirconia, silica and carbon.

This chapter reviewed the works on the catalysts for catalytic dehydration and oxidative dehydrogenation reaction of alcohol that is also of great interest in the field of heterogeneous catalysis while it has been used for many catalytic application.

2.5.1 Catalysts in dehydration of alcohol

Dehydration of methanol to dimethyl ether (C_2H_6O, DME) was investigated over a wide range of nanocrystalline Al_2O_3 with mixed γ- and χ- crystalline phases. It was found that the mixed γ- and χ- Al_2O_3 catalyst containing 20 wt% of χ-phase exhibited the highest yield (86 mole%) with good stability for DME synthesis [31]. The HZSM-5 zeolite was also used as a catalyst in the ethanol dehydration reaction. When compared HZSM-5 with gamma alumina, it rendered higher selectivity of ethylene and ethanol conversion than gamma alumina, while the lower reaction temperature than gamma alumina [43-45] was required.

Ethylene production via catalytic dehydration of ethanol over TiO_2/γ-Al_2O_3 catalysts in multi-microchannel reactors is reported. The reaction results indicated that the catalysts doped with TiO_2 have high ethanol conversion of 99.96 mole% and ethylene selectivity of 99.4 mole%. Ethylene yield of 26 g/(gcat h) can be achieved and provided a very favorable foundation for the process intensification and miniaturization of the ethylene production process using bioethanol [46].

Furthermore, TiO_2/4A zeolite composite catalysts were prepared by coating TiO_2 on 4A zeolite via liquid phase deposition. The TiO_2/4A zeolite composite catalysts with higher surface weak acidity and lower modulate strong acidity exhibited much better catalytic performance on ethanol dehydration to ethylene compared with 4A zeolite. It was suggested that the TiO_2 promoter could improve the effective Lewis

acidity of composite catalyst which consequently enhanced the catalytic performance [47].

The TiO_2-supported zeolite with core/shell heterostructure was fabricated by coating aluminosilicate zeolite (ASZ) on the TiO_2 inoculating seed via in situ hydrothermal synthesis. It showed that the TiO_2-supported zeolite composite catalyst with heterostructure core/shell exhibited prominent conversion efficiency for ethanol dehydration to ethylene [48].

The catalytic dehydration of ethanol into ethylene was studied over HZSM-5, phosphorous modified HZSM-5 and lanthanum–phosphorous modified HZSM-5 in the low temperature range from 473 K to 573 K. The experimental results demonstrated the lanthanum–phosphorous modified HZSM-5 offered the outstanding catalytic performance and the enhanced anti-coking ability markedly, especially for 0.5 wt%La-2 wt%PHZSM-5 [49].

Dehydration reaction of ethanol was investigated in a temperature range of 140–250 ^{o}C with three different heteropolyacid catalysts, namely tungstophosphoric acid (TPA), silicotungsticacid (STA) and molybdophosphoricacid (MPA). Very high ethylene yields over 75 mole% obtained at 250 ^{o}C with TPA was highly promising. At temperatures lower than 180 ^{o}C the main product was diethyl-ether. Presence of water vapor was shown to cause some decrease of catalyst activity. The product selectivities did not change much with the space time in the reactor indicated two parallel routes for the production of ethylene and DEE. Among the three HPA catalysts, the activity trend was obtained as STA>TPA>MPA [8].

The efficiency of montmorillonite (K-10) and dodecatungestophosphoric acid (DTPA) supported on montmorillonite (DTPA/K-10), had been evaluated in the dehydration of dilute bio-ethanol (80%m/m). The dehydration of ethanol and cracking of diethyl ether were studied independently. It was found that 30%DTPA/K-10 more active with 74 mole% ethanol conversion and 92 mole% ethylene selectivity at 250 °C in comparison with other acid catalysts used. The mechanism of the dehydration of ethanol reaction suggested that two types of sites were responsible. The dehydration of ethanol and cracking of diethyl ether were second order reactions with weak adsorption of species [50].

2.5.2 Catalysts in oxidative dehydrogenation of alcohol

The oxidative dehydrogenation of alcohols to aldehydes and ketones by heterogeneously catalyzed routes still presents a great challenge in the fine chemical industry. Therefore, considerable effort has been made in the past years to develop "green" oxidation technologies. Though homogeneous catalysts often have high activity, homogeneous processes suffer from the drawback of corrosion, and difficulty in catalyst recovery and reuse. Hence, the most attractive route concerning large scale industrial application is the heterogeneous catalytic oxidation with molecular oxygen. Application of solid catalysts for the gas-phase oxidation of structurally simple and volatile alcohols has been thoroughly investigated [51], but limitations are noticed when synthesizing complex, thermally unstable molecules.

The behavior of nanoparticles of copper and silver on an alumina support in the oxidation and dehydrogenation of ethanol was investigated. Pure alumina mainly acts as an acidic catalyst and produces diethyl ether and ethylene. Addition of copper and silver nanoparticles results in a direct conversion of ethanol into ethylene oxide. Addition of lithium oxide influenced the selectivity by suppressing the formation of diethyl ether and ethylene. Using $Ag/Li_2O/Al_2O_3$ and $Cu/Li_2O/Al_2O_3$ catalysts, it was possible to obtain high selectivity towards ethylene oxide at a temperature of 200 ^oC. Addition of cerium oxide results in higher selectivities towards CO [16]. Futhermore, the behavior of alumina-supported gold catalysts and the effects of addition of Li_2O and CeO_x on the oxidation, dehydrogenation and dehydration reactions of ethanol. Pure alumina mainly acts as an acidic catalyst and produces diethyl ether and ethylene. Gold particles play an important role in converting ethanol into ethylene oxide and acetaldehyde. Addition of lithium oxide influences the selectivity by suppressing the formation of diethyl ether and ethylene. With the $Au/Li_2O/Al_2O_3$ catalysts, a high selectivity toward ethylene oxide can be obtained. It is suggested that at low concentrations, the role of oxygen is mainly to prevent coke formation on the catalytic surface [17].

A range of silica-supported gold nanoparticle catalysts had been synthesized on various silica supports. The particle size was varied between 1.7 and 15 nm by varying the support and the gold loading procedure. A strong influenced of the gold particle size

on the non-oxidative dehydrogenation of ethanol is noted. The gold nanoparticles of about 6 nm showed a much higher activity than smaller or larger particles. In the presence of oxygen, the rate for dehydrogenation was much higher because of the presence of an adsorbed oxygen species, but the selectivity became lower as combustion starts to contribute. The intrinsic activity was constant up to about 7 nm and then increases for larger particles. The larger gold nanoparticles may contained strongly adsorbed oxygen atoms, which were much scarcer on smaller gold particles. The reaction rate was first order with respect to ethanol [52].

Three types of graphite nanofibers (GNFs), with varying orientations of the graphene sheets (herringbone, platelet, and ribbon), were used as catalysts for the gas-phase oxidative dehydrogenation of ethanol to acetaldehyde and ethyl acetate in the presence of oxygen. The effects of fiber type, temperature, oxygen concentration, and ethanol concentration on conversion and product ratio were explored. When identical processing conditions were employed, herringbone fibers produced higher conversions of ethanol compared to platelet and ribbon fibers. Altering equilibrium conditions by increasing oxygen concentration tended to increase conversion as well as increase the percentage of acetaldehyde produced. Adjusting oxygen concentration had a more significant effect on the platelet and ribbon fibers [15].

Oxidative dehydrogenation of ethanol to acetaldehyde has been performed on vanadium based catalysts prepared by grafting on titania–silica supports with different procedures. A comparison of the performances of the prepared catalysts in terms of activity and selectivity had been made. Grafting technique gives place to well dispersed catalysts that resulted more selective than catalysts prepared by impregnation. In particular, very selective catalysts had been obtained by grafting vanadium–titanium bimetallic alkoxides directly on silica support. The effect of both the preparation methods and the used supports on the catalytic performances had been studied and an attempt to correlate the observed properties with the obtained results had been made [14].

The influence of relative humidity of air on the catalytic activity of $Ag_3PW_{12}O_{40}$ and $Ag_3PMo_{12}O_{40}$ salts in the vapor phase dehydration of ethanol was investigated. The reaction was performed in air of relative humidity of 2% or 9% and in the temperature range of 373–493 K. The catalytic activity of $Ag_3PW_{12}O_{40}$ salt was much higher than the one obtained for $Ag_3PMo_{12}O_{40}$ salt and strongly dependent on relative humidity of air. However, the XPS spectroscopy exhibited the changes in surface composition of this salt after reaction in air of 2% of relative humidity whereas the SEM imaging displayed the formation of silver nanostructures on its surface. The $Ag_3PW_{12}O_{40}$ salt remained stable after reaction in air of 9% of relative humidity. In case of $Ag_3PMo_{12}O_{40}$ salt analyzed before and after ethanol dehydration, a very limited difference in surface composition was found by XPS that was supported by SEM imaging [53].

CHAPTER III

METHODOLOGY

3.1 Research Methodology

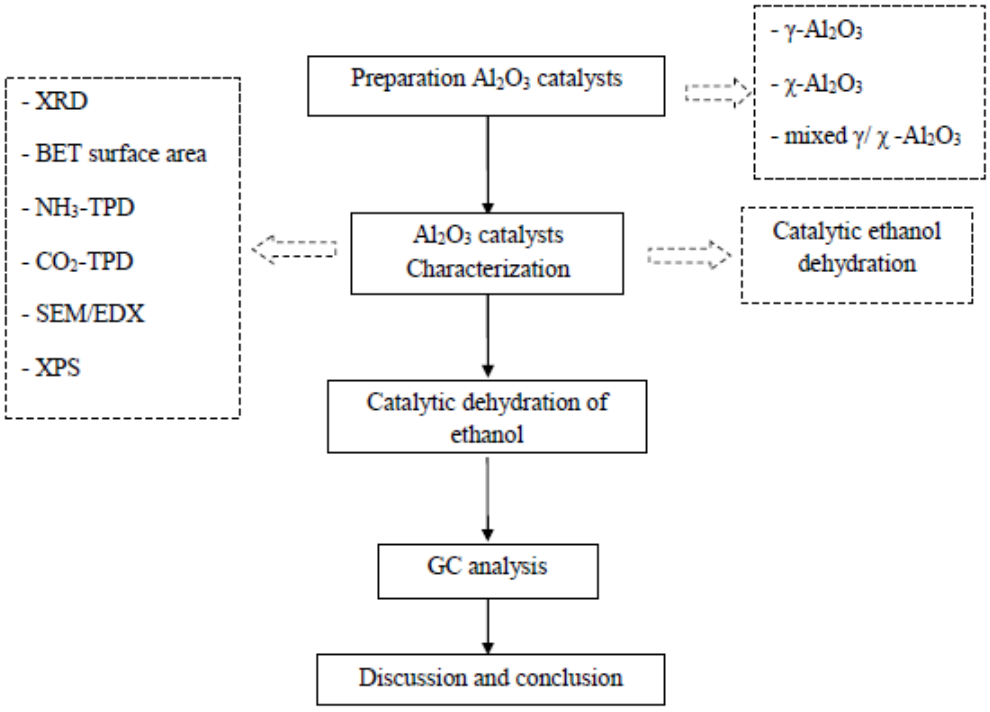

Figure 3.1 Flow diagram of research methodology for dehydration of ethanol via alumina catalysts

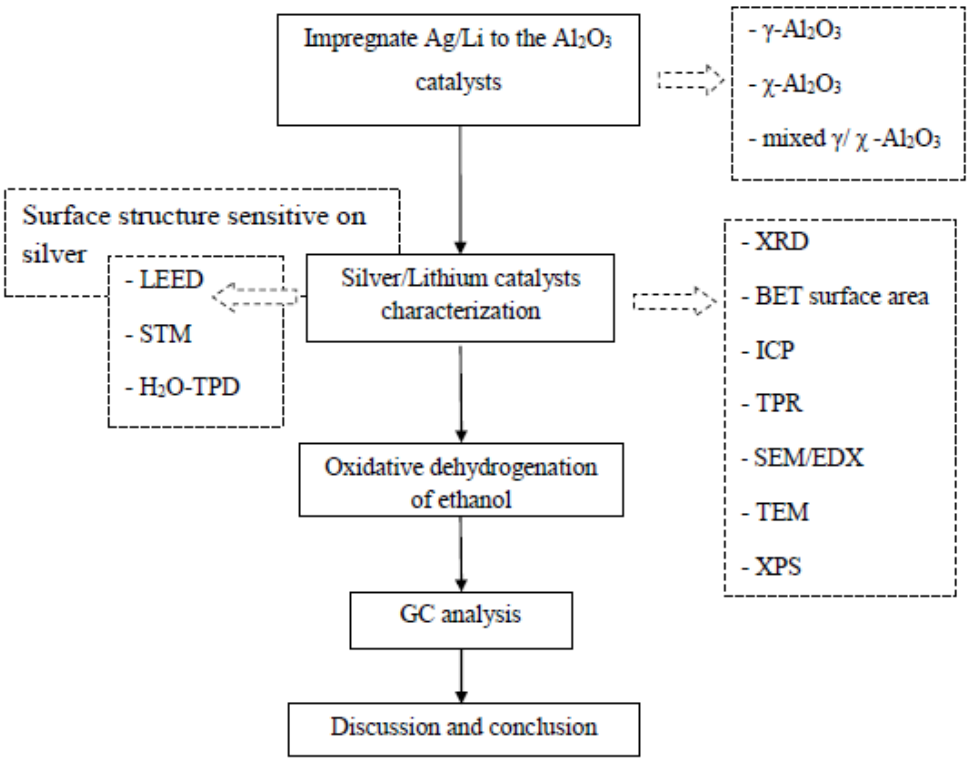

Figure 3.2 Flow diagram of research methodology for oxidative dehydrogenation of ethanol via sliver-lithium catalysts

3.2 Catalyst preparation

3.2.1 Chemicals

1. Aluminium isopropoxide 98 wt% (AIP) available from Aldrich.
2. Silver (II) nitrate 99 wt% ($AgNO_3$) available from Aldrich.
3. Lithium (II) nitrate 98 wt% ($LiNO_3$) available from Aldrich.
4. 1-Butanol (C_4H_9OH) from Fisher Scientific.
5. Toluene ($C_6H_5CH_3$) from Fisher Scientific.
6. Methanol (CH_3OH) from Merck.
7. Absolute ethanol available from BDH PRLABO
8. De-ionized water

3.2.2 Preparation of the various percent mixed γ/χ alumina particles via solvothermal method

Nanocrystalline aluminas having different chi and gamma phases (**Table 3.1**) were prepared by the solvothermal method according to the procedure described by Meephoka et al [22]. Twenty five grams of AIP was dissolved in 100 ml with different ratios of mixed solvent (butanol and toluene as shown in **Table 3.1**) in a test tube. After the autoclave was purged with nitrogen, the autoclave was heated up to the desired temperature (300 °C) at the rate of 2.5 °C min^{-1} and the temperature was held for 2 h. After the autoclave was cooled to room temperature, the precipitated powder was collected. The white powder was repeatedly washed with methanol and dried at room temperature. The synthesized alumina was subsequently calcined with a heating rate of 10 ^oC/min at the temperature raised to 600^oC and held on that temperature for 6 h using an air flow rate of 100 ml/min. The obtained alumina catalysts comprised of 0, 30, 50 and 100 wt% of χ-phase upon the mixed solvents employed as confirmed by the XRD measurement.

Table 3.1 Detail of different alumina catalysts and nomenclatures

Catalysts	Phase %		Dissolved solvent (ml)		The solvent outside the synthesis tube (ml)	
	χ-phases	γ-phases	Toluene	1-Butanol	Toluene	1-Butanol
CHI00	0	100	0	100	0	30
CHI30	30	70	30	70	9	21
CHI50	50	50	50	50	15	15
CHI100	100	0	100	0	30	0

3.2.3 Silver Lithium Loading

In this experiment, incipient wetness impregnation is the method used for loading metal active phase. Silver (I) nitrate [$Ag(NO_3)$] and Lithium nitrate [$Li(NO_3)$] are used as precursors in this method.

The incipient wetness impregnation procedure was as followed:

1. The certain amount of silver (Ag : supports weight ratio was 1 : 40) and lithium (Li : Al atomic ratio was 1 : 15) were introduced into the de-ionized water which its volume equals to pore volume of catalyst.

2. The desired support was impregnated with aqueous solution of silver and lithium. The silver and lithium solution was dropped slowly to the desired supports.

3. The catalyst was dried in the oven at 383 K for 12 h.

4. The catalyst was calcined in air at 673 K for 4 h.

3.2.4 Catalysts Nomenclature

The nomenclature used for the catalyst samples in this study is as follows:

CHIXX refers to mixed phase alumina composed of (100-XX)% γ-phase and XX% χ-phase

AgLi-CHIXX refers to silver and lithium supported on mixed phase alumina composed of (100-XX)% γ-phase and XX% χ-phase

3.3 Catalyst characterization

3.3.1 X- ray diffraction (XRD)

XRD was performed to determine the bulk phase of catalysts by SIEMENS D 5000 X-ray diffractometer connected with a computer with Diffract ZT version 3.3 programs for full control of the XRD analyzer. The experiment was carried out by using CuK_α radiation with Ni filter in the 2θ range of 20-80 degrees with resolution 0.04°. The crystallite size was estimated from line broadening according to the Scherrer equation and α-Al_2O_3 was used as standard.

3.3.2 N_2 physisorption

BET apparatus for the single point method, the reaction apparatus of BET surface area measurement consisted of two feed lines for helium and nitrogen. The flow rate of the gas was adjusted by means of fine-metering valve on the gas chromatograph. The sample cell was made from pyrex glass. The mixture gases of helium and nitrogen were flown through the system at the nitrogen relative of 0.3. The catalyst sample (ca. 0.1 g) was placed in the sample cell, which was then heated up to 160 °C and hold at this temperature for 2 h. After the catalyst sample was cooled down to room temperature, nitrogen uptakes were measured as follows.

1. Adsorption step: The sample that is set in the sample cell were dipped into liquid nitrogen. Nitrogen gas that was flowed through the system were adsorbed on the surface of the sample until equilibrium was reached.

2. Desorption step: The sample cell with nitrogen gas-adsorption catalyst sample was dipped into the water at room temperature. The adsorbed nitrogen gas was desorbed from the surface of the sample. This step was completed when the indicator line was in the position of base line.

3. Calibration step: 1 ml of nitrogen gas at atmospheric pressure was injected through the calibration port of the gas chromatograph and the area was measured.

3.3.3 Scanning Electron Microscopy: SEM and Energy Dispersive X-ray Spectroscopy (EDX)

Scanning electron microscopy (SEM) and energy dispersive X-ray spectroscopy (EDX) were used to determine the morphology and elemental distribution of the catalyst particles. Model of SEM: JEOL mode JSM-5800LV and EDX was performed using Link Isis Series 300 program.

3.3.4 Transmission Electron Microscope (TEM)

The particle size and distribution of catalyst samples were observed using JEOL-JEM 200CX transmission electron microscope operated at 100 kv.

3.3.5 X-ray photoelectron spectroscopy (XPS)

For each and every element, there is a characteristic binding energy associated with each core atomic orbital i.e. each element gives rise to a characteristic set of peaks in the photoelectron spectrum at kinetic energies is determined by the photon energy and the respective binding energies. The presence of peaks at particular energies therefore indicates the presence of a specific element in the sample under study. Furthermore, the intensity of the peaks is related to the concentration of the element within the sampled region. Thus, the technique provides a quantitative analysis of the surface composition and is sometimes known by the alternative acronym, ESCA (Electron Spectroscopy for Chemical Analysis). The most commonly employed X-ray sources are those giving rise to:

Mg K_a radiation : h_n = 1253.6 eV Al K_a radiation : h_n = 1486.6 eV

The emitted photoelectrons therefore have kinetic energies in the range of ca. 0 1250 eV or 0 - 1480 eV. Since such electrons have very short IMFPs in solids, the technique is necessarily surface sensitive.

3.3.6 Temperature programmed reduction (TPR)

TPR was used to determine the reducibility of catalysts. The catalyst sample 0.1 g use in the operation and temperature ramping from 30 ^oC to 500 ^oC at 10 ^oC/min. The carrier gas was 10 % H_2 in Ar. During reduction, a cold trap was placed to before the detector to remove water produced. A thermal conductivity detector (TCD) measure the amount of hydrogen consumption. The calibration of hydrogen consumption was performed with bulk cobalt oxide (Co_3O_4) at the same conditions.

3.3.7 Ammonia Temperature-Programmed Desorption (NH_3-TPD)

The acidity of the catalyst samples was determined by temperature programmed desorption of ammonia using a Micromeritics Chemisorp 2750. In the experiment, about 0.10 g of the catalyst sample was placed in a glass tube and pretreated at 500^oC in a flow of helium. The sample was saturated with 15% NH_3/He. After saturation, the physisorbed ammonia was desorped in a helium gas flow about 2 h. Then the sample was heated from 30 to 500 ^oC at a heating rate 10 ^oC/min. The amount of ammonia in effluent was measured via TCD signal as a function of time.

3.3.8 Carbon dioxide Temperature-Programmed Desorption (CO_2-TPD)

The basicity of the catalyst samples was determined by temperature programmed desorption of carbon dioxide using a Micromeritics Chemisorp 2750 with a computer. In an experiment, about 0.10 g of the catalyst sample was placed in a glass tube and pretreated at 500 ^oC in a flow of helium. The sample was saturated with pure CO_2. After saturation, the physisorbed carbon dioxide was desorbed in a helium gas flow for about 2 h. Then the sample was heated from 30 to 500 ^oC at a heating rate 10 ^oC/min. The amount of carbon dioxide in effluent was measured via TCD signal as a function of time.

3.3.9 UV-Visible absorption spectroscopy (UV-Vis)

The oxidation state of silver was determined by spectroscopic method using UV-Visible absorption spectroscopy (Perkin Elmer Lamda 650, wavelength 200-600 nm and step size 1 nm).

3.3.10 Inductively Coupled Plasma-Optical Emission Spectroscopy (ICP-OES)

The percentage of catalyst component such as silver, lithium and alumina was analyzed by ICP-OES (Perkin Elmer model PLASMA-1000).

3.4 Reaction study of ethanol

3.4.1 Materials

Catalytic ethanol reaction was performed using 0.05 g of catalyst that was packed in the middle of the glass micro-rector, which was located in the electrical furnace. Ethanol was introduced to the reactor by bubbling He as a carrier gas through the saturator which was kept at 45^{o}C to maintain the partial pressure and hence the composition of the feed. A flow rate of Ar was kept at 50 ml/min. Ethanol reaction was ranged between 200 to 400^{o}C and 1 atm total pressure. The effluent was analyzed using gas chromatography technique [Thermal conductivity detector (TCD), Porapak-Q was used for separation of carbon dioxide (CO_2) and ethylene (C_2H_4) and Molecular sieve 5 $\mathring{A}$ was used for separation of carbon monoxide (CO) and oxygen (O_2) Furthermore, flame ionization detector (FID), DB-5 was used for separation of light hydrocarbon such as ethanol (C_2H_5OH), ethylene (C_2H_4), acetaldehyde (C_2H_4O), diethyl ether ($C_2H_5OC_2H_5$), etc.]

3.4.2 Apparatus

Flow diagram of catalytic ethanol reaction system is shown in **Figure 3.3** and **Figure 3.4** for dehydration and oxidative dehydrogenation, respectively. The system consists of a reactor, an automatic temperature controller, an electrical furnace and a gas controlling system.

3.4.2.1 Reactor

The reactor was made from a glass tube (O.D. 3/8"). Two sampling points was provided above and below the catalyst bed. Catalyst was placed between two quartz wool layers

3.4.2.2 Automatic Temperature Controller

This unit consisted of a magnetic switch connected to a variable voltage transformer and a solid-state relay temperature controller model no. SS2425DZ connected to a thermocouple. Reactor temperature was measured at the bottom of the catalyst bed in the reactor. The temperature control set point was adjustable within the range of 0-400 ^{o}C at the maximum voltage output of 220 volt.

3.4.2.3 Electrical Furnace

The furnace supplied heat to the reactor for catalytic ethanol reaction. The reactor could be operated from temperature up to 400 ^{o}C at the maximum voltage of 220 volt.

3.4.2.4 Gas Controlling System

Reactant for the system was equipped with a pressure regulator and an on-off valve and the gas flow rates were adjusted by using metering valves.

3.4.2.5 Gas Chromatography

The composition of hydrocarbons in the product stream was analyzed by a Shimadzu GC14B (DB5) gas chromatograph equipped with a flame ionization detector. A Shimadzu GC8A (molecular sieve 5A and Parapak Q) gas chromatography equipped with a thermal conductivity detector was used to analyze CO, CO_2 and O_2 in the feed and product streams. The operating conditions for each instrument are shown in the **Table 3.2**.

Table 3.2 Operating condition for gas chromatograph

Gas Chromatograph	SHIMADZU GC-8A		SHIMADZU GC-14B
Detector	TCD	TCD	FID
Column	Molecular sieve 5A	Parapak Q	DB5
Maximum temperature	350°C	150°C	350°C
Carrier gas	He (99.999%)	He (99.999%)	N_2 (99.999%)
Carrier gas flow	40 cc/min		-
Column temperature			
- initial (°C)	80	80	40
- final (°C)	80	80	40
Injector temperature (°C)	100	100	150
Detector temperature(°C)	-	-	150
Current (mA)	80	80	-
Analysed gas	CO, O_2, N_2	CO_2, C_2H_4, CH_4	Ethanol, ethylene, acetaldehyde, diethyl ether

3.4.3 Procedures

3.4.3.1 Dehydration

1. The 0.05 g of catalyst was packed in the middle of the glass microrector, which was located in the electrical furnace.

2. A flow rate of Ar at 50 ml/min, was employed in a fixed-bed flow reactor. Ethanol was introduced to the reactor by bubbling Ar as a carrier gas through the saturator which is kept at 45^{o}C to maintain the partial pressure and hence the composition of the feed.

3. The catalyst sample was pre-treated *in situ* in flowing Ar at 200 ^{o}C for 1 h prior to dehydration of ethanol.

4. Dehydration of ethanol was performed at the temperatures range between 200 to 400^{o}C and 1 atm total pressure.

5. The effluent was analyzed using gas chromatography technique. [Flame ionization detector (FID) was used for separation of light hydrocarbon such as ethanol (C_2H_5OH), acetal dehyde (C_2H_4O), diethyl ether ($C_2H_5OC_2H_5$), etc.].

3.4.3.2 Oxidative dehydrogenation

1. The 0.05 g of catalyst was packed in the middle of the glass microrector, which is located in the electrical furnace.

2. A flow rate of Ar at 50 ml/min, 10% O_2 in He at 25 ml/min and H_2 at 50 ml/min in a fixed-bed flow reactor. Ethanol was introduced to the reactor by bubbling Ar as a carrier gas through the saturator which was kept at 45^{o}C to maintain the partial pressure and hence the composition of the feed.

3. The catalyst sample was pre-reduced *in situ* in flowing H_2 at 300^{o}C for 1 h prior to oxidative dehydrogenation of ethanol.

4. Oxidative dehydrogenation of ethanol was performed at the temperatures range between 200 to 400^{o}C and 1 atm total pressure.

5. The effluent was analyzed using gas chromatography technique. [Thermal conductivity detector (TDC) is used for separation of carbon monoxide (CO), carbon dioxide (CO_2) and oxygen (O_2). Furthermore, flame ionization detector (FID) is used for separation of light hydrocarbon such as ethanol (C_2H_5OH), acetal dehyde (C_2H_4O), diethyl ether ($C_2H_5OC_2H_5$), etc.].

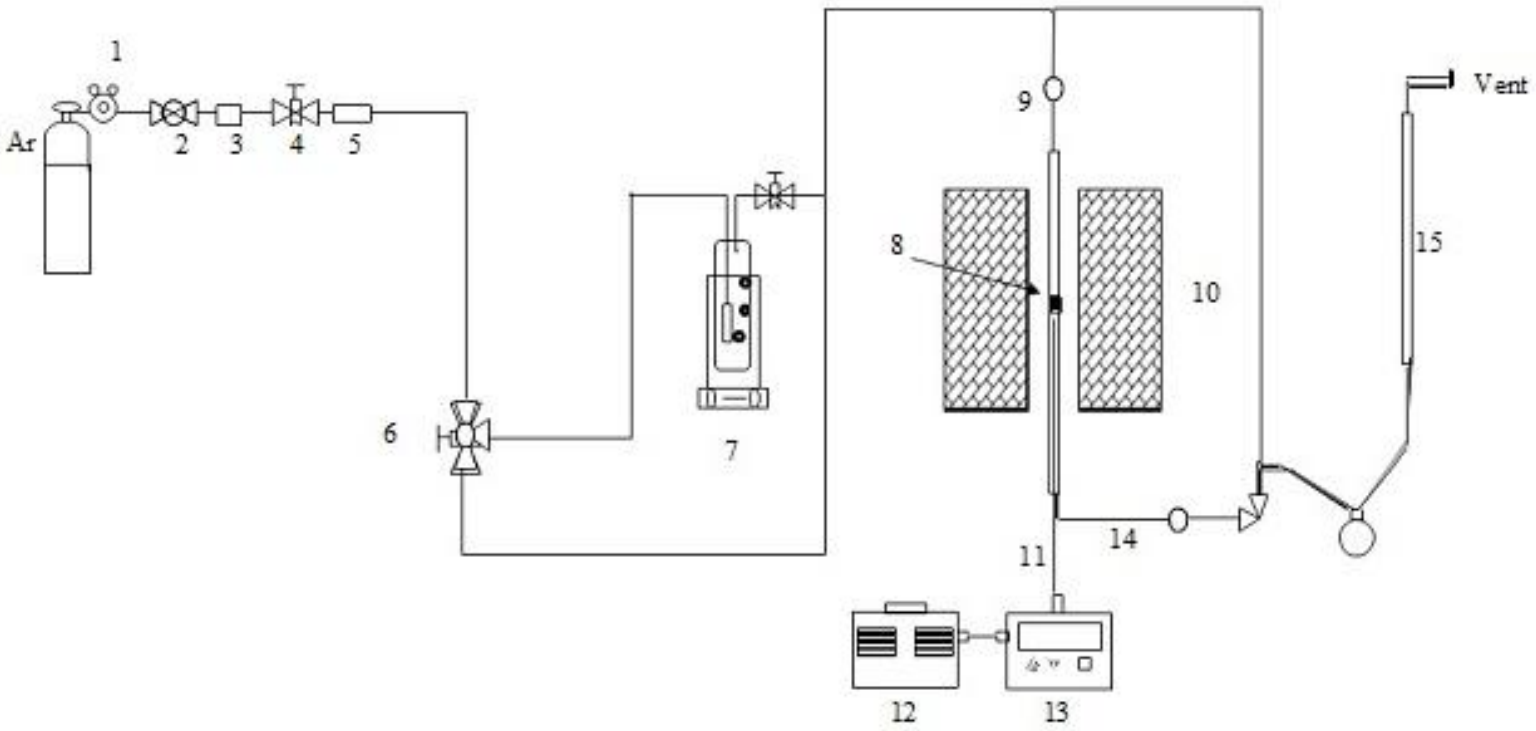

1. Pressure Regulator 2. On-Off Value 3. Gas Filter 4. Metering Valve 5. Back Pressure

6. 3-way Valve 7. Saturator 8. Catalyst Bed 9. Sampling point 10. Furnace

11. Thermocouple 12. Variable Voltage Transformer 13. Temperature Controller 14. Heating Line 15. Bubble Flow

Figure 3.3 Flow diagram of ethanol dehydration system.

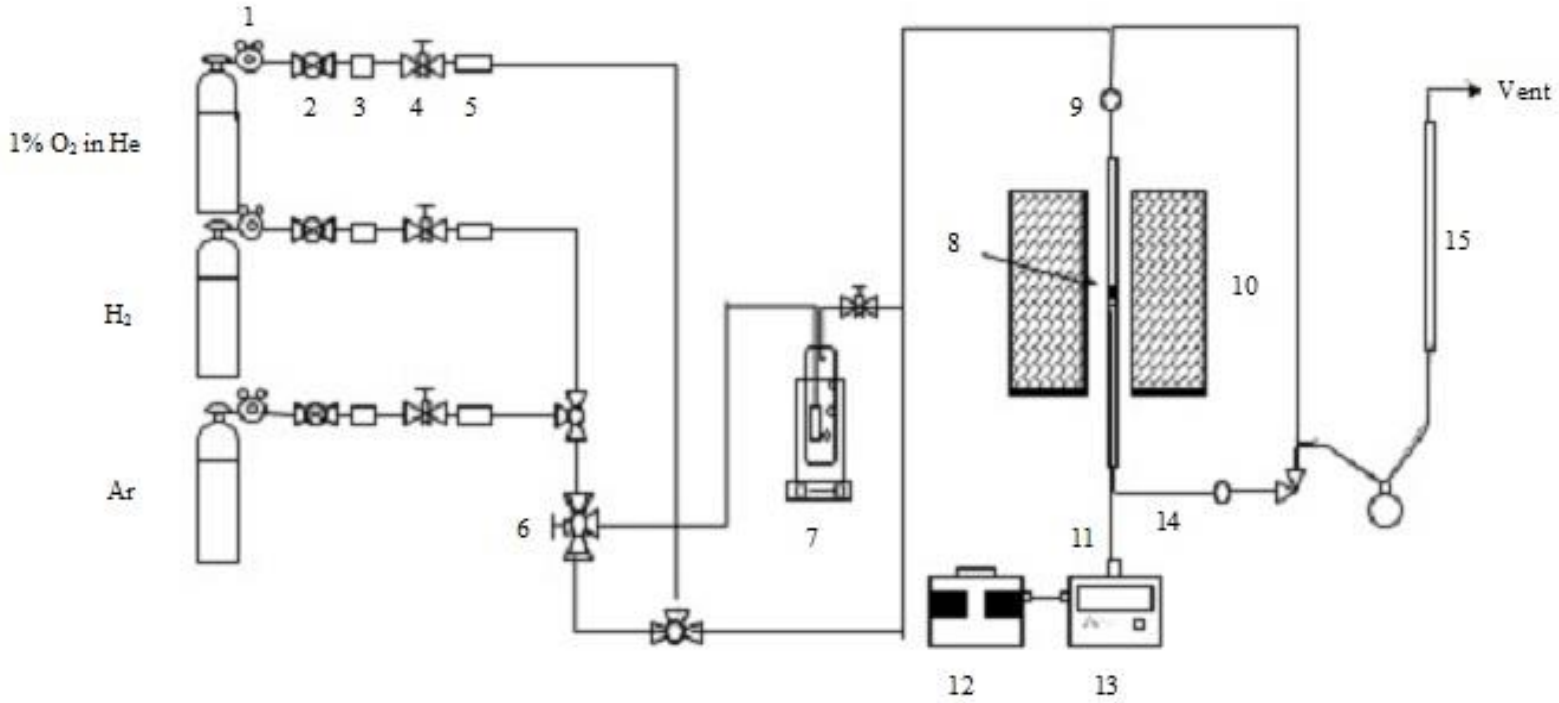

1. Pressure Regulator 2. On-Off Value 3. Gas Filter 4. Metering Valve 5. Back Pressure

6. 3-way Valve 7. Saturator 8. Catalyst Bed 9. Sampling point 10. Furnace
11. Thermocouple 12. Variable Voltage Transformer 13. Temperature Controller 14. Heating Line 15. Bubble Flow

Figure 3.4 Flow diagram of oxidative dehydrogenation system

3.5 Surface structure sensitive on partially curved silver single crystal

3.5.1 Surface morphology

To allow for easy variation of step type and step density, an Ag single crystal with a well-polished curved surface was used. The curvature is in principle due to atomic steps separating terraces (**Figure 3.5a**). Note that faceting and step bunching have been observed for Pt [54], Au [55] and Ni [56] curved samples. With the [111] vector in the middle of a curvature following [001] toward [110] via [111], an FCC metal has two different step types to either side. This is depicted in **Figure 3.5b**. Whereas the A step type consists of a square arrangement, the B step type consists of a rectangular arrangement of atoms. A Laue back reflection study indicates that our crystal's normal is not exactly the [111] direction. It is tilted by ~0.6º in the [110] direction and ~0.3º in the [011] direction. These deviations cause the 'infinite' (111) plane to be slightly off the center of the crystal's curvature. In addition, the crystal is azimuthally rotated by ~1º. This causes the steps to a non-straight average step direction and thus a small difference in the number of R vs S-type kinks.

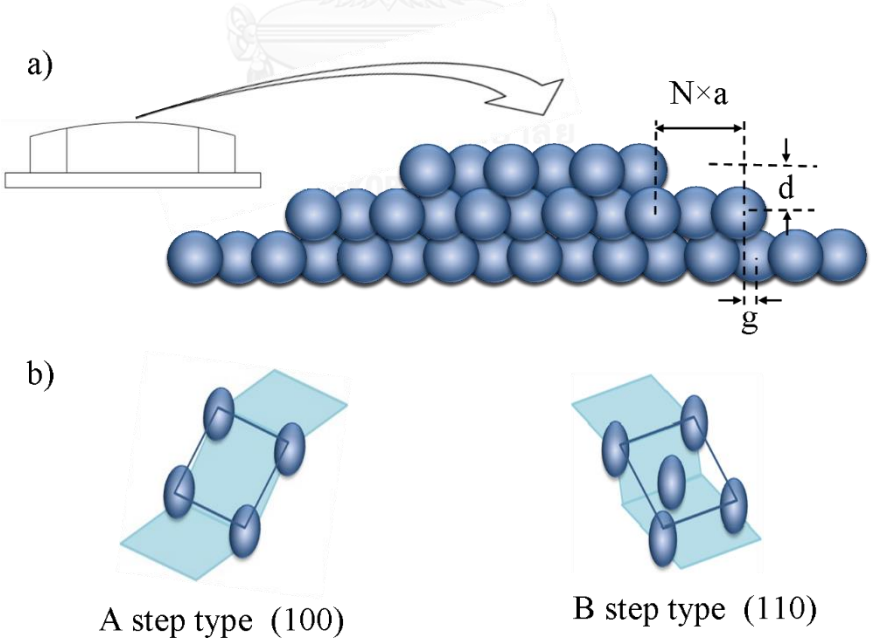

Figure 3.5 (a) Schematic drawing of a curved FCC metal single crystal with [111] centered at the curvature (b) Schematic drawing of the atomic arrangements of the A and B step types.

Figure 3.6 showed three schematic drawings and a photograph of the actual Ag crystal used in our studies. The surface is curved and polished only on its top side. It may be considered a 31º section of a 30 mm diameter cylinder. With this angle, the surface structures range from approximately [5(111)x100] on the outer left side (front view) via (111) near the middle to [5(111)x(110)] on the outer right side. The initial crystal was spark eroded from an Ag boule. It was circular, 10 mm in diameter and ~3 mm thick. At the edge, a 1 mm wide ring was removed to leave a 0.6 mm thick flange and 8 mm diameter top surface. The sides were removed making it 7 mm wide. The curvature on the top of the crystal was initially created by spark erosion and sanding. The crystal was subsequently polished in an automated, custom built polishing machine (Surface Preparation Labs, Zaandam, the Netherlands).

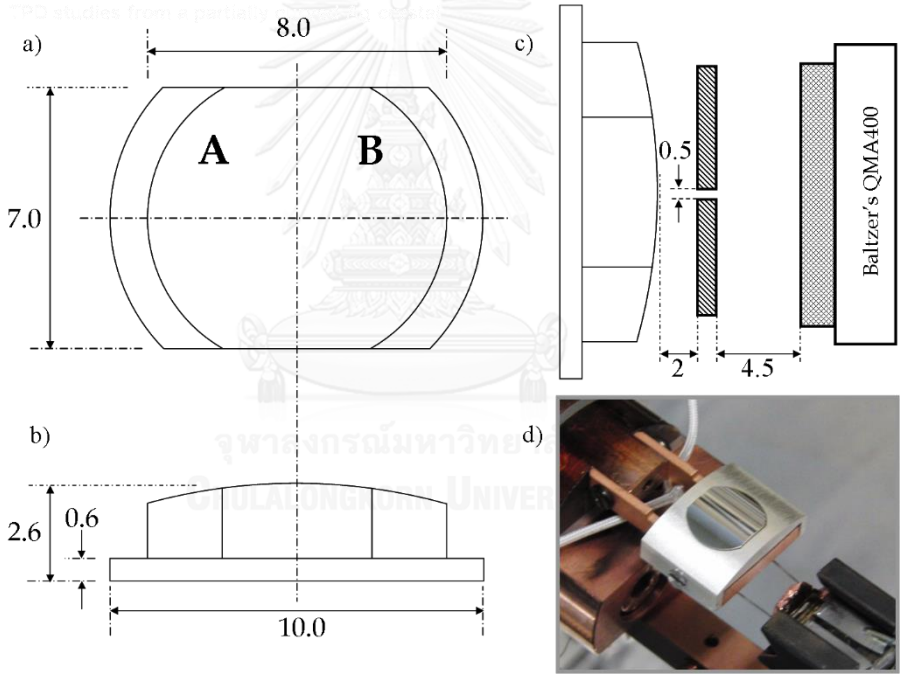

Figure 3.6 Schematic drawings (dimensions in mm) of the curved Ag crystal (a) front view with step type indication (b) bottom view (c) top view of crystal in front of the differentially pumped QMS (d) Photograph of the crystal with retaining Ag cap.

At its 1 mm wide flange, the crystal was held by a polycrystalline Ag cap onto a Cu base plate by two screws (**Figure 3.6d**). This assembly was connected with two solid Cu leads extending from the base plate to a bath cryostat. It is electrically isolated using AlN blocks (not visible in the picture. The cryostat is inserted into the UHV chamber through an x,y,z, ϑ manipulator). Behind the base plate, a filament from a

commercial light bulb (Osram) enables uniform heating of the base plate and crystal. The filament is spring loaded at its glass base. Heating is performed either radiatively or by electron bombardment using a positive voltage on the crystal assembly while the filament is grounded. A type-K thermocouple is inserted into the side of the Ag polycrystalline cap. For temperature control, we use a PID controller with an internal ice point reference (Eurotherm 2416).

3.5.2 Characterization of partially curved silver single crystal using Low Energy Electron diffraction (LEED) and Scanning tunnelling microscopy (STM)

The crystal assembly was initially held in a home-built ultrahigh vacuum (UHV) surface science chamber for cleaning and surface structure determination using low energy electron diffraction (LEED). This system has a base pressure of $3x10^{-10}$ mbar and contains, amongst others, a sputter gun (Prevac, IS 40C1), a QMS (Baltzers Prisma 200), and LEED optics (LK Technologies RVL2000/8/R). The crystal was cleaned by sputtering-annealing cycles. We sputter using Ar^+ (6.0 Messer) at 600 V and 2 μA while rotating the crystal 2º per minute, and anneal at 675 K for 10 min. LEED studies were performed with the electron beam impinging along [111] at all locations along the curved surface. The surface was translated normal to the impinging electron beam.

Finally, the crystal's surface was also studied using scanning tunnelling microscopy (STM). Here, we employ a commercial UHV system (Omicron) containing separate preparation and analysis chambers. The latter has a base pressure of $2x10^{-10}$ mbar and contains a variable temperature scanning tunnelling microscope (VT-STM). We redesigned the sample holder such that the entire polished surface could be imaged, while the holder still fit inside the analysis chamber's sample carousel. Parts of the sample holder in proximity to the sample's polished surface were covered by an Ag foil to prevent cross-contamination of the sample during sputtering. Tungsten STM tips were prepared by electrochemical etching in NaOH using DC current. Under UHV conditions, tip treatment also included heating the tip apex with a 100-500 uA electron emission current to remove tungsten oxide and tip stabilisation by applying 2-3 V pulses wile scanning. We used AES (VG 100AX hemispherical analyzer in combination with

a LEG-63 electron gun) and LEED (VG RVL900) regularly to verify cleanliness and long-range surface order. AES spectra never showed any sign of adsorbed oxygen, O_{ads}, on any of the stepped (111) surfaces, even after prolonged exposure (~10^3 mbar*s) to O_2 at room temperature.

3.5.3 Thermal desorption of water

Subsequently, the crystal assembly was moved to a second home-built UHV chamber with a base pressure of $9x10^{-11}$ mbar for spatially-resolved temperature programmed desorption (TPD) studies. Here, a Baltzers QMA400 head was kept in a differentially pumped canister that connects to the main UHV chamber via a 0.5x5 mm^2 rectangular slot (**Figure 3.6b**). The curved crystal is positioned ~2 mm from this orifice for TPD studies. It is translated laterally to monitor desorption from different surface structures in separate experiments. H_2O (Millipore, 18.2 MΩ) was dosed onto the Ag sample at 86 K using a home-built 10 mm diameter capillary array doser at a distance large enough to ensure a uniform flux across the entire cleaned surface. The water was degassed by multiple freeze-pump-thaw cycles and backfilled with 1.1 bar He (AirProducts 6N) prior to experiments. The H_2O/He mixture was generally dosed onto the crystal for different durations at a fixed pressure of $1x10^{-7}$ mbar in the UHV chamber as determined by an uncalibrated cold cathode gauge. Co-dosing with He allows us to dose H_2O reproducibly as the co-dosed He yields a large and accurately determined pressure change. Subsequent TPD experiments were performed at 1.0 K/s while monitoring m/z = 18. We have verified by TPD that the cold sample did not accumulate CO (m/z=28) to measurable amounts prior to or during the experiment. LEED (LK Technologies RVL2000/8/R) was regularly used to verify the structure of the bare Ag surface, while Auger Electron Spectroscopy (AES) was used to verify cleanliness (Staib Instruments, ESA 100).

CHAPTER IV
RESULTS AND DISCUSSIONS

This chapter was aimed to investigate the effects of mixed phase alumina for catalytic dehydration and oxidative dehydrogenation of ethanol. The topic was divided into two sections. The first section contained the preparation and characterization of the native γ-phase, χ-phase and the mixed phase alumina catalysts for catalytic dehydration of ethanol. The second section showed characteristic and catalytic activity of silver-lithium supported on alumina catalyst. In addition, in order to investigate surface-structure sensitive on silver catalyst, the adsorption of H_2O onto the A and B type steps on an Ag single crystal by temperature programmed desorption was studied.

4.1 Dehydration of ethanol over the mixed phase alumina catalysts

This section described the ethanol dehydration over the mixed-phase alumina catalysts. In addition, the preparation and characterization of the native and mixed of nanocrystalline γ- and χ-phases alumina by solvothermal method was investigated.

4.1.1 Characteristics

The physical properties of the catalysts prepared by the solvothermal synthesis were obtained from the N_2 physisorption and XRD data. The compositions of γ- and χ-phases of nanocrystalline alumina were produced depending on the different types and amounts of solvents, such as 1-butanol and toluene employed during the synthesis. In fact, the mixed γ- and χ-phases of nanocrystalline alumina were controllably obtained by mixing solvents between 1-butanol and toluene with desirable composition as shown in **Table 4.1**. The phase identification of all catalysts was carried out on the basis of data obtained from XRD measurment as shown in **Figure 4.1**. The CHI00 catalyst, which was produced using only 1-butanol as the synthesis solvent exhibits the diffraction peak at 32 37, 39, 45, 61 and 66^o. This evidently proved that CHI00 catalyst is the native γ- phase nanocrystalline alumina. However, with the use of mixed solvent of toluene and 1-butanol, the characteristic diffraction peak of χ-phase nanocrystalline alumina was remarkably appeared at 43^o. Certainly, the higher intensity of peak area at

43^{o} can be attributed to the increase of χ-phase present in the catalysts. In addition, the γ- and χ-phase compositions of alumina catalysts were determined by the area of characteristic peak at 43^{o} from the calibration curve obtaining from the XRD patterns of the physical mixture between native γ- and χ-phase with different contents according to those reported by Meephoka et al. [22]. This result was also in corresponding with that from the previous work [20]. The obtained catalysts consisting of 0%, 30%, 50% and 100% χ-phase are denoted as CHI00, CHI30, CHI50 and CHI100, respectively.

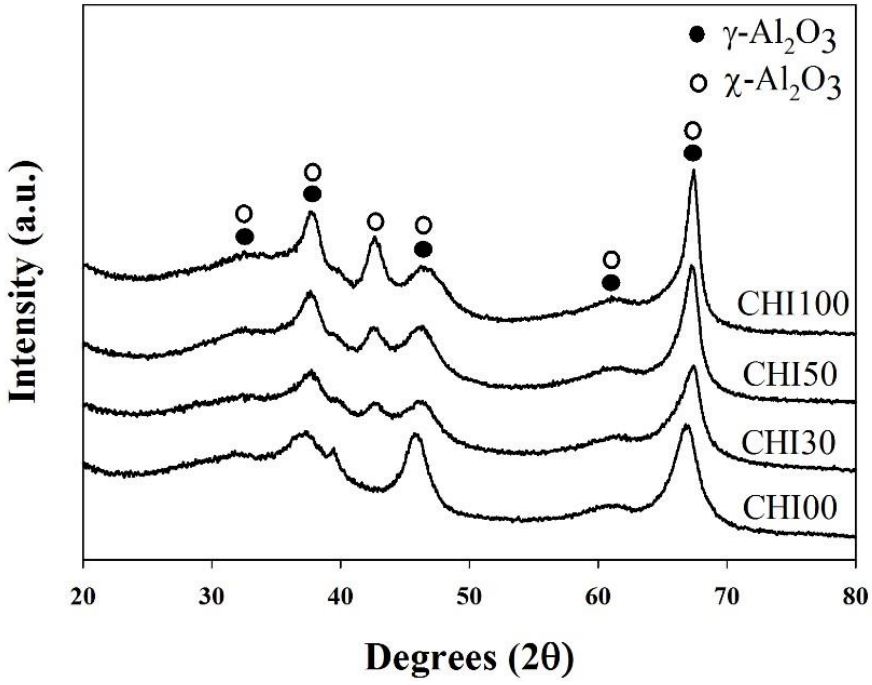

Figure 4.1 XRD patterns of all prepared catalysts.

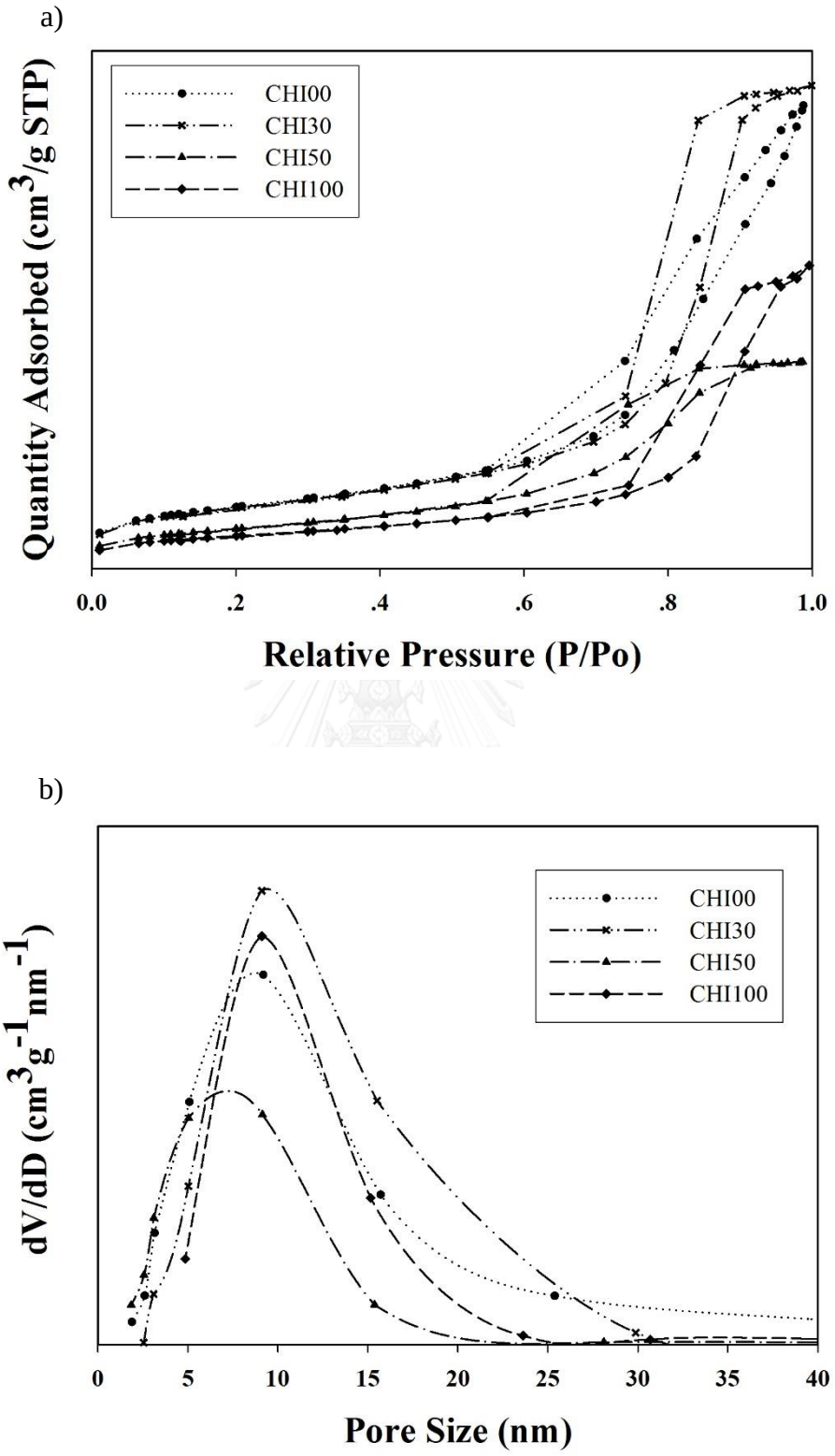

Figure 4.2 N_2 physisorption profiles of all prepared catalysts (a) adsorption-desorption isotherm and (b) pore size distribution profiles.

The effect of phase composition on the pore size and pore size distribution of catalysts measured by the nitrogen adsorption-desorption is shown in **Figure 4.2a** and **2b**. The isotherms of all catalysts are in the classical shape of the typical Type IV isotherms that refer to mesoporous materials as described by the IUPAC. As seen in **Figure 4.2a**, the isotherms of the CHI30, CHI50, and CHI100 catalysts reveal the H1 hysteresis loops occurred at a relative pressure range (P/P_0) of 0.55 – 0.95. The H1 hysteresis loop is often associated with porous materials indicating a broad pore size distribution with a uniform cylindrical-like pore. In the contrary, the isotherm of CHI00 catalyst was quite different indicating that the H3 hysteresis loop does not exhibit any limiting adsorption at high relative pressure. This behavior can be for instance caused by the existence of non-rigid aggregation of wrinkled sheet-like particles or agglomeration of slit-shaped pores. Moreover, this principle should not be expected to provide a reliable assemble assessment of either the pore size distribution or the total pore volume. The pore size distribution present here confirms isotherm assertion and mesoporous structure for all prepared catalysts as seen in **Figure 4.2b**. The structural parameters of all alumina catalysts derived from these isotherms are summarized in **Table 4.1**. The BET surface area of the catalysts decreased from 257 to136 m^2/g with the larger quantity of χ-phase being present from 0 to 100%, whereas the average pore diameter was rather similar for the different catalysts. The results were in accordance with the previous work [22, 31].

Table 4.1 BET surface area, pore volume and pore diameter of all prepared catalysts.

Catalysts	A_{BET} (m^2/g)	V_p (cm^3/g)	D_{BJH} (nm)
CHI00	257	0.84	8.27
CHI30	254	0.87	8.19
CHI50	168	0.37	5.46
CHI100	137	0.55	10.42

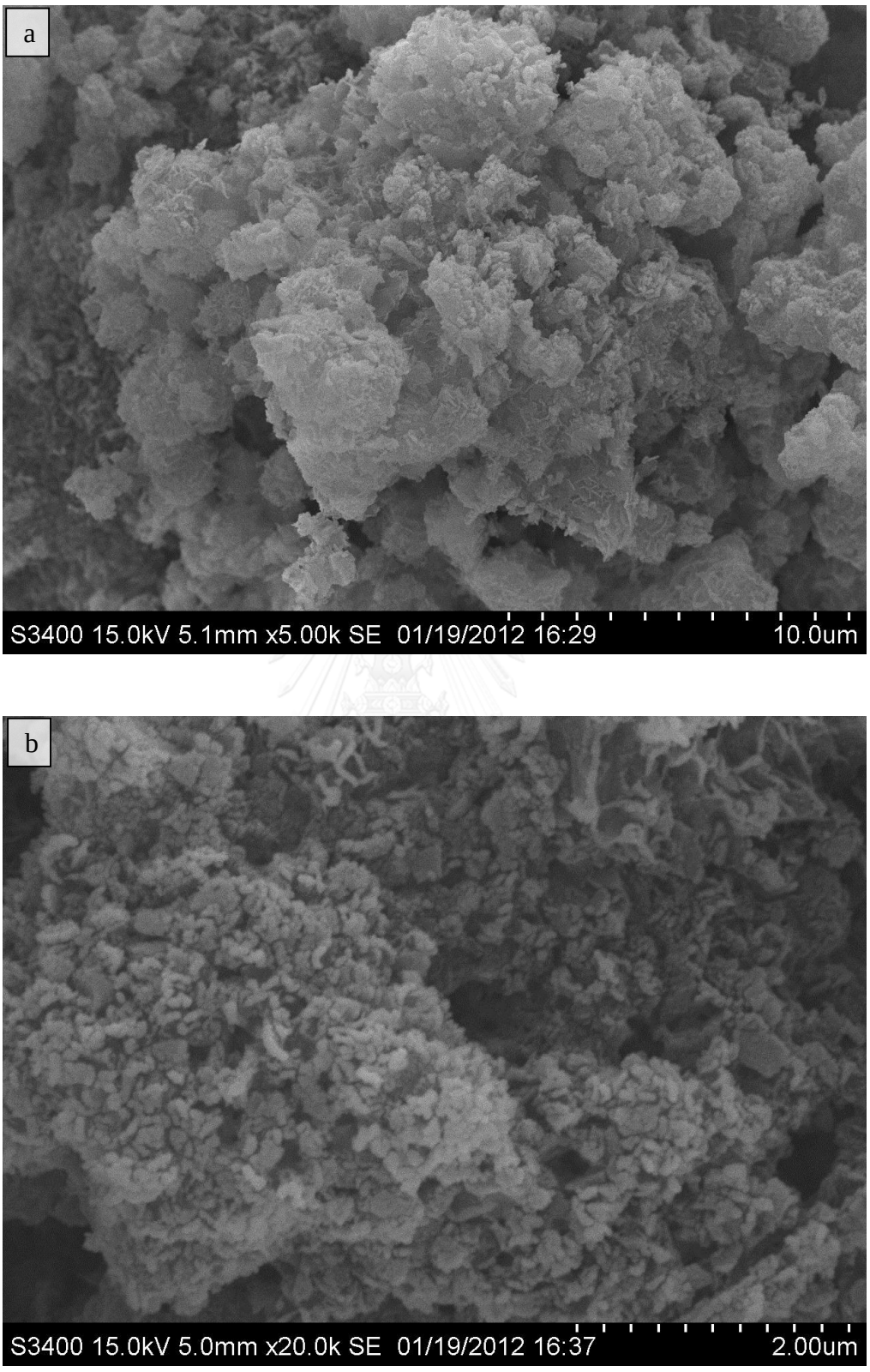

Figure 4.3 SEM micrographs of prepared pure γ- phase and χ-phase alumina catalysts (a) CHI00, (b) CHI00, (c) CHI100 and (d) CHI100.

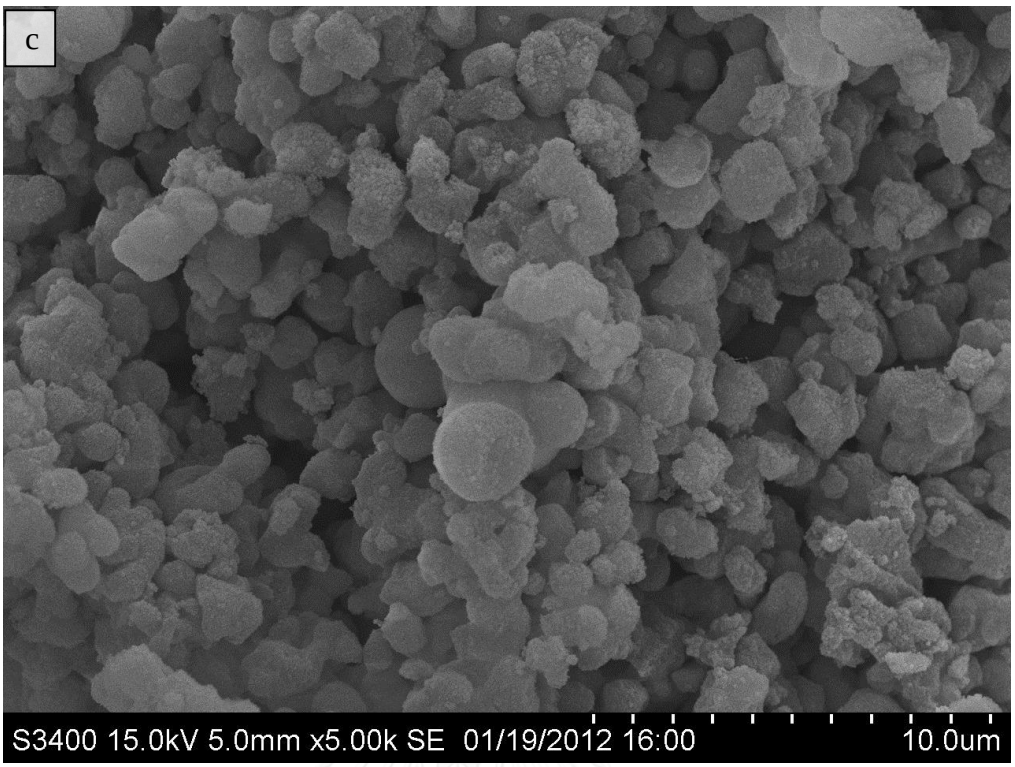

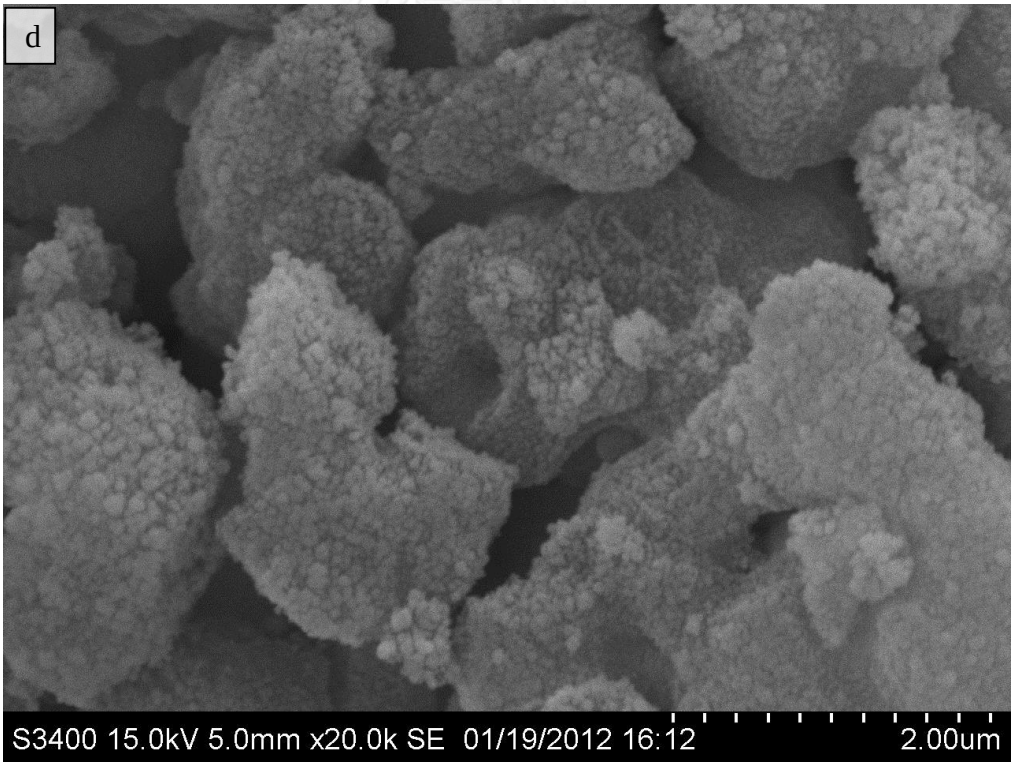

Figure 4.3 (cont.) SEM micrographs of prepared pure γ- phase and χ-phase alumina catalysts (a) CHI00, (b) CHI00, (c) CHI100 and (d) CHI100.

The SEM images of prepared catalysts containing the native γ- phase (CHI00) and χ-phase (CHI100) are shown in **Figure 4.3a-b** and **Figure 4.3c-d**, respectively. It can be observed that the catalyst particles are the secondary agglomerated catalyst particles of the prepared native γ- phase and native χ-phase alumina resulting in the presence of large micron sized granules. However, it can be observed the secondary catalyst particle having size between 0.1-0.2 micron as seen in **Figure 4.3b** and **Figure 4.3d**. The observed mesoporosity can be attributed to the voids from inter-connected between primary particles. It can be seen that the morphology of both catalysts are quite different. This is likely that the wrinkled sheet morphology is attributed to the presence of native γ- phase, while χ-phase is present as the spherical shape [33].

It is well known that the acidic property of the alumina catalysts importantly influences on their catalytic properties. The acidic property was investigated using the temperature programmed desorption of NH_3 (NH_3-TPD). The desorbed profiles and integral area of desorbed NH_3 from all catalysts can be evaluated relating to the acidic strength and the number of total acid sites on catalysts. The bimodal desorption peaks obviously reveal that the catalyst samples occupy a heterogeneous distribution of two different strength types of acid sites. NH_3-TPD profiles probably distinguish two peaks of desorption, which are according to the temperature range between 40 to 250 and 250 to 500 ^{o}C as seen in **Figure 4.4a-4.4d**. This can be generally assigned to the overlap of two desorption steps of weak acid sites and moderate to strong acid sites. The weak acid sites are probably defined as Lewis acid site on aluminum oxide at lower temperature [57]. It was found that the fraction of weak acid sites for all catalysts was ranged between 22.5 to 36.4%. On the contrary, the moderate to strong mode of interaction is perhaps defined as the Brønsted acid sites at higher temperature [57]. It was reported that a peak was observed at ca. 320 ^{o}C on P/HZM-5(Ga), which is attributed to the desorbed NH_3 from strong Brønsted acid sites [58]. However, the identity of acid type, which was evaluated by NH_3-TPD, was unclear.

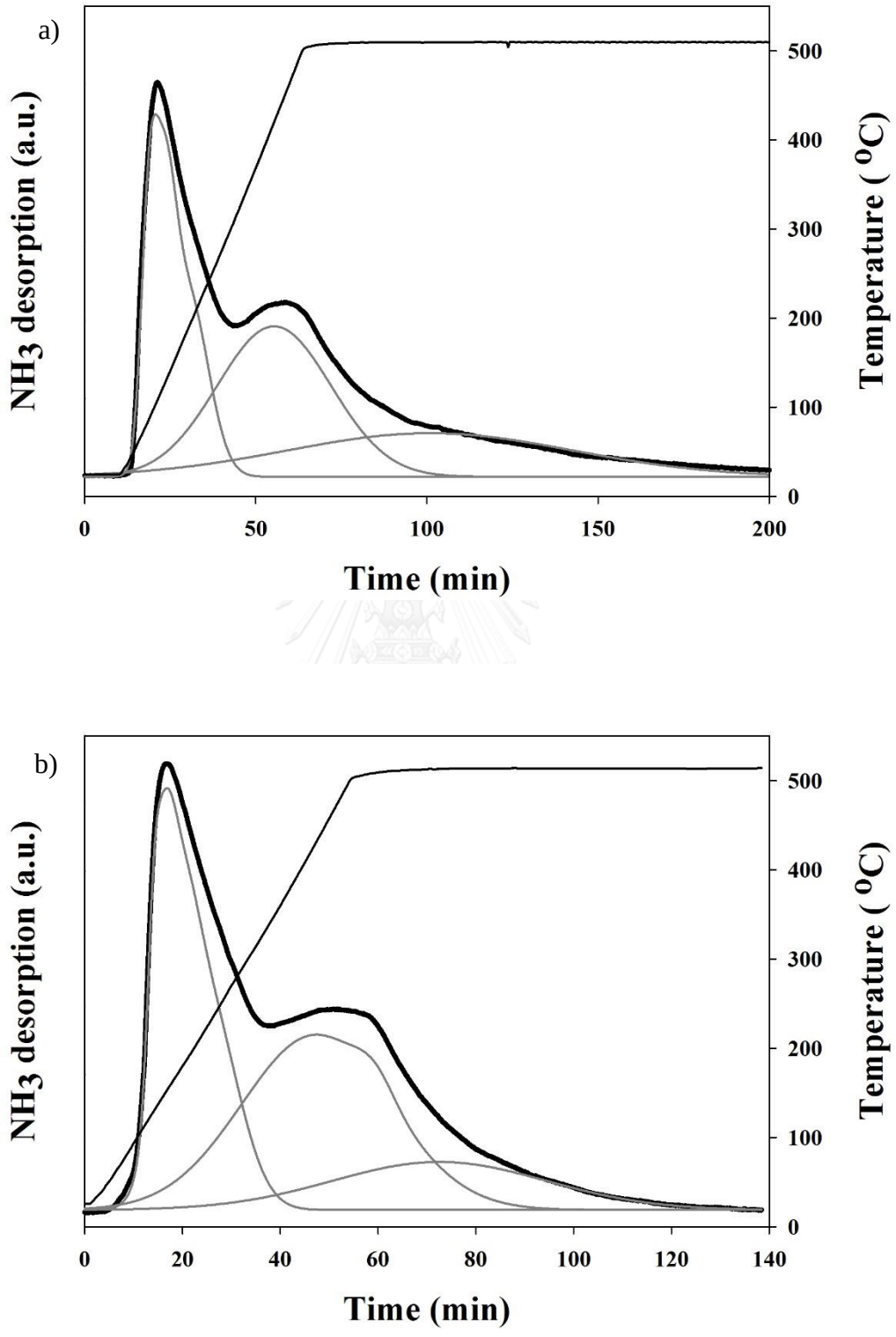

Figure 4.4 NH_3-TPD profiles of all prepared catalysts (a) CHI00, (b) CHI30, (c) CHI50 and (d) CHI100.

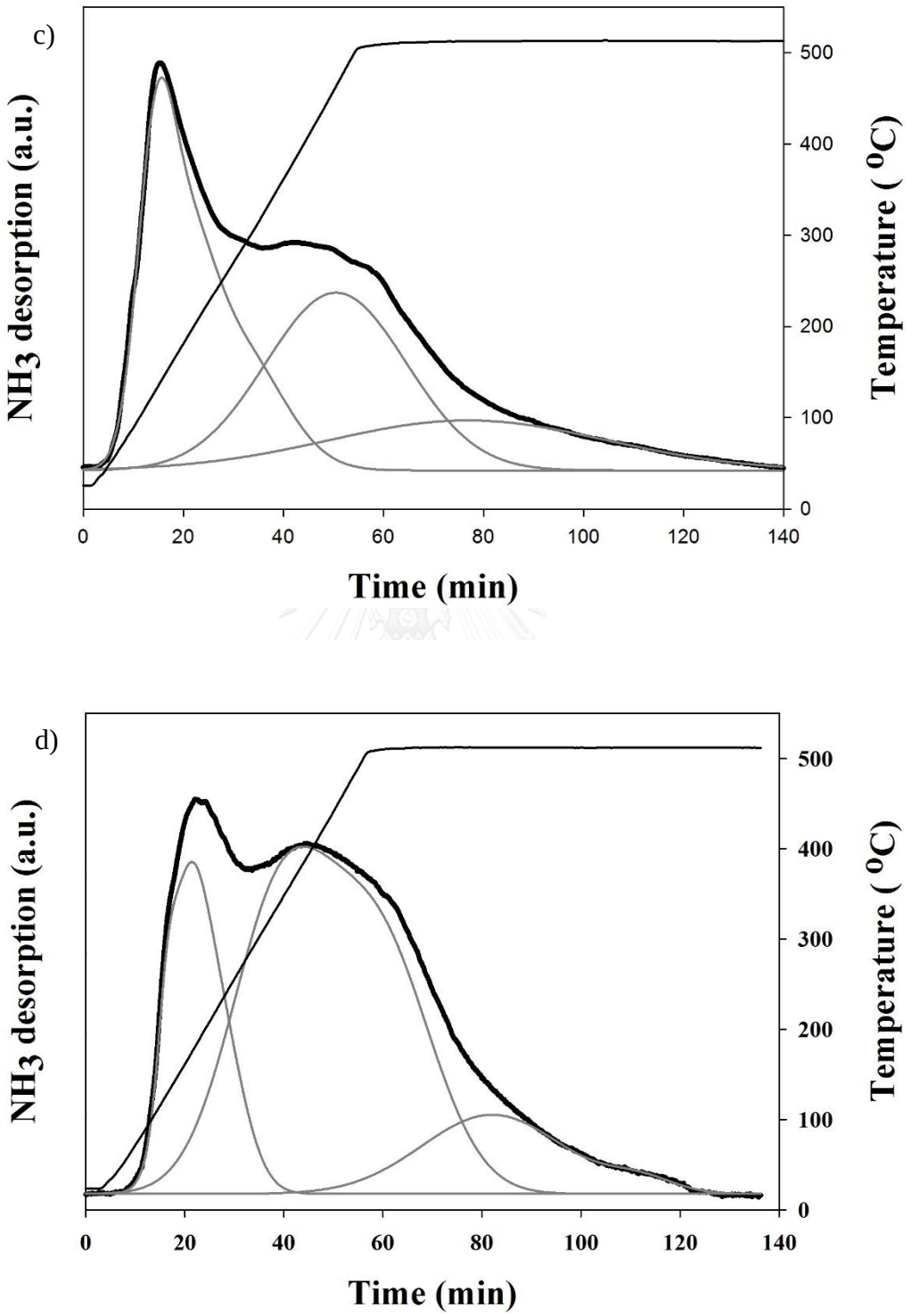

Figure 4.4 (cont.) NH_3-TPD profiles of all prepared catalysts (a) CHI00, (b) CHI30, (c) CHI50 and (d) CHI100.

Table 4.2 NH_3 TPD analysis of all prepared catalysts

Catalysts	Acid sites distribution (%)		Total acid site	Acid site density (μmol NH_3/m^2)		
	Weak	Moderate to Strong	(μmol NH_3/g)	Weak	Moderate to Strong	Total
CHI00	34.64	65.36	1136.99	1.53	2.89	4.42
CHI30	40.01	59.99	1332.39	2.09	3.15	5.24
CHI50	27.58	72.43	1292.89	2.12	5.58	7.70
CHI100	22.49	77.51	804.02	1.32	4.55	5.87

The total amount of acid sites determined either per mass of catalysts or per surface area is practically equal for all catalysts as given in **Table 4.2**. The total acid sites for all catalysts were ranged from 804 to 1,436 μmol NH_3/g. It can be observed that mainly the acid sites distribution was consistent upon the moderate to strong acid sites. In addition, if the NH_3 desorption data are expressed in per unit surface area, the density of surface acid sites for all alumina catalysts will approximately range between 4 to 7 μmol NH_3/m^2. The CHI30 catalyst exhibited the highest concentration of the acid sites at 1,436 μmol NH_3/g, while the CHI50 catalyst displayed the highest acid density on the surface of the catalyst at 7 μmol NH_3/m^2. This crucial characteristic will be used to explain the catalytic behaviors for all catalysts during ethanol dehydration reaction.

4.1.2 Ethanol dehydration reaction

In order to determine the catalytic behaviors of all prepared catalysts, the conversion of ethanol and the selectivity to products such as ethylene, diethyl ether and acetaldehyde as a function of temperature were investigated in vapor phase ethanol dehydration. The experiment was performed with the same catalyst weight. The dehydration activity is already significant at ca. 200 ^oC and total at 400 ^oC as displayed in **Figure 4.5a** and **Figure 4.5b**.

a)

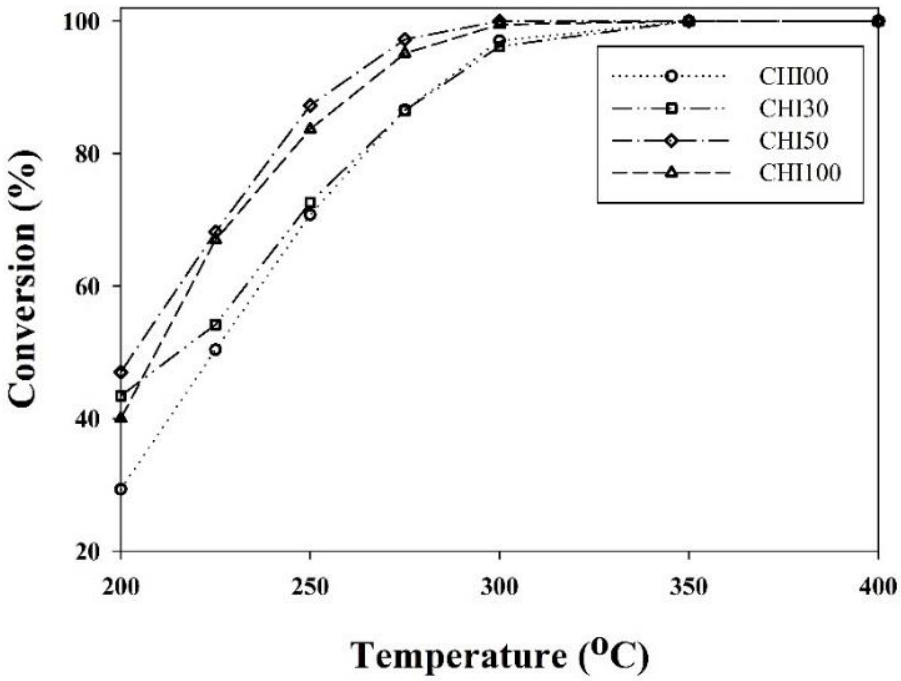

b)

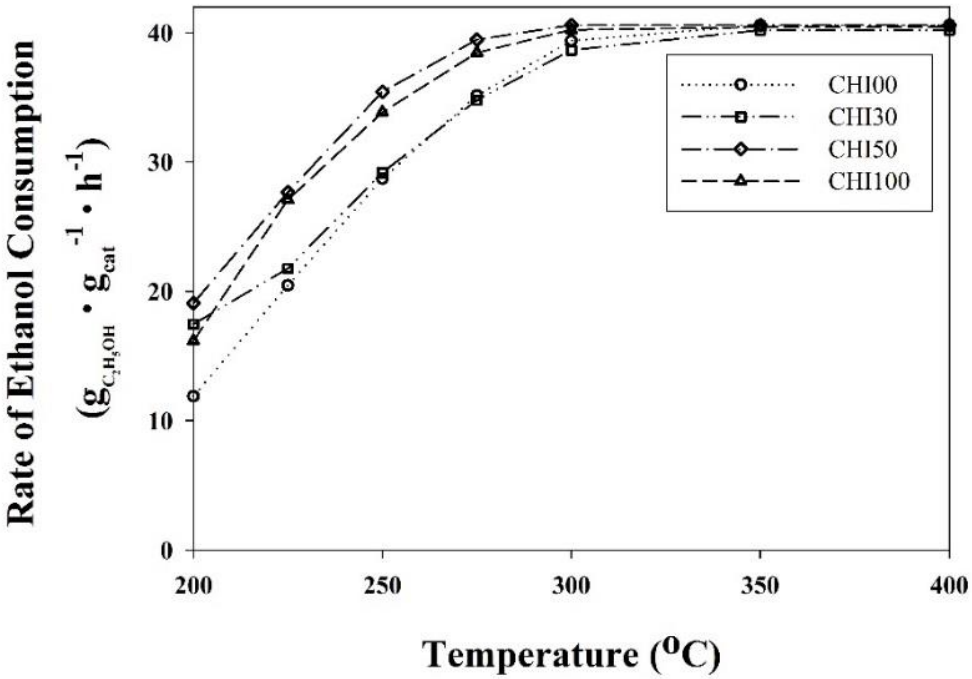

Figure 4.5 Catalytic activities of all prepared catalysts (a) conversion and (b) reaction rate.

Typically, ethanol conversion increases during the reaction temperature is raised. The obtained catalytic activity for all catalysts can be achieved completely for ethanol conversion at 300 ^{o}C. The obtained conversions were ranged between 96.2 to 100% in accordance with the ethanol consumption rate of 2.4 to 8.3 $g_{Ethanol} \cdot g_{cat}^{-1} \cdot h^{-1}$, respectively. The dehydration activity decreased in the order: CHI50 > CHI100 > CHI30 > CHI00 during the reaction temperature around 200 to 300 ^{o}C. Moreover, it can be observed that the catalytic activity of the mixed of γ- and χ-alumina (CHI30 and CHI50) and native χ-phases alumina (CHI100) exhibited remarkably higher catalytic conversion than the native γ-alumina (CHI00) at the temperature of 200 ^{o}C. During the reaction temperature between 225 to 275 ^{o}C, it was attractively observed that CHI50 and CHI100 still present distinctly high catalytic conversion, whereas CHI30 was not significantly different in the catalytic activity with CHI00. In a number of papers, it was observed that the acidity over solid catalysts predominantly plays an important role on alcoholic dehydration. The presence of strong acid sites on alumina catalysts increases the alcoholic conversion. In the contrary, the concentration of the acid sites (μmol NH_3/g) was a more dominant factor than their strength. It was due to the reaction is not specifically sensitive to the strength of the acid sites [5, 59, 60]. In contrast, this result indicated that the dehydration activity was independent on the concentration of the acid sites on the catalyst. Evidently, this is consequence of an inductive effect of transition phase on alumina catalysts as being observed from the result that CHI100 exhibits higher catalytic activity than CHI00 in spite of its lower acidity. Moreover, the effect of different morphologies on the physicochemical, surface and catalytic properties of γ-alumina was also explained [4]. Interestingly, this catalytic observation displayed the ethanol conversions and reaction rate related to the acid density (μmol NH_3/m^2) as mentioned in **Table 4.2**. The obtained highest activity of CHI50 was in accordance with the largest total acid density (7.7 μmol NH_3/m^2) while the lowest activity of CHI00 was corresponding to the least total acid density (4.4 μmol NH_3/m^2). The previous work demonstrated that the O atom of adsorbed ethanol interacts strongly with surface Al (Lewis acid) sites to form ethoxide species [61]. A bimolecular nucleophilic substitution mechanism is preferred with two adjacent ethanol molecules probably co-adsorb on two nearby neighboring sites and react to form an ethanol dimeric species at

low temperature. The shorter distances between two nearby neighboring sites probably lead to rapidly react to form diethyl ether as seen in **Scheme 4.1**.

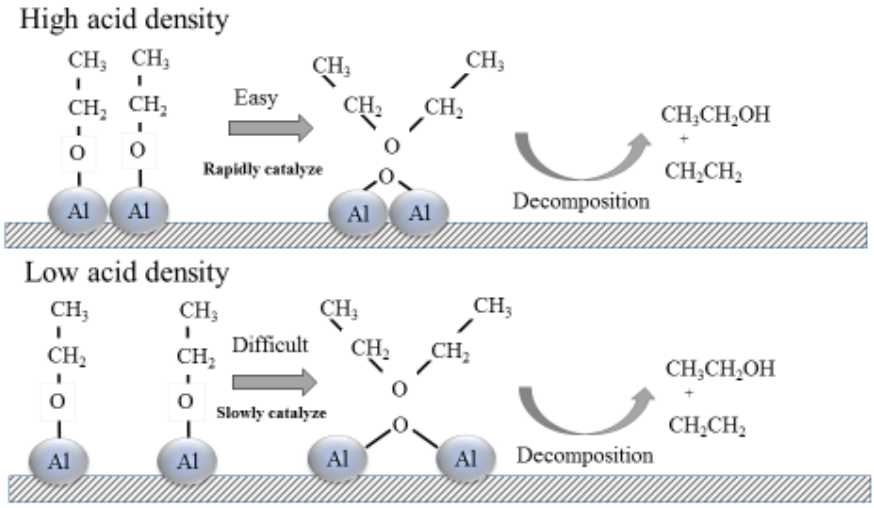

Scheme 4.1. The conceptual pathway for ethanol conversion

This reason can be used to demonstrate that why diethyl ether selectivity is dominant at low temperature [50]. This is difficult to understand the important factor of catalytic dehydration, while the mechanistic detail of ethylene formation is unclear. In a number of papers, it was demonstrated the ethylene and diethyl ether formation. The catalytic process may occur via two reaction pathways. The possible pathway includes diethyl ether acts as a reaction intermediate, which is subsequently decomposed to ethylene and ethanol [62] as seen in **Scheme 4.1**.

Ethanol conversion can be acid and base catalyzed, therefore the selectivity to a desired products can be easily related to the characteristics of the surface. Besides, the measurement of elemental composition on the catalyst surface such as XPS is famous as one of the most powerful techniques that can be also applied to obtain the information of the oxidation state and chemical environment of the elements present on the surface of the catalyst. The XPS analysis, that has the depth of ca. 10 $\mathring{A}$, convinces

the external surface elemental concentrations influencing on the catalytic activity. The XPS data for all alumina catalysts are given in **Table 4.3**. The Al 2p and O 1s peaks were detected at the binding energy between 74.10 to 75.05 eV and 531.00 to 531.95 eV, respectively. It revealed that the atomic ratio of Al 2p over O 1s is slightly lower than the expected composition of Al_2O_3, which has the value of 0.67. It was observed that the atomic ratios of Al 2p over O 1s in the catalyst samples were ranged from 0.478 to 0.530. Moreover, this ratio slightly decreased with increasing the quantity of χ-phase from 0 to 100%. This reason becomes apparent from the possessed defect spinel lattices, which are slightly tetragonal distorted that can be pronounced for γ-alumina [4, 63]. Hexagonal χ-alumina seems to possess a layer structure. The arrangement of anions inherited from gibbsite, whereas the aluminum cations occupy octahedral sites within the hexagonal oxygen layer [39].

In principle, the transition alumina is generally formed aluminum monohydroxide and trihydroxide. The dehydration process of transition alumina in air takes place, the loss of water by desorption of physisorbed water or by condensation of hydroxyl group occurs. The dehydroxylation condition predominantly presents that the condensation of two nearby surface hydroxyls forms water molecule on the surface during the formation of alumina catalysts as seen in **Scheme 4.2** [57].

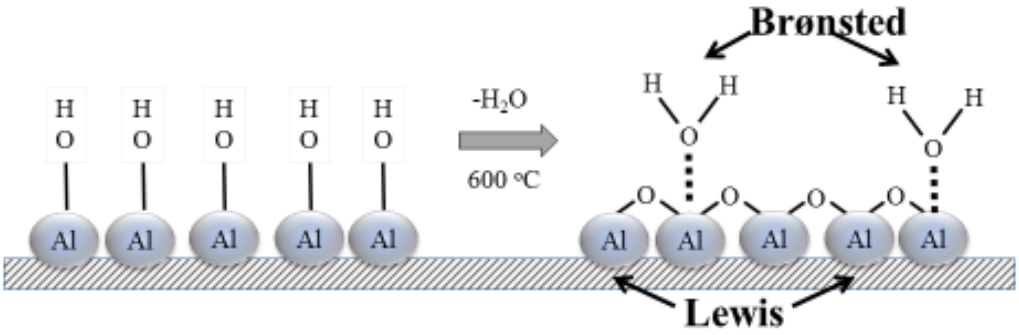

Scheme 4.2. Formation of the acid site on alumina surface by dehydroxylation process [57]

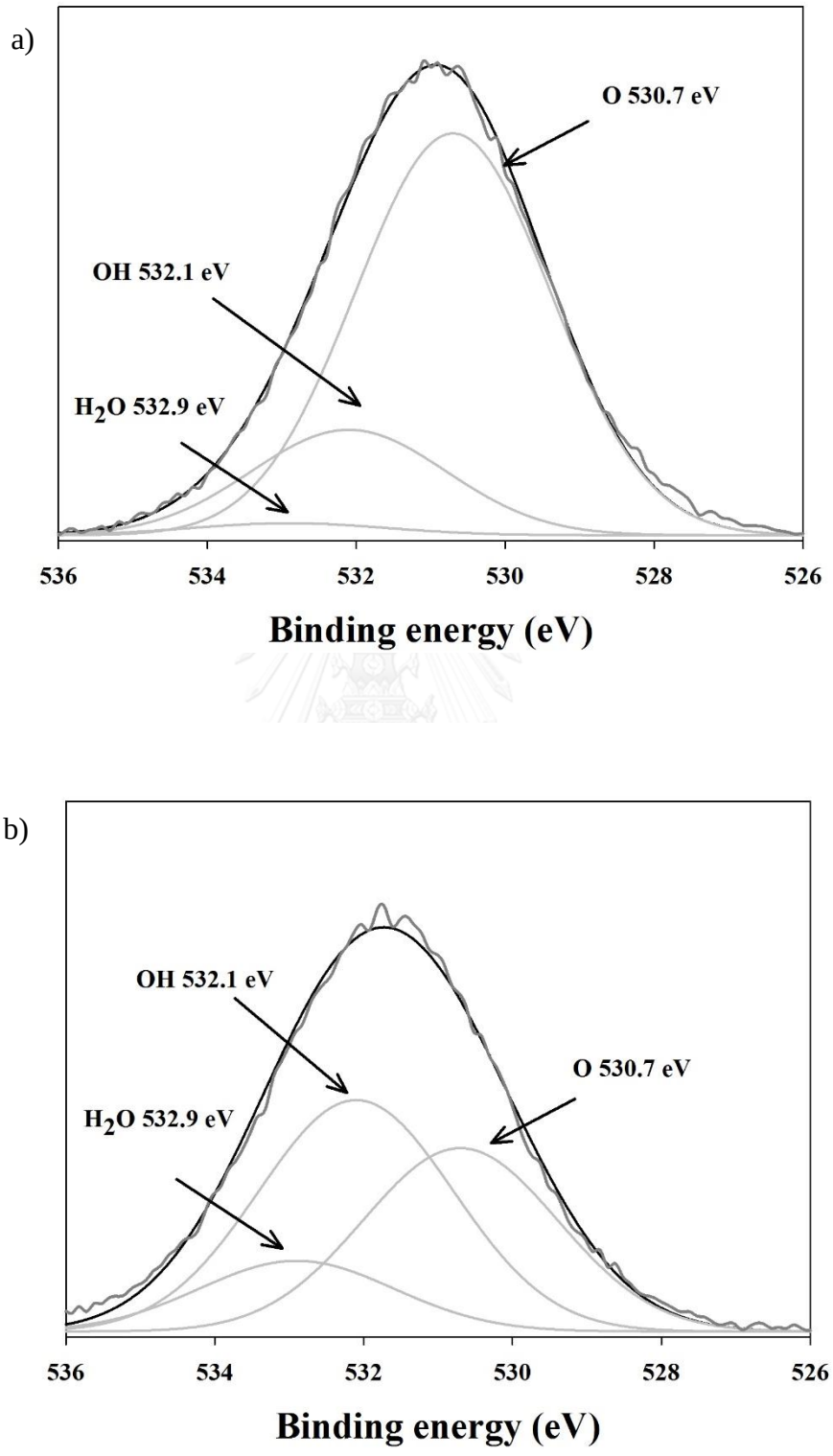

Figure 4.6 XPS analysis for O 1s spectra of all prepared catalysts (a) CHI00, (b) CHI30, (c) CHI50 and (d) CHI100.

c)

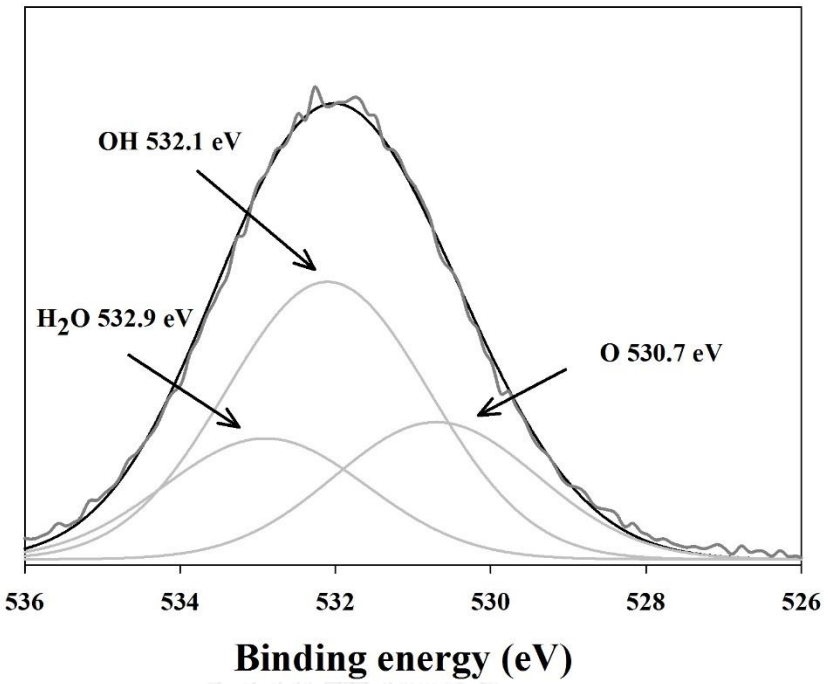

d)

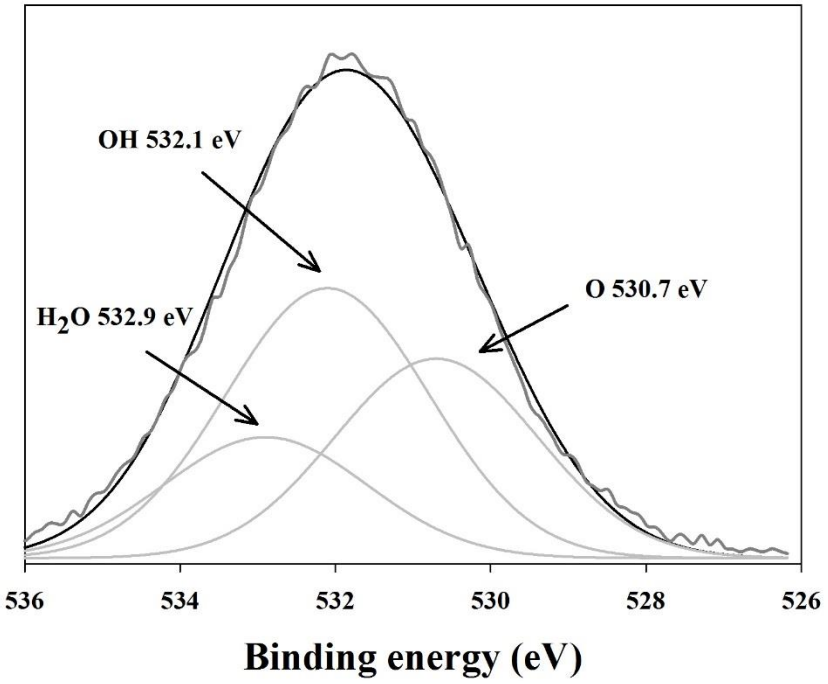

Figure 4.6 (cont.) XPS analysis for O 1s spectra of all prepared catalysts (a) CHI00, (b) CHI30, (c) CHI50 and (d) CHI100.

As mentioned above, the O 1s spectra show the presence of three different oxygen species. The spectra analysis of XPS core level spectra focusing on O 1s was used to identify the oxygen species on the surface of all alumina catalysts as seen in **Figure 4.6a-4.6d**. The deconvolution of the O 1s spectra, separated and fitted into three signals can be generally attributed to the different species of atomic oxygen such as H_2O, OH and O on the surface. Normally, the crystal structure of corundum has lattice oxygen (O), which is in the form of aluminium oxide in accordance with binding energy of 530.7 eV [64]. Besides, the corundum structure of alumina contains O 1s peak including atomic oxygen that indicates the surface hydroxyl (OH) and adsorbed water (H_2O) corresponding to 532.1 and 532.9 eV, respectively. All three signals exhibit the similar FWHM about 3.0 eV. The atomic concentrations of each O 1s species for all catalysts were fitted and determined as mentioned in **Table 4.3**. This result presents that the CHI00 catalyst exhibited the highest area fraction of the lattice oxygen about 77% from the total atomic oxygen, while the CHI50 catalyst displayed the maximum value from O1s peak of the adsorbed water ca. 23% from the total atomic oxygen.

The alumina catalysts predominantly lead to the formation of ethylene and diethyl ether either with minor amount of acetaldehyde. The process involves the unimolecular dehydration of ethanol leading to ethylene formation, while the bimolecular reaction produces diethyl ether. The selectivity towards ethylene increased with increasing reaction temperature (**Figure 4.7a**), while the selectivity towards diethyl ether apparently decreased (**Figure 4.7b**). At low temperature, ethanol dehydration is predominantly a bimolecular reaction whilst the unimolecular reaction route prevails at high temperature [46, 65, 66]. On the contrary, the mechanism of ethylene formation has been expected from the decomposition of diethyl ether at higher temperature [67, 68]. The selectivity towards ethylene reaches around 91 to 98% at 300 ^{o}C. The obtained selectivity to ethylene for all catalysts was approximately completed at the reaction temperature range between 300 to 350 ^{o}C. It decreased in the following order: CHI50 > CHI100 > CHI30 > CHI00 during the reaction temperature between 200 to 300 ^{o}C. This result can be likely illustrated that the dehydration of ethanol to ethylene corresponded to the amount of adsorbed water (Brønsted acid) on the surface, which was evaluated from the O 1s core level spectra as shown in **Table 4.3** that the O

1s of H_2O fraction of CHI50 (22.6%) > CHI100 (20.5%) > CHI30 (14.6%) > CHI00 (2.3%). The predominant concentration of adsorbed water on the surface of CHI50 was received while the most efficient selectivity to ethylene was detected. This relation is in good agreement with the Brønsted acid that being active sites as the direct conversion of ethanol into ethylene via elimination reaction [9]. Recently, the appearance of hydrated silver cations in AgPW salts plays important role in generation of protons, which is available for an acidic type reaction [69]. This is important because the water molecules hydrated silver cations are necessary to generate protons needed to acidic type reaction. Moreover, a moderate surface acid density of ZSM-5 seems to be suitable for bioethanol to ethylene reaction [70]. In addition, CHI100 has a higher selectivity to ethylene than that of CHI00. This attractive observation is consequence of an inductive effect of transition phase on alumina catalysts. Moreover, the possible pathway includes diethyl ether formation and decomposition leads to ethylene production as mentioned before. The higher efficiency of diethyl ether formation probably took place to higher ethylene formation rate. However, the distinct catalysts exhibit the variation of decomposition rate and product distribution in diethyl ether decomposition [62].

The formation of diethyl ether begins around 43 to 62% at 200 ^{o}C. The obtained selectivity to diethyl ether for all catalysts was absolutely disappeared at the reaction temperature of 300 ^{o}C. It decreased in the following order: CHI00 > CHI30 > CHI100 > CHI50 during the reaction temperature between 200 to 300 ^{o}C. It can be observed that the selectivity to diethyl ether is disproportionation to the selectivity to ethylene. The highest ethylene selectivity of CHI50 was obtained, while the lowest efficient selectivity to diethyl ether was found. The formation towards acetaldehyde can be observed at the reaction temperature around 200 to 350 ^{o}C (**Figure 4.8**). It decreased in the following order: CHI00 > CHI30 > CHI100 > CHI50.

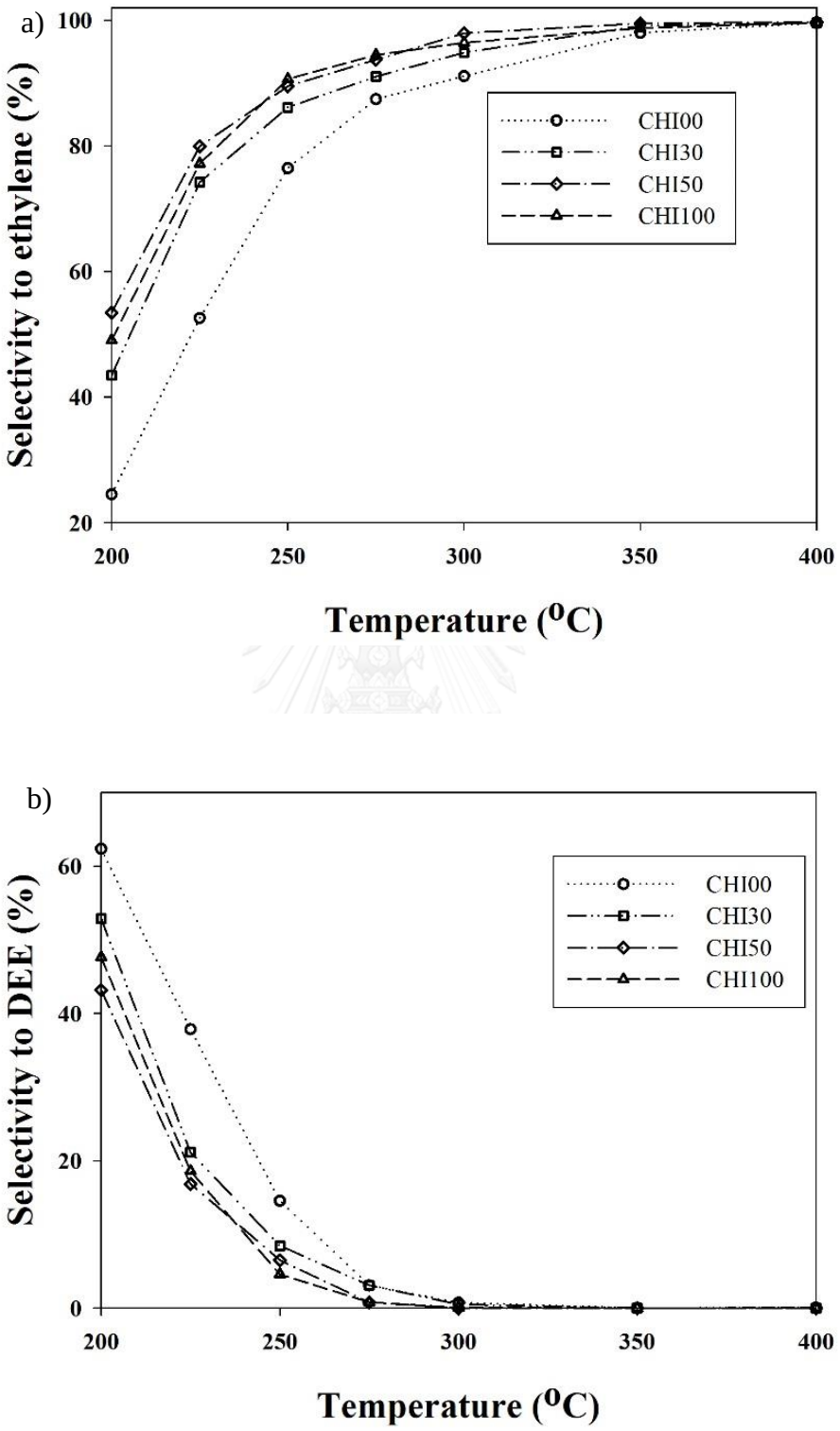

Figure 4.7 Selectivity to products of all prepared catalysts (a) ethylene selectivity, (b) diethyl ether selectivity.

Table 4.3 XPS analysis of all prepared catalysts

Catalysts	BE for Al 2p(eV)	BE for O 1s(eV)	Atomic concentration (%)		Atomic ratio	O 1s peak area fraction (%O 1s)			O 1s atomic concentration (%)		
			Al 2p	O 1s	Al/O	H_2O	OH	O	H_2O	OH	O
CHI00	74.10	531.00	34.61	65.39	0.530	0.023	0.203	0.774	1.52	13.28	50.59
CHI30	74.30	531.70	34.37	65.63	0.524	0.146	0.477	0.378	9.56	31.29	24.79
CHI50	75.05	531.95	32.95	67.05	0.491	0.226	0.518	0.256	15.14	34.74	17.17
CHI100	74.90	531.80	32.36	67.64	0.478	0.205	0.457	0.338	13.86	30.93	22.85

Moreover, the selectivity to acetaldehyde from the mixed phase of γ- and χ-alumina (CHI30 and CHI50) and native χ-phases alumina (CHI100) remarkably displayed the low selectivity at 4%, while the native γ-alumina (CHI00) exhibited 14% at the reaction temperature of 200 ^{o}C. This evidence can be alternatively used to suggest that the appearance of χ-phases promoted the inhibition of dehydrogenation reaction. However, the suitable temperature of the acetaldehyde formation was seen around 275 ^{o}C. The basic catalysts take place for the dehydrogenation of ethanol to produce acetaldehyde [71]. Moreover, the formation of acetaldehyde probably displayed the presence of redox sites on the catalyst [72].

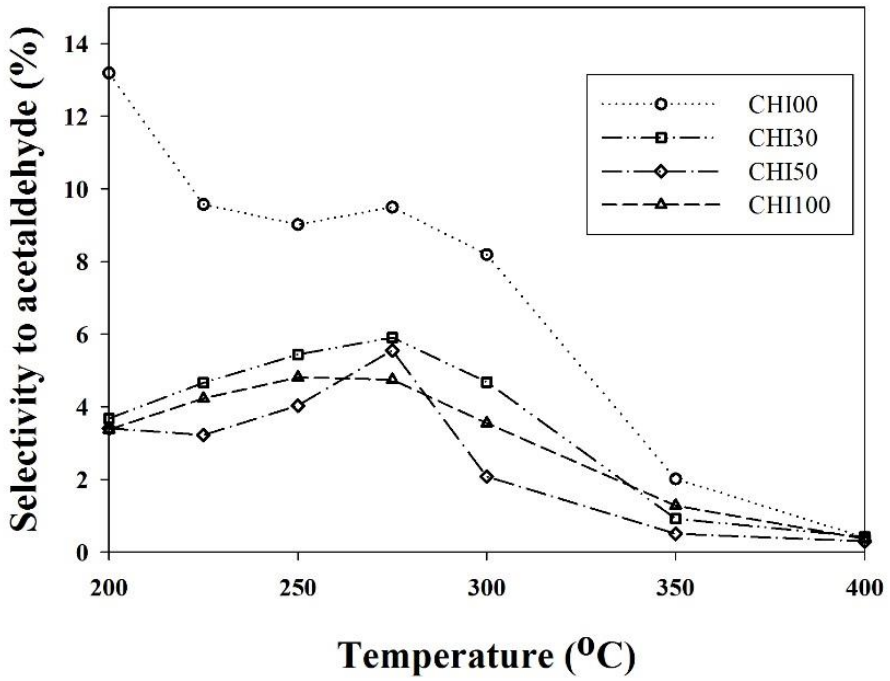

Figure 4.8 Selectivity to acetaldehyde of all prepared catalysts.

In summary, the appearance of metastable χ-alumina structure based on hcp close packing exhibited better catalytic activity and ethylene selectivity than γ-alumina with the ccp close packing. Thus, the introduction of metastable χ-alumina structure into γ-alumina enhanced catalytic activity and ethylene selectivity. The increased catalytic activity is due to an increase in acid density, whereas increased O 1s atoms in the adsorbed water apparently respond for the enhancement of ethylene selectivity. As the results, the CHI50 distinctly exhibits good performance in ethylene synthesis, even

at the reaction temperature lower than 300 ^{o}C. It is likely that the presence of O 1s atoms in the adsorbed water is related to the Bronsted acid site.

4.2 Oxidative dehydrogenation of ethanol over silver-lithium supported on the mixed phase alumina catalysts

This section describes the influences of Ag/Li modification on mixed-phase alumina was investigated for oxidative dehydrogenation of ethanol to acetaldehyde. Moreoveer, the preparation and characterization of the AgLi catalysts was investigated. In addition, the adsorption of H_2O onto the A and B type steps on an Ag single crystal by temperature programmed desorption was studied for surface-structure sensitive.

4.2.1 Characteristics

The physical properties of alumina supports and catalysts prepared by the solvothermal synthesis were obtained from the XRD and N_2 physisorption data. The desirable phases of nanocrystalline alumina depend on the synthesis solvents as shown in **Table 4.4**. XRD measurement was performed to identify the bulk phase of nanocrystalline alumina and silver-lithium catalysts. The γ-alumina support (CHI00), which was produced using only 1-butanol as the synthesis solvent was confirmed by the diffraction peak at 32 37, 39, 45, 61 and 66^{o}. However, during using toluene as the synthesis solvent, the characteristic diffraction peak of χ-phase was remarkably appeared at 43^{o} for χ-alumina support (CHI100). In addition, the γ- and χ-phase compositions of mixed phase alumina (CHI50) were determined and confirmed by the area of characteristic peak at 43^{o}. The obtained alumina supported consisting of γ-phase, χ-phase and the mixed between γ- and χ-crystalline alumina (1:1) are denoted as CHI00, CHI100 and CHI50, respectively. The XRD patterns of silver-lithium supported on distinct type nanocrystalline alumina are shown in **Figure 4.9**. The reflection attributed to metallic silver species is observed at $2\theta \approx 38.1$ and 44.3^{o} [73] while oxygenate silver is observed at $2\theta \approx 33^{o}$, according to the previous literature data [74]. The obtained XRD patterns were observed only the typical pattern for transition alumina except for any additional peaks from silver phase. The absence of diffraction

pattern for metallic and oxygenate silver probably due to the low loading of silver or well disperse of silver in the catalysts. In addition, the strong intensity of alumina probably disturbed the observation of silver peak.

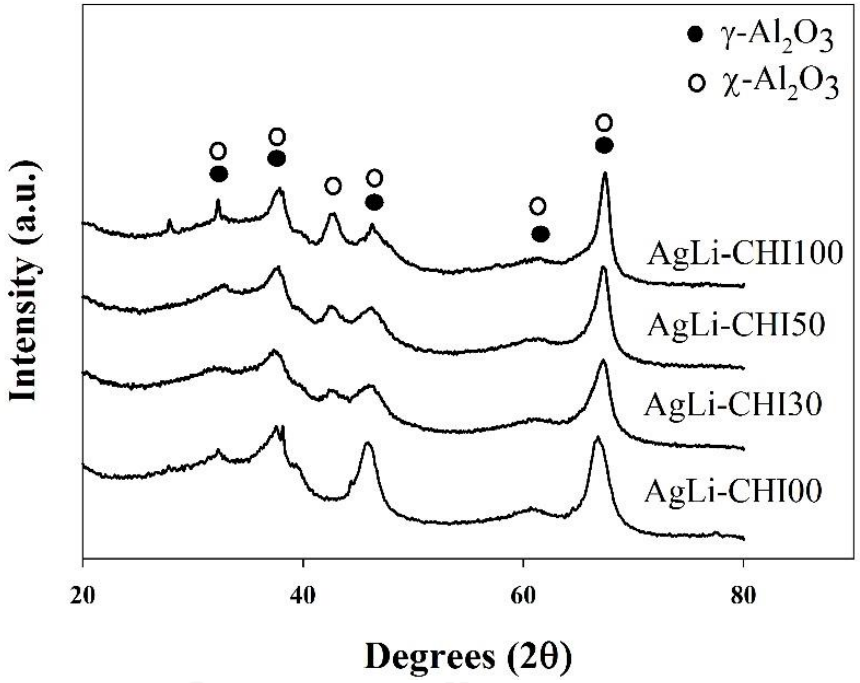

Figure 4.9 XRD patterns of all prepared silver-lithium catalysts.

The structural parameters of distinct alumina supports and silver-lithium based catalysts derived from N_2 physisorption isotherms are summarized in **Table 4.4**. The BET surface area of the nanocrystalline alumina decreased from 257 to137 m^2/g with the larger quantity of χ-phase, whereas the average pore diameter was rather similar for the different nanocrystalline alumina. The pore size distribution confirms isotherm assertion and mesoporous structure for all prepared nanocrystalline alumina. The observed mesoporosity can be probably attributed to the voids from inter-connected between primary particles. The surface area of AgLi-CHI00 catalyst was much lower than its alumina supports, whereas AgLi-CHI30, AgLi-CHI50 and AgLi-CHI100 only

had a slight effect. The decreased surface area for all silver-lithium based catalysts can be attributed to the lower pore volume of all catalysts.

Table 4.4 BET surface area, pore volume and pore diameter of all prepared silver-lithium catalysts.

Catalysts	A_{BET} (m^2/g)	V_p (cm^3/g)	D_{BJH} (nm)
AgLi-CHI00	158	0.39	7.28
AgLi-CHI30	148	0.24	4.13
AgLi-CHI50	142	0.32	5.57
AgLi-CHI100	109	0.42	9.21

The representative of transmission electron micrograph of three distinct silver-lithium based catalysts are shown in **Figure 4.10**. TEM images are representative for the obtained alumina morphology and homogeneous distribution of silver and lithium particles on alumina supports. This is likely that the wrinkled sheet morphology is attributed to the presence of native γ- phase (AgLi-CHI00 as seen in **Figure 4.10a**), while χ-phase is present as the spherical shape (AgLi-CHI100 as seen in **Figure 4.10d**) [33]. The mixed between γ- phase and χ-phase represent the combination of morphology between wrinkled sheet and spherical shape (AgLi-CHI50, AgLi-CHI50 as seen in **Figure 4.10b** and **4.10c**). Lithium deposits, which appear as transparent small spherical shape, well dispersed on nanocrystalline alumina. Silver particles obscurely observed as seen in AgLi-CHI00, whereas silver particle appears as dark spherical shape as seen in AgLi-CHI30, AgLi-CHI50 and AgLi-CHI100.

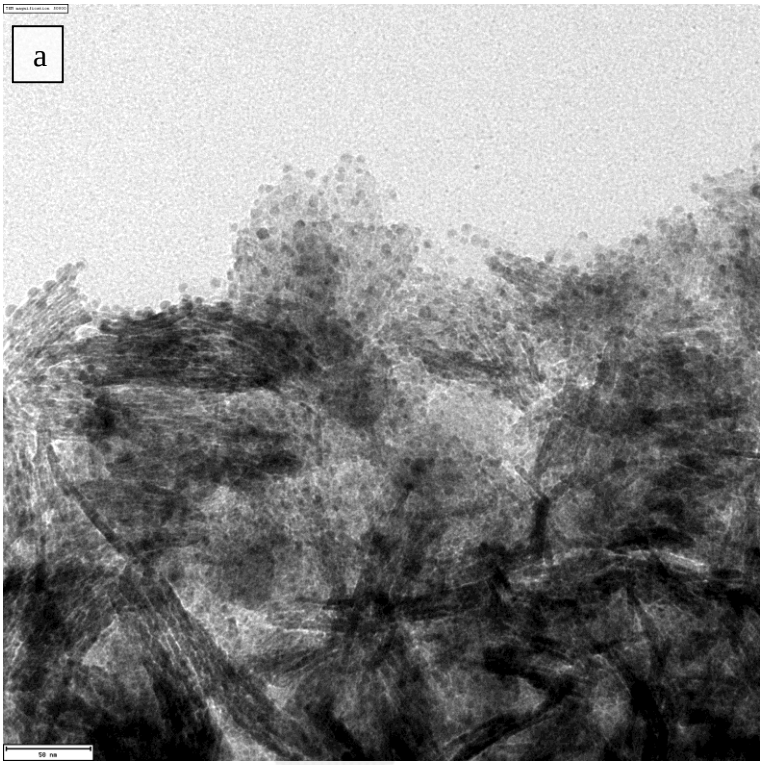
a
50 nm

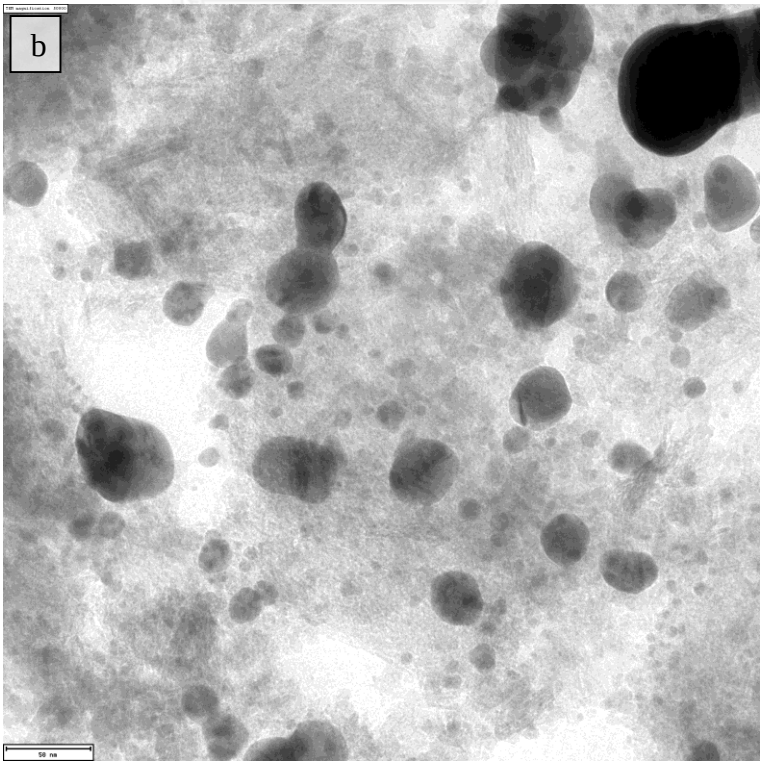
b
50 nm

Figure 4.10 TEM micrographs of all prepared silver-lithium supported on pure γ- , χ- and the mixed phase alumina catalysts (a) AgLi-CHI00, (b) AgLi-CHI30, (c) AgLi-CHI50, (c) AgLi-CHI100.

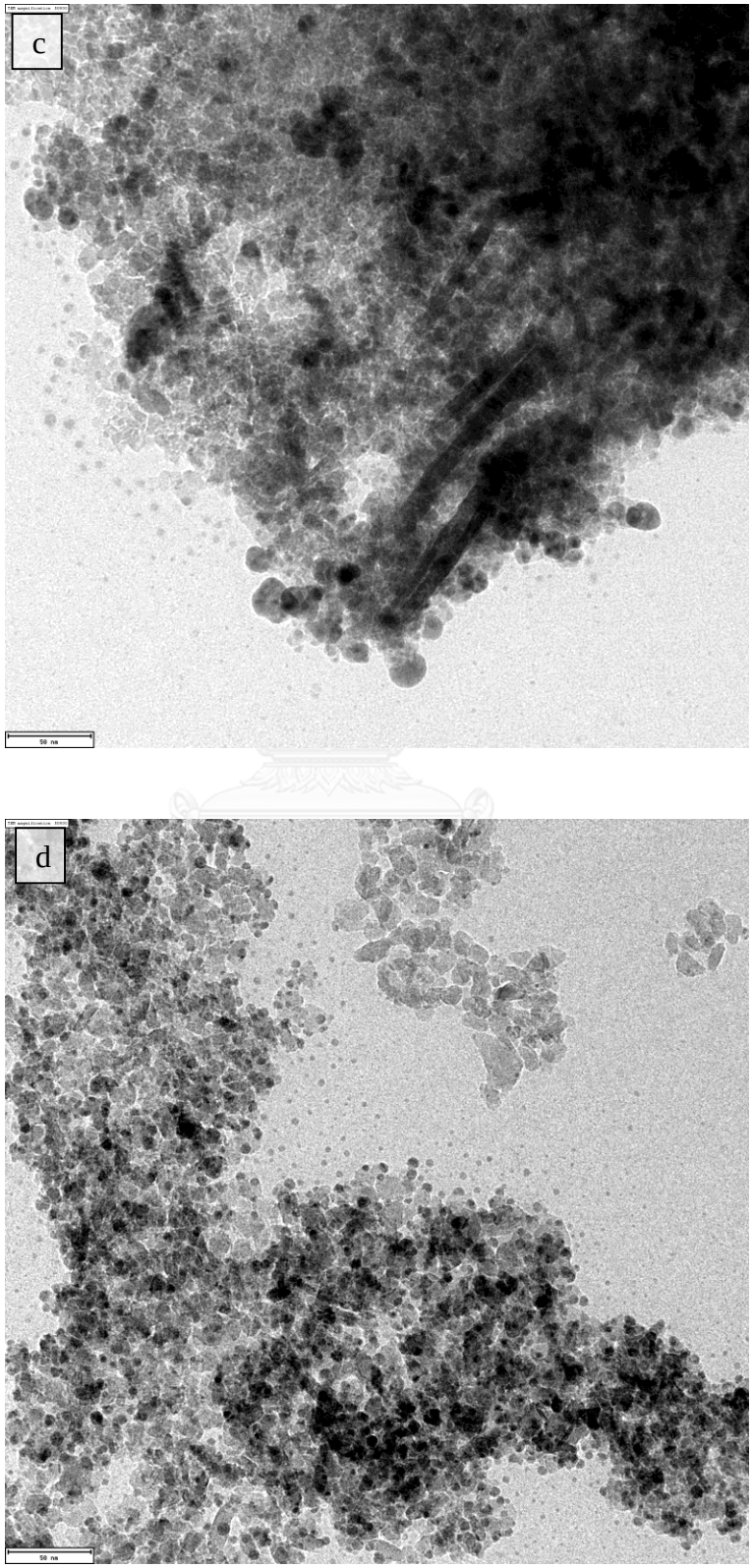

Figure 4.10 (cont.) TEM micrographs of all prepared silver-lithium supported on pure γ- , χ- and the mixed phase alumina catalysts (a) AgLi-CHI00, (b) AgLi-CHI30, (c) AgLi-CHI50, (c) AgLi-CHI100.

SEM/EDX and ICP-OES were also conducted in order to study the chemical distribution and chemical composition of the catalysts, respectively. The amount of silver, lithium alumina and oxygen are summarized. It was well known that the silver concentrations at bulk were ranged between 4.7 and 4.8 wt%, while Li contents were at 0.69 and 0.72 wt% for all silver-lithium based catalysts. However, the element concentration from the EDX analysis, which is not a bulk (but rather surface) analytical tool, gives information down to a depth of approximately 50 nm from the typical external granule. To compare the silver distribution between bulk and surface analysis, the concentration of element data are expressed in Ag/Al ratio. The ICP results can be observed that the Ag/Al ratio at bulk for all silver-lithium based catalysts were about 0.11. However, the ratio of Ag/Al for AgLi-CHI00, AgLi-CHI30 and AgLi-CHI50 from EDX analysis were slightly higher than ICP measurement, while the ratio was distinctly higher for AgLi-CHI100 catalyst. This was due to the silver accumulated on the external surface of alumina support.

4.2.2 Oxidative dehydrogenation of ethanol

In order to determine the catalytic behaviors of all silver-lithium based catalysts, the conversion of ethanol and the selectivity to products such as acetaldehyde, carbon monoxide and carbon dioxide as a function of temperature were investigated in vapor phase oxidative dehydrogenation of ethanol. Generally, the basic catalysts take place for the dehydrogenation of ethanol to produce acetaldehyde [12]. Moreover, the formation of acetaldehyde probably displayed the presence of redox sites on the catalyst [13]. The oxidative dehydrogenation activity is apparently significant at ca. 150 ^{o}C and total at 400 ^{o}C as displayed in **Figure 4.11**. Typically, ethanol conversion increases during the reaction temperature is raised. The obtained catalytic activity for all catalysts can be achieved completely for ethanol conversion at 275 ^{o}C. The obtained conversions were ranged between 96 to 100%. The oxidative dehydrogenation activity decreased in the order: AgLi-CHI50 > AgLi-CHI30 > AgLi-CHI00 > AgLi-CHI100 during the

reaction temperature around 150 to 275 ^{o}C. It can be observed that the catalytic activity of the silver-lithium supported on the mixed γ- and χ-phase alumina exhibited remarkably higher catalytic activity than the native γ- and χ- phases alumina. The previous studies [22] indicated that the platinum supported on mixed γ- and χ-alumina displayed higher Pt dispersion and catalytic conversion for carbon monoxide oxidation. Moreover, the presence of χ-phase in alumina support resulted in higher dispersion of cobalt as well as higher CO hydrogenation activities [21, 32]. However, the relationships between catalytic activity and catalyst properties in term of basicity, oxidation state and reduction behavior were investigated.

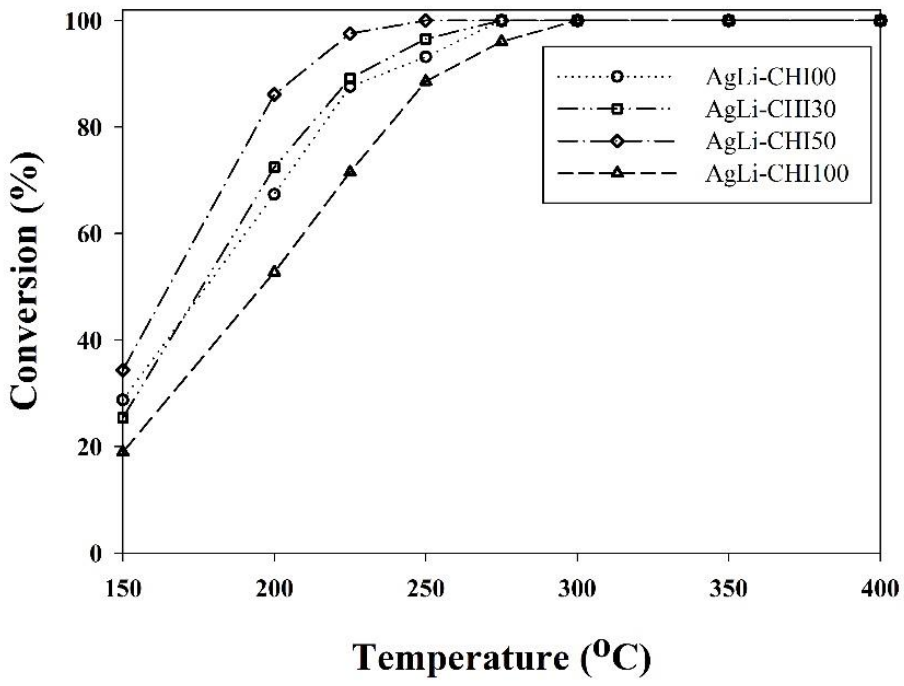

Figure 4.11 Catalytic activities of all prepared silver-lithium catalysts.

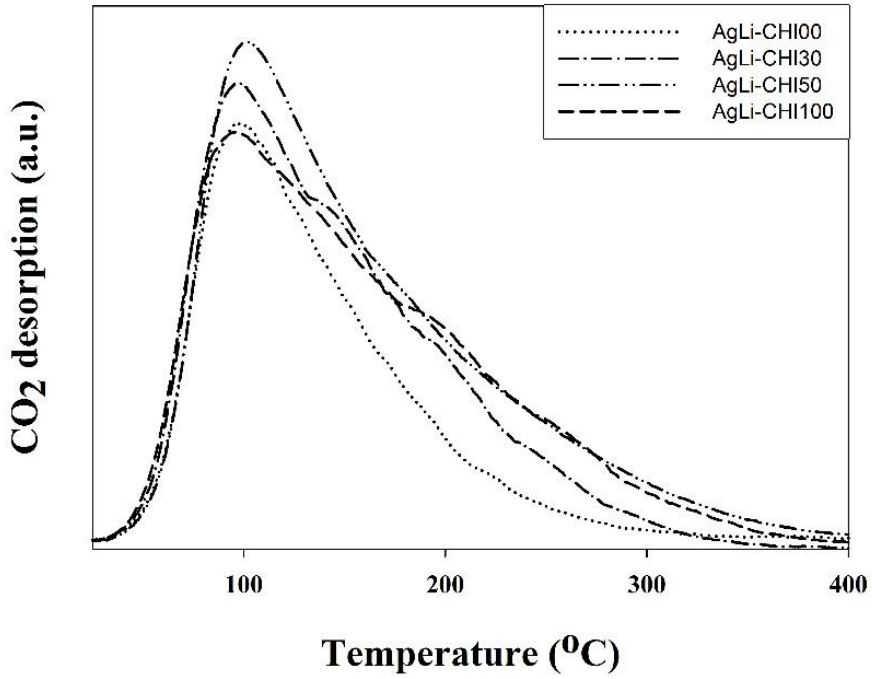

Figure 4.12 CO_2 TPD analysis of all prepared silver-lithium catalysts**.**

Oxidative dehydrogenation of alcohols is well known as a base-catalyst reaction. In fact, an acidic gas such as CO_2 can adsorb on the catalyst surface that is strongly influenced by the basic property of the catalysts. It can be assumed in principal that one CO_2 molecule adsorbs on the basic site of the catalyst after desorption under He flow at room temperature, the physisorbed CO_2 was removed. A qualitative measurement of the basic site strength were obtained by TPD of chemisorbed CO_2. The CO_2-TPD profiles occur at low desorption temperature around 89^oC corresponding to CO_2 (bicarbonate species) adsorbed on the weak basic site (OH groups) [75]. While the medium (150^oC) and high (244^oC) desorption temperature can be attributed to CO_2 interaction on the medium (M-O^{2-} pairs) and strong (O^{2-} ions) [76]. The CO_2-TPD profiles of silver-lithium based catalysts occur most likely the low temperature desorption as shown in **Figure 4.12**. However, the appearance of χ-phase in the silver-lithium based catalysts represent much more medium and strong basic sites leading to the shoulder peak observation above 120^oC. The total evolved CO_2 was obtained by integration of TPD curves as calculated in term of μmol CO_2/g. The result can be

observed that the CO_2 uptake remarkably increased, according to the appearance of χ-Al_2O_3. However, it can be clearly observed that AgLi-CHI50 provides the highest value of basic site. This was in accordance with the highest catalytic activity. Moreover, it can be suggested that more basic site generated on interface between χ- and γ-Al_2O_3. The CO_2 uptake decreased in the order: AgLi-CHI50 (1212 μmol CO_2/g) > AgLi-CHI100 (979 μmol CO_2/g) > AgLi-CHI30 (907 μmol CO_2/g) > AgLi-CHI00 (501 μmol CO_2/g). This result indicated that the total basicity was not only the key parameter, which strongly affects on the oxidative dehydrogenation activity of the silver-lithium based catalysts. Evidently, this is consequence of an inductive effect of transition phase on alumina catalysts as being observed from the result that AgLi-CHI100 exhibits lower catalytic activity than AgLi-CHI00 in spite of its higher basicity. In addition, the electronic state of silver on the surface probably plays an important role for the specific forms of adsorbed oxygen that are selective for the different pathway of oxidation activity on silver. To compare the quality of the distinct silver species on the silver-lithium catalysts, the UV-Vis spectroscopy is the attractively useful technique for obtained well results. The UV-Vis spectra of the catalysts contain the similar band and appearance in peak around 210, 310 and 430 nm as seen in **Figure 4.13**. According to the previous literature data, the signals round 200-250 and 280-315 belong to charge transfer bands of Ag^+ and small charged $Ag_n^{\delta+}$ clusters (n<10) [77-79]. The presence of absorption band around 410-460 nm corresponds to the characteristic absorbance of metallic Ag^0 particles.

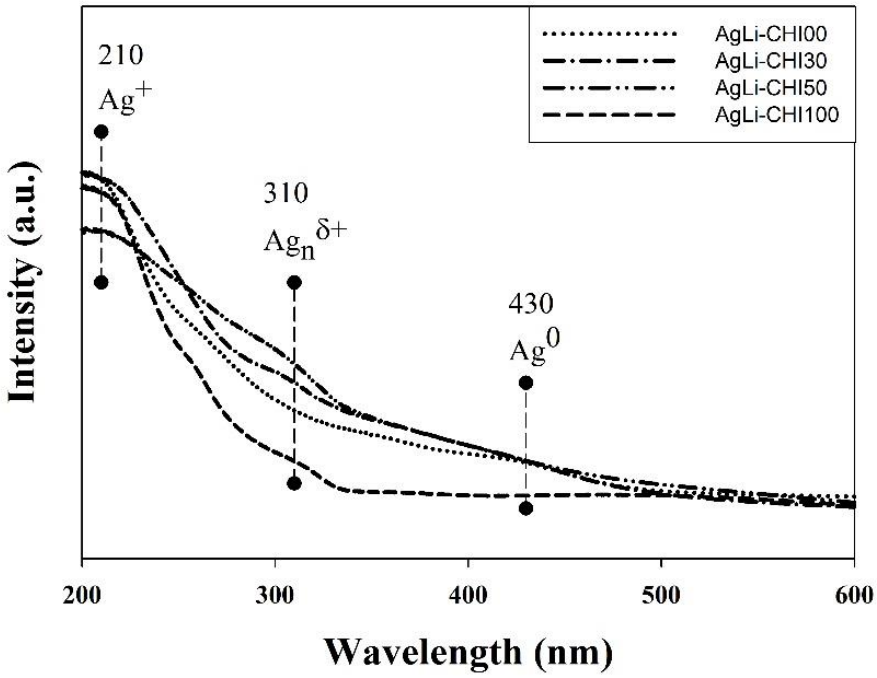

Figure 4.13 UV-Vis spectra of all prepared silver-lithium catalysts.

The spectra of AgLi-CHI00, AgLi-CHI30 and AgLi-CHI100 displayed the similarly high absorption intensity around 210 nm, which can be attributed to Ag^{+} while AgLi-CHI50 exhibited the lowest absorption intensity. Interestingly, AgLi-CHI00, AgLi-CHI30 and AgLi-CHI50 signals corresponding to charge $Ag_n^{\delta+}$ clusters are significantly more intensive as observed in the shoulder peak around 310 nm. This intensity decreased in the order: AgLi-CHI50 > AgLi-CHI30 > AgLi-CHI00 > AgLi-CHI100. This decreased in intensity corresponded to the decreased catalytic activity of silver-lithium catalysts. Previous studies indicated that the stabilizing effect of Ce and Zr oxides on ionic states of silver (Ag^{+}, $Ag_n^{\delta+}$) on the modified surface for selective oxidation of alcohol [80, 81]. Therefore, it can be observed from previous studies that oxygen-containing silver species is the active species for CO oxidation [73]. The facets of silver are ideal versatile facets to activate molecular oxygen and generate oxidative, strong basic oxygen species ($O^{\delta-}$) and weak acidic sites ($Ag_n^{\delta+}$). In addition, AgLi-CHI00, AgLi-CHI30 and AgLi-CHI50 exhibited significantly similar intensity as

observed in the shoulder peak around 310 nm corresponded to metallic Ag^0 particles while this absorbance disappears on AgLi-CHI100. The Ag^+ was assigned to be the active state for catalytic oxidation of ammonia at the temperature above 140 ^oC [82]. Previous studies suggested univalent $Ag_n^{\delta+}$ ions to be active states of silver for partial oxidation of alcohol [77, 80, 81]. Appropriately, the UV-vis spectra indicated that the small charged $Ag_n^{\delta+}$ clusters probably act as important state for oxidation reaction.

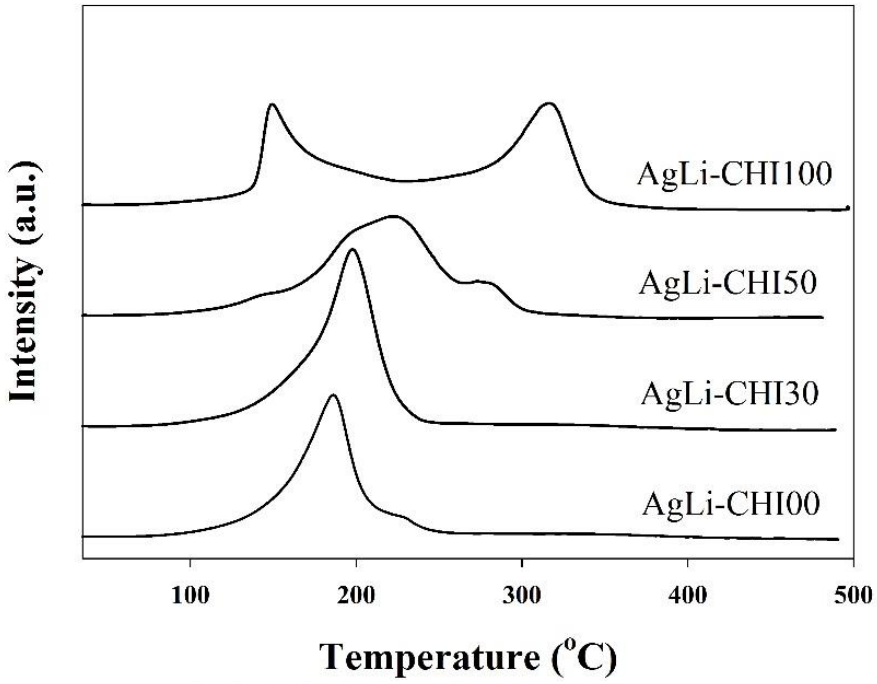

Figure 4.14 TPR profiles of all prepared silver-lithium catalysts.

Moreover, the reduction behaviors of all silver-lithium based catalysts were observed by temperature programmed reduction (TPR). The TPR profiles of silver-lithium supported on distinct alumina supports are shown in **Figure 4.14**. The reduction temperatures for all calcined silver-lithium catalysts located at ca. 100-400 ^oC. The reduction profile can be assigned to the overlap of two step reduction, which was observed for AgLi-CHI00, AgLi-CHI30 and AgLi-CHI50 catalysts. In the contrary, the two separate step of reduction peak was seen for AgLi-CHI100 catalyst. TPR profile for supported silver-lithium catalysts depended on various parameters such as the metal

particle size distribution, metal-support interaction and porous structure resulting in different reduction behavior for silver species on the support [83]. The reduction temperature for cobalt supported on χ-Al_2O_3 was higher than γ-Al_2O_3 [32]. This shift of reduction temperature indicated that the structure and morphology of the Al_2O_3 support apparently plays an important role for the reduction behavior of silver-lithium supported on Al_2O_3. Previous studies suggested that TPR profile displays the overlap of reduction peak from the molecular, the atomic and the lattice oxygen [84]. It clearly indicated that the low temperature peaks can be generally assigned to the reduction of the Ag_2O species, while the high temperature peaks resulted in further reduction of $Ag_n^{\delta+}$ clusters [74]. Moreover, the shift of $Ag_n^{\delta+}$ reduction peak toward to remarkably high temperature for AgLi-CHI100 corresponded to the lowest oxidative dehydrogenation activity as seen in TPR results. This evidence attractively shows that the reduction behavior of $Ag_n^{\delta+}$ predominantly plays an important role on oxidative dehydrogenation of ethanol. Interestingly, the shift of Ag^+ reduction peak toward to lower temperature decreased in the order: AgLi-CHI50 > AgLi-CHI30 > AgLi-CHI00 > AgLi-CHI100. This decreased reduction temperature corresponded to the decreased catalytic activity of silver-lithium catalysts. The maximum temperature results was corresponding with metal–support interaction. Probably, the stronger interaction between Ag_2O species and support was one key property.

From the obtained results, three primary products were obtained from reaction of ethanol. Acetaldehyde is mainly formed as major product by oxidative dehydrogenation of ethanol over all silver-lithium based catalysts at ca. 150 ^oC and total at 225 ^oC as seen the successive selectivity in **Figure 4.15a**. In the appearance of oxygen, the intrinsic catalytic dehydrogenation of ethanol is substantially high in gold catalysts [52]. The studies in surface science indicated that coadsorbed oxygen on transition metals acts as a Brønsted base promoting O-H bond cleavage [85]. Subsequent C-H bond cleavage leads to the formation of aldehyde and ketone. The continuous decrease of the acetaldehyde selectivity corresponded to the catalytic activity after the ethanol conversion achieved completely during the reaction above 225 ^oC. It can be observed that the acetaldehyde selectivity rapidly decreased with the high catalytic activity. The acetaldehyde selectivity increased in the order: AgLi-CHI50 <

AgLi-CHI00 < AgLi-CHI100 during the reaction temperature above 250 ^{o}C. At high reaction temperature, the formation of CO and CO_2 was favorable as seen in **Figure 4.15b** and **4.15c**. The catalytic process may occur via oxidation reaction pathways in series. The series pathway includes acetaldehyde as a prior product, which is subsequently oxidized to CO and followed by total oxidation towards to CO_2 as seen in **Scheme 4.3**.

a)

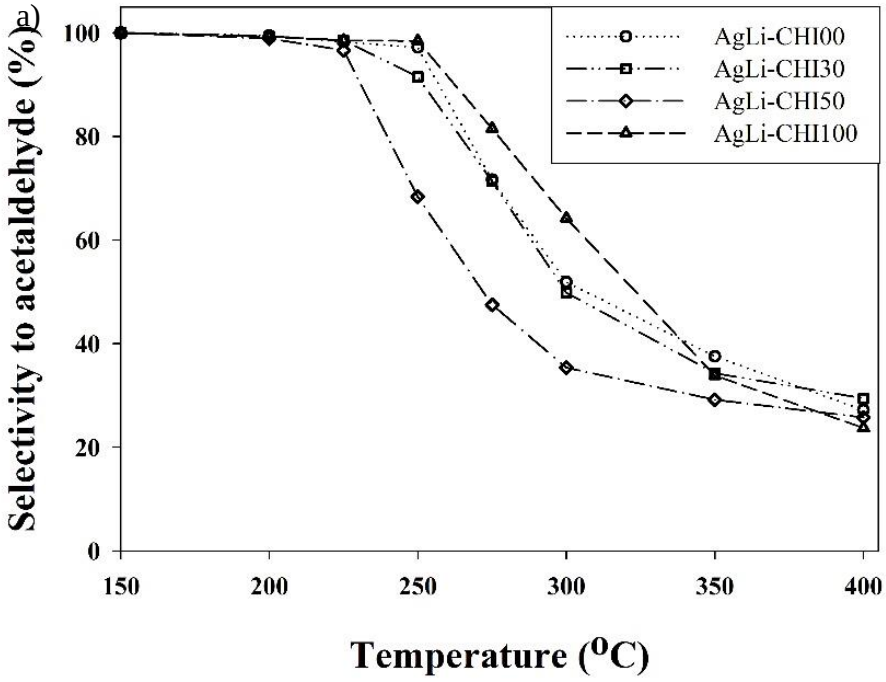

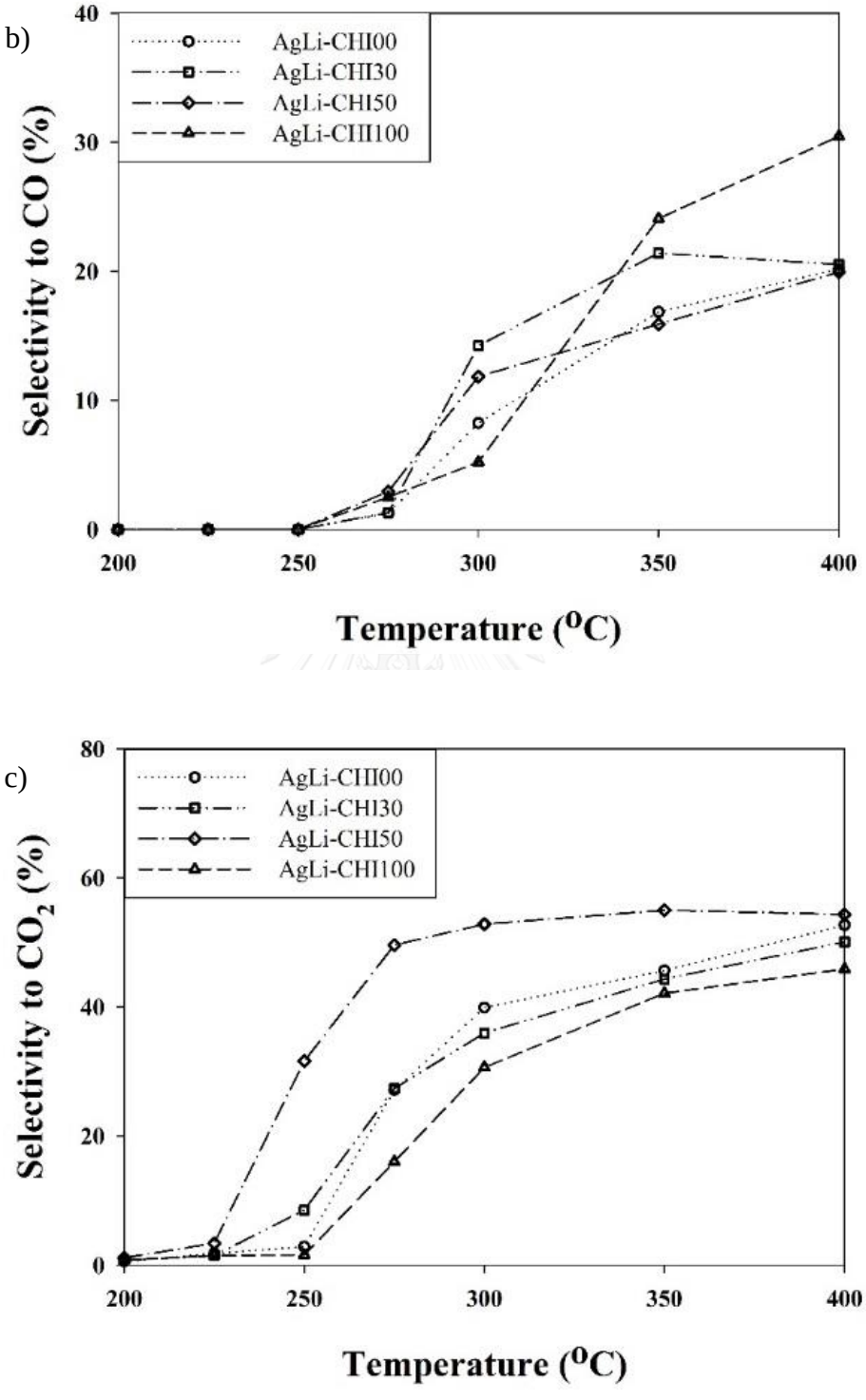

Figure 4.15 Selectivity to products of all prepared silver-lithium catalysts (a) acetaldehyde selectivity, (b) carbon monoxide selectivity, (c) carbon dioxide selectivity.

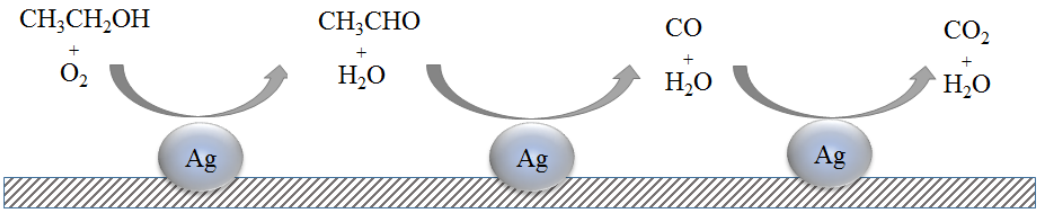

Scheme 4.3. The conceptual pathway for oxidative dehydrogenation of ethanol.

Interestingly, acetaldehyde molecule directly oxidized to form CO_2 during the reaction temperature between 225 to 250 ^{o}C as observed in the decreased acetaldehyde selectivity and CO_2 formation. This evidence confirmed the highest activity in oxidation reaction of AgLi-CHI50. Moreover, CO selectivity result indicated that AgLi-CHI100 exhibited the lowest oxidative activity leading to the CO accumulation at higher reaction temperature.

4.2.3 Surface structure sensitive on partially curved silver single crystal

The results from LEED and STM studies were summarized in **Figure 4.16**. The spot-splitting/row-spacing ratio as a function of azimuthal position from LEED patterns that were recorded while translating the crystal normal to the impacting electron beam as seen in **Figure 4.16a**. We simultaneously adjust the crystal's position to maintain a constant LEED-to-sample distance. **Figure 4.16b** shows representative LEED patterns. As explained by Henzler [86], diffraction from the stepped structure peaks at regularly spaced angles, $\Delta\varphi$, depending only on the terrace width (Na+g) and the step height (d) (see also **Figure 4.16b**):

$$\Delta\varphi = \lambda / [(Na+g)\cos\varphi - d\sin\varphi] \quad (1)$$

For the same number of terrace atoms, N, the spot-splitting/row-spacing ratio for the A type step (at negative angles) is slightly smaller than for the B type step (at positive angles). The difference is a consequence of the difference value of the horizontal offset

(g) between the exposed Ag lattice of successive terraces. The ratio has been calculated for a large number of stepped structures with integer N terrace atoms by van Hove and Somorjai, who also suggested the [N(terrace type)x(step type)] nomenclature [87]. When expressed in terms of angular position on a cylindrical crystal, their tabulated values (for structures that are exposed on our Ag crystal) are a linear function of azimuthal angle. In **Figure 4.16a** we plot this function (solid red lines) as described in our studies of a cylindrical Ni single crystal [88] together with two data sets of the experimentally determined ratio (solid and open symbols). The coincidence of the experimental data with predictions of the Henzler model indicates that our curved surface yields the expected average local step density at any position away from the (111) center. Furthermore, as explained in detail in ref. 10, one can also verify that steps are truly monoatomic by determining the electron energies at which the (0,0) beam shows singlets and doublets. We have performed this analysis at various azimuthal positions and find that the curvature of the crystal can only be explained by the large dominance of monoatomic steps. The same conclusion was drawn by Ortega and coworkers for their very similar curved Ag single crystal [89].

Our STM data, taken later in the UHV-STM apparatus, corroborate these findings. Typical images of ~50×50 nm^2 are shown in **Figure 4.16c**. The middle image shows a large and flat (111) area found near the middle of the crystal. The other images show large areas dominated by monoatomic steps. Some protrusions appearing as white and black spots have been determined to cover < 2% of the surface area. They have an apparent height on the order of 1 nm and remain unidentified as we detect no elements other than Ag in AES spectra. These protrusions could not be removed by extensive sputtering-annealing or oxidation-reduction cycles, which suggests that they are remnants of the polishing process.

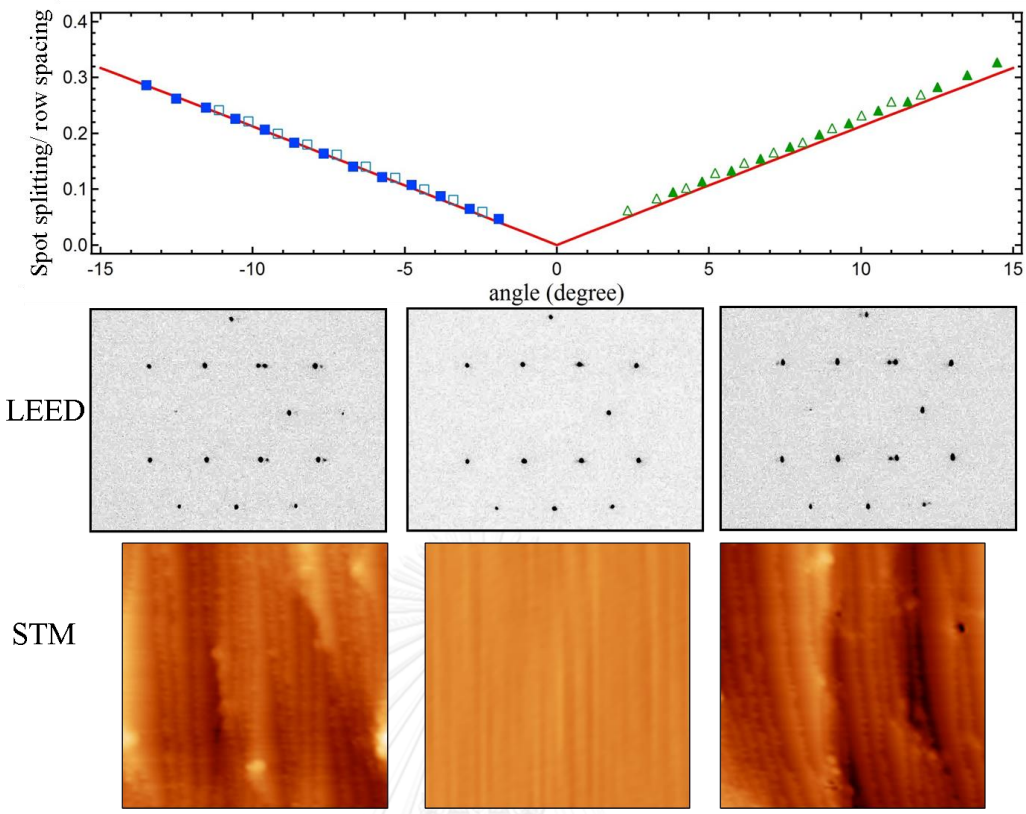

Figure 4.16 a) spot splitting-to-row spacing ratio as a function of angle; red circles and black squares are used for two data sets collected on different days, red solid lines indicate expect values b) images of color-inverted LEED patterns taken at -1.5 mm (left), 0.00 mm (middle), and +1.5 mm (right) from the crystal center c) STM images (100 x 100 nm^2) taken at -1.6 mm (left), 0.00 mm (middle), and +1.6 mm (right) from the crystal center

Thermal desorption spectra for 0.06-0.08 ML H_2O are shown in **Figure 4.17** for (111) (bottom traces both left and right) and various average terrace widths separated by A (left) and B (right) type steps. A small shift in the peak desorption temperature as a function of step density is apparent when comparing TPD traces for each type of step. To facilitate comparison, the temperature of maximum flux from Ag (111) is indicated. We fit each desorption profile using a single Gaussian function and determine the peak's amplitude (A), width (α), and peak desorption temperature (T_p). The fits are shown in **Figure 4.17** as solid traces through the data.

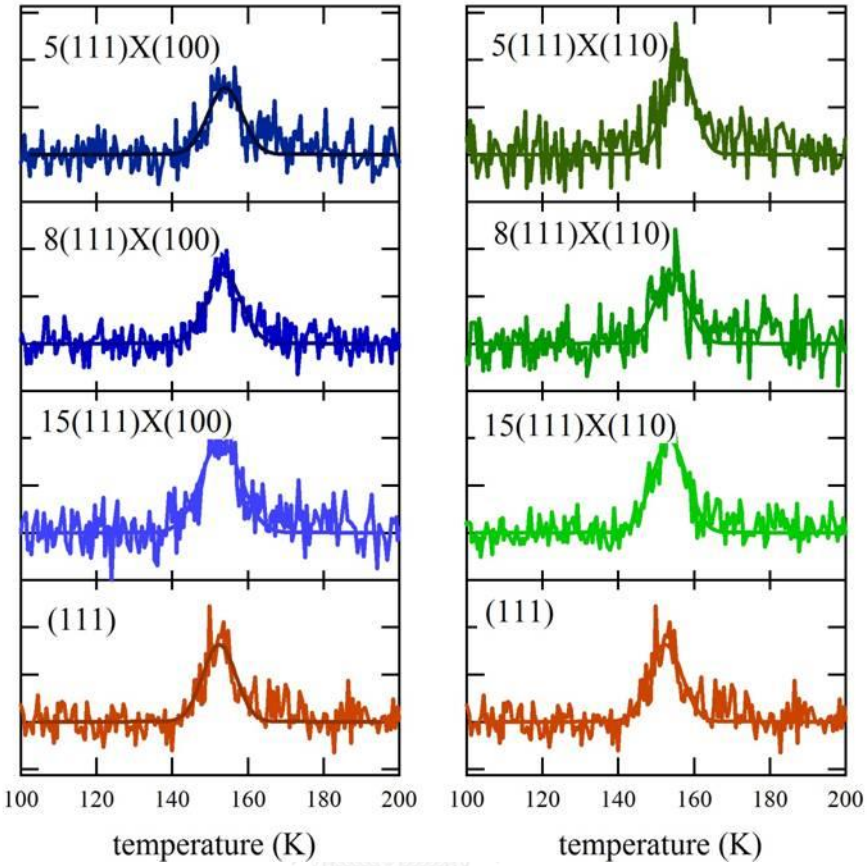

Figure 4.17 Series of spatially-resolved TPD spectra for 0.06-0.08 ML exposures to H_2O for the (left) A step type [N(111)x(100)] and (right) B step type [N(111)x(110)]. Solid lines are fits to the data using Gaussian functions.

The values of the three fitting parameters are plotted versus step density in **Figure 4.18**. We including the error as determined by the fitting procedure and show these as error bars. The desorption amplitude (A) and width (α) are nearly constant. No clear trend with step density is observed. The peak desorption temperature (T_p), however, depends significantly on step density over the entire range for both A and B. Translating the crystal over +/- 3 mm results in a shift of ~1.5 K for the A step type and ~3.5 K for the B step type. Over this range, the central surface structure from which desorption is probed changes from approximately [6(111)×(100)] to [6(111)×(110)]. The temperature shift appears to be proportional to step density. Linear fits are shown as dashed lines. These individual fits suggest that T_p for the 'infinite' (111) plane is

152.2 ± 0.1 K and 152.1 ± 0.2 K, as determined from the A and B steps respectively. The slopes are 19.7±1.8 K·Å and 42.4±4.4 K·Å. Considering the uncertainty of the best-fit parameters and the negligible temperature gradient across the crystal as determined from **Figure 4.18**, we conclude that the A and B type steps influence water desorption in an experimentally measurable and different manner. The B step type induces a peak temperature shift approximately twice as large as the A step type.

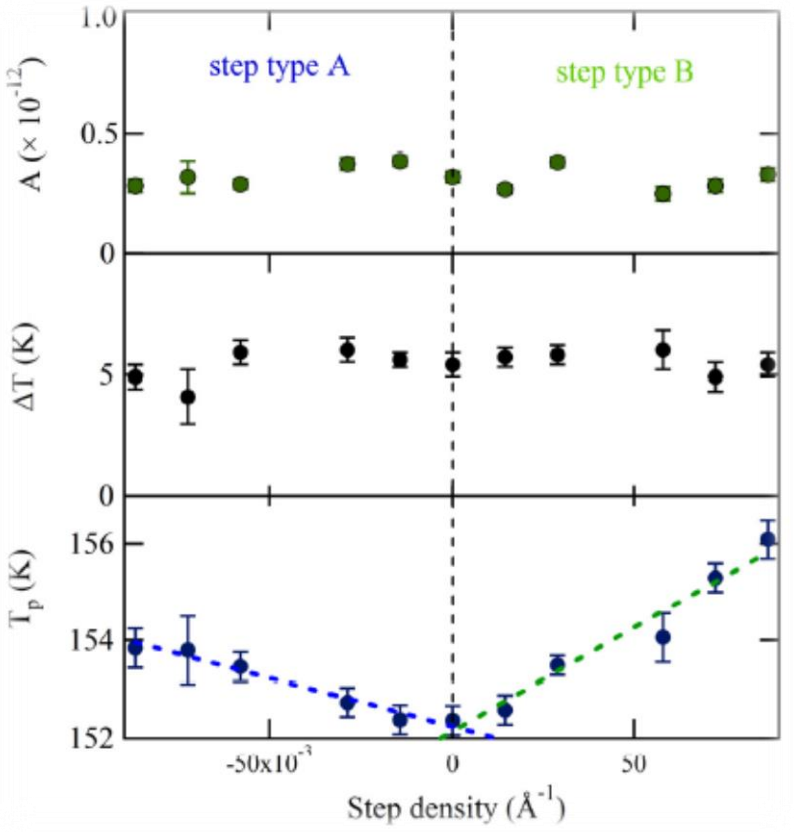

Figure 4.18 Amplitude (A), peak width (ΔT) and peak temperature (T_p) determined from fitting spatially-resolved TPD spectra with Gaussian functions

The results presented here are noteworthy for two reasons. First, the peak temperature shift is small but significant. To our knowledge, this is the first time that a characteristic change in TPD features of this magnitude has been attributed to surface structure. The difference is so small that it would be difficult to determine using multiple flat single crystals. At least 2 or 3 samples with widely varying step densities of both step types and an Ag(111) surface would be required to establish this trend.

Even then, random sample-to-sample temperature measurement error (caused by irreproducible mounting of samples and thermocouples) is likely to dominate the intrinsically lower random error of a single sample measured multiple times, as here. Second, considering the shape and near invariance in peak width, it is not immediately obvious how a linear dependence of a peak desorption temperature on step density for adsorbates in the submonolayer regime is to be interpreted. To our knowledge, such a phenomenon has also not been reported before.

To guide our consideration of possible origins for the observed desorption temperature dependence, we first summarize the results of previous publications on the adsorption of water to Ag(111) and related surfaces. The first report of water desorption from Ag(111) by Klaua and Madey[90] shows a single peak with a desorption maximum shifting from 175 K to higher temperatures with increased dosing. In line with zeroth-order desorption kinetics, the leading edges overlap of all traces overlap. Close inspection of their TPD data shows the onset of desorption at ~141 K. This is in excellent agreement with our results for Ag(111) for very low water coverages, as shown in **Figure 4.1**7. The same analysis for their desorption data from Ag(100) suggests an onset near 145 K. The first desorption data from Ag(110) by Stuve, Madix and Sexton[91] unfortunately shows a non-flat baseline prior to the desorption, hence this data does not allow us to extract the onset temperature. In a later publication, the onset appears ~140 K for 0.06 ML of water[92]. None of these surfaces showed any evidence for long-range ordering of water molecules by LEED or ESDIAD. The desorption features were interpreted to indicate either dissolving of water clusters in the submonolayer regime and/or sublimation from three-dimensional crystallites. For all these substrates, the intermolecular forces were apparently greater than the interaction of water with the Ag substrate. Multilayered features simply form as a consequence of an increased chance for water molecules to impinge onto two-dimensional ice clusters with increasing exposure and the absence of a dominant driving force to bind to the substrate.

In a more recent series of experiments that imaged water on Ag(111) using low temperature STM in the submonolayer regime, Morgenstern and coworkers found single protrusions for water dosed at 70 K[93, 94]. These protrusions were interpreted

as cyclic water hexamers. Larger stable clusters containing heptamers, octamers and nonamers are also observed when water is dosed at 17 K[95]. The hexamers are buckled, with alternating H-bond lengths as a consequence of a competition between H_2O's simultaneous tendency to bond with the substrate and act as a hydrogen bond acceptor. At the higher dosing temperature, hexamers mostly conglomerate in large water-covered patches without long-range order [93, 94]. An oscillatory distance distribution between water hexamers is caused by electronic surface states[96]. Interestingly, water clusters of different apparent heights were also found along the upper edge of descending step edges even for otherwise uncovered terraces[93, 94]. The height variation suggests a variation in cluster size and/or form and a high barrier for reorientation after water molecules adsorb to the step edge. The absence of order between these protrusions at the step edge indicates a lack of a strong driving force for long-range ordering. For Pt(111) [97], similar behavior was observed.

Preferential adsorption to step edges is generally attributed to the Smoluchowski effect[98]: a smoothing of the electronic cloud at a sharp edge lowers electron density at the upper edge. This electronic redistribution was originally inferred from a dependence of the work function of metals on surface structure. However, scanning tunneling spectroscopy (STS) measurements by Avouris et al. visualized that the local density of states (LDOS) at step edges of Au(111) and Ag(111)[99]. On the upper side, the density of unoccupied states increased at the expense of such states at the lower part of the edge. The associated dipole oriented parallel to the surface was predicted to strongly affect adsorption of molecules. Recently, different types of steps on an Ag(111) surface were also shown by STS to affect the local electronic structure in markedly different ways indicating that all steps are not equal[100].

Water's electron donating capacity may result in stronger binding to the upper edge. The STM results for water clusters bound to step edges on Ag(111)[93, 94] and Pt(111)[97] confirm that steps are the preferred adsorption sites. It also shows that diffusion is fast at the dosing temperature and occurs over distances at least comparable to the terrace widths generally observed for a (111) plane on the time scale of the measurements. A computational study by Scipioni et al. finds that the adsorption energy for the water monomer to the B step type is 0.20 eV[101]. This is indeed slightly higher

that the 0.18 eV found for the atop site on Ag(111)[102, 103]. A comparative study of single water molecules binding to the A and B step type of Pt(111), did not find an explanation for the experimental result[104]. A small shift to higher desorption temperatures in TPD spectra would reflect such a minor difference in binding energy for steps and terraces. Thus it seems logical that the different dependence of our TPD spectra on step density for A and B step types reflects different binding geometries and desorption energies of H_2O to these different steps.

We suggest a simple ‘two-state model’ to explain our results. One part of the water dosed onto a local structure finds itself adsorbed as part of cyclic hexagons at (111) terrace sites whereas the remainder is trapped at a step with a higher binding energy. Both states desorb with a desorption energy that is nearly invariant with the state’s coverage. It is governed by the dissolution energy of the local structure at terrace and step. Thus, both states should show zeroth-order desorption kinetics and show peaks that are offset on the temperature axis as consequence of their different dissolution energies. The relative amplitudes are governed only by the coverage and step density.

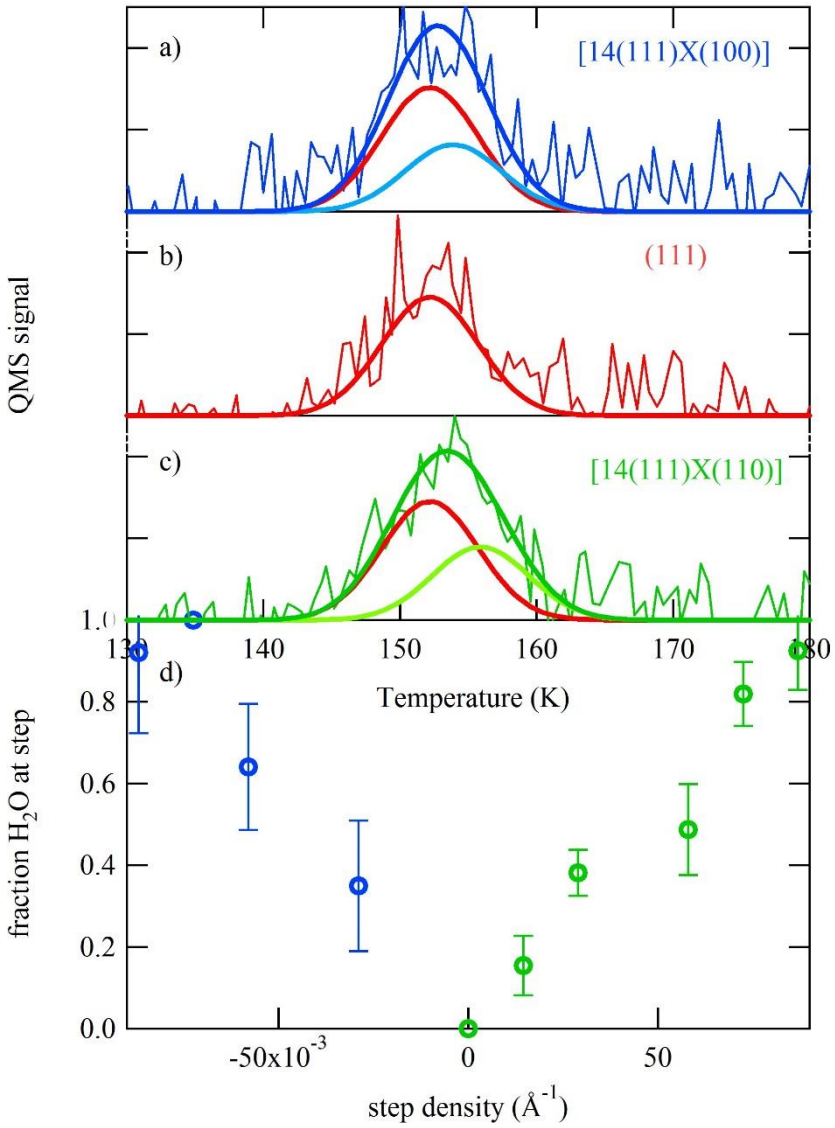

Figure 4.19 a-c) Deconvolution of TPD features from three different surface structures into contributions from (111)-bound hexamers and water clusters bound to A (blue) and B (green) type step edges. d) Fractional contribution of steps to the total observed desorption as obtained for a two state model.

We may attempt to fit our data by such a 'two-state' model. To simplify matters and to incorporate non-idealities, e.g. limited pumping speed and a tail generally observed in TPD spectra for H_2O, we use Gaussian functions instead of the zeroth-order desorption peak shape. Values for T_p are extracted from **Figure 4.18**. For a lack of steps at the central (111) part of our curved crystal, most of the 0.06-0.08 ML H_2O should be condensed as water hexagons and we use 152.2 K for their desorption temperature. To

determine T_p for the A and B step types we take into consideration that a water hexagon spans three atomic rows. We estimate that for a 4-atom wide terrace, these hexagons can not exist without direct interaction with the atoms forming the step edge due to the driving force to anchor at the step edge. Thus, we use the step density of the [4(111)x(100)] and [4(111)x(110)] planes and the linear fits in **Figure 4.18** to estimate T_p for desorption from the A and B step types. These are 153.9 K and 155.9 K, respectively. Note that these values would hardly change if we would choose any other value close to 4. For both terrace and step desorption peaks we assume a Gaussian width (α) of 5.0 K as **Figure 4.18** suggests this to be a rather accurate value for both extremes. We now fit a double Gaussian function with T_p values for terrace and step and extract the relative amplitudes of the two contributions for all of our data. The individual contributions to desorption of the hexagons (red) and step (green and blue) as well as the total desorption intensity are shown in **Figure 4.19a-c**) for three surface structures. The fractional contribution of the step to the total desorption intensity in this two-state desorption model is shown in **Figure 4.19d**. The linearity of the step contribution on either side of (111) indicates that the model is self-consistent and our data well.

CHAPTER V
CONCLUSIONS AND RECOMMENDATIONS

5.1 Conclusions

In summary, the combination of nanocrystalline γ- and χ-alumina can be attractively used for catalytic dehydration of ethanol with distinct chemical and physical properties from native γ- and χ- alumina. The correlation between ethanol conversion and acid density of the catalysts suggested that the possible pathway includes diethyl ether as a reaction intermediate, which is continually decomposed to ethylene at low temperature. The relationship between ethylene selectivity and H_2O on surface as observed from XPS analysis is crucial. The consequence of an inductive effect of transition phase and crystallographic orientation on alumina displays the distinct activity of acid site. The appearance of metastable χ-alumina structure based on hexagonal close packing (hcp) exhibits better catalytic conversion and ethylene selectivity than γ-alumina based on cubic close packing (ccp) in spite of its lower acidity. This should be due to the increase in acid density with introduction of χ-alumina.

In the second part, the influences of Ag/Li modification on mixed-phase alumina can be attractively used for oxidative dehydrogenation of ethanol to acetaldehyde. The high catalytic activity and acetaldehyde selectivity corresponded to the oxidation state and reduction behavior as observed by UV-Vis and TPR. The relationship between catalytic activity and $Ag_n^{\delta+}$ clusters on surface as observed from UV-Vis analysis is crucial. Moreover, the remarkably high temperature of $Ag_n^{\delta+}$ reduction peak corresponded to the low oxidative dehydrogenation activity as seen in TPR results. In addition, the water desorption from a curved single crystal surface was investigated. A shift in desorption temperature for very small coverages exhibits originates from small differences in the dissolution and consecutive desorption energies of water clusters bound to the (111) terrace and the upper edge of steps. The stronger shift for the B step type indicates a stronger binding to this (110) edge.

5.2 Recommendations

1. In the further study, the pyridine FT-IR should be used to investigate the types of acid sites included Bronsted acid site and Lewis acid site for alumina catalysts. The obtained results should be used to confirm the amount of Brønsted acid site as observed by XPS analysis which was an important factor for the selectivity to ethylene.

2. The oxidation behavior of AgLi-alumina catalysts should be further investigated via Temperature programmed oxidation. The obtained results should be used to explain the behavior and amount of oxygen which can adsorb on silver surface. This should be an important data to conclude the oxidative dehydrogenation activities.

3. The thermal stability, life span and coke accumulation of the alumina and AgLi-alumina catalysts should be further investigated. The obtained results should be used to evaluate the catalysts deactivation and coke formation.

REFERENCES

[1] Bedia, J., Barrionuevo, R., Rodríguez-Mirasol, J., and Cordero, T. Ethanol dehydration to ethylene on acid carbon catalysts. Applied Catalysis B: Environmental 103(3–4) (2011): 302-310.

[2] Takahara, I., Saito, M., Inaba, M., and Murata, K. Dehydration of Ethanol into Ethylene over Solid Acid Catalysts. Catalysis Letters 105(3-4) (2005): 249-252.

[3] Martins, L., Cardoso, D., Hammer, P., Garetto, T., Pulcinelli, S.H., and Santilli, C.V. Efficiency of ethanol conversion induced by controlled modification of pore structure and acidic properties of alumina catalysts. Applied Catalysis A: General 398(1-2) (2011): 59-65.

[4] Phung, T.K., et al. Surface and catalytic properties of some γ-Al2O3 powders. Applied Catalysis A: General 483(0) (2014): 41-51.

[5] Zotov, R.A., Molchanov, V.V., Volodin, A.M., and Bedilo, A.F. Characterization of the active sites on the surface of Al2O3 ethanol dehydration catalysts by EPR using spin probes. Journal of Catalysis 278(1) (2011): 71-77.

[6] Chiang, H. and Bhan, A. Catalytic consequences of hydroxyl group location on the rate and mechanism of parallel dehydration reactions of ethanol over acidic zeolites. Journal of Catalysis 271(2) (2010): 251-261.

[7] Madeira, F.F., Gnep, N.S., Magnoux, P., Maury, S., and Cadran, N. Ethanol transformation over HFAU, HBEA and HMFI zeolites presenting similar Brønsted acidity. Applied Catalysis A: General 367(1–2) (2009): 39-46.

[8] Varisli, D., Dogu, T., and Dogu, G. Ethylene and diethyl-ether production by dehydration reaction of ethanol over different heteropolyacid catalysts. Chemical Engineering Science 62(18–20) (2007): 5349-5352.

[9] Riad, M., Sobhi, Z., and Mikhail, S. Catalytic dehydration reaction of ethanol over transition metal catalysts. Journal of Engineering and Applied Science 49(1) (2002): 195-208.

[10] Zaki, T. Catalytic dehydration of ethanol using transition metal oxide catalysts. Journal of Colloid and Interface Science 284(2) (2005): 606-613.

[11] Gao, X. and Wachs, I.E. Titania–silica as catalysts: molecular structural characteristics and physico-chemical properties. Catalysis Today 51(2) (1999): 233-254.

[12] Hashimoto, K. and Toukai, N. Dehydrogenation of alcohols over potassium zinc aluminum silicate hydroxide. Journal of Molecular Catalysis A: Chemical 145(1–2) (1999): 273-280.

[13] Mistry, C.R., Mewada, R.K., Srivastava, V.K., and Jasra, R.V. Characteristics of Oxidation and Oxidative Dehydrogenation Catalysts for Gas Phase Reactions : A Review. in *INTERNATIONAL CONFERENCE ON CURRENT TRENDS IN TECHNOLOGY*. 2011: Institute of technology, Nirma University, Ahmedabad. 1-6.

[14] Santacesaria, E., Sorrentino, A., Tesser, R., Di Serio, M., and Ruggiero, A. Oxidative dehydrogenation of ethanol to acetaldehyde on V2O5/TiO2-SiO2 catalysts obtained by grafting vanadium and titanium alkoxides on silica. Journal of Molecular Catalysis A: Chemical 204–205(0) (2003): 617-627.

[15] Weinstein, R.D., Ferens, A.R., Orange, R.J., and Lemaire, P. Oxidative dehydrogenation of ethanol to acetaldehyde and ethyl acetate by graphite nanofibers. Carbon 49(2) (2011): 701-707.
[16] Lippits, M.J. and Nieuwenhuys, B.E. Direct conversion of ethanol into ethylene oxide on copper and silver nanoparticles. Catalysis Today 154(1-2) (2010): 127-132.
[17] Lippits, M.J. and Nieuwenhuys, B.E. Direct conversion of ethanol into ethylene oxide on gold-based catalystsEffect of CeOx and Li2O addition on the selectivity. Journal of Catalysis 274(2) (2010): 142-149.
[18] Bi, J., Guo, X., Liu, M., and Wang, X. High effective dehydration of bio-ethanol into ethylene over nanoscale HZSM-5 zeolite catalysts. Catalysis Today 149(1–2) (2010): 143-147.
[19] Vít, Z., Vala, J., and Málek, J. Acid-base properties of aluminium oxide. Applied Catalysis 7(2) (1983): 159-168.
[20] Mekasuwandumrong, O., Silveston, P.L., Praserthdam, P., Inoue, M., Pavarajarn, V., and Tanakulrungsank, W. Synthesis of thermally stable micro spherical χ-alumina by thermal decomposition of aluminum isopropoxide in mineral oil. Inorganic Chemistry Communications 6(7) (2003): 930-934.
[21] Pansanga, K., Panpranot, J., Mekasuwandumrong, O., Satayaprasert, C., Goodwin, J.G., and Praserthdam, P. Effect of mixed γ- and χ-crystalline phases in nanocrystalline Al2O3 on the dispersion of cobalt on Al2O3. Catalysis Communications 9(2) (2008): 207-212.
[22] Meephoka, C., Chaisuk, C., Samparnpiboon, P., and Praserthdam, P. Effect of phase composition between nano γ- and χ-Al2O3 on Pt/Al2O3 catalyst in CO oxidation. Catalysis Communications 9(4) (2008): 546-550.
[23] Keshavarz, A.R., Rezaei, M., and Yaripour, F. Nanocrystalline gamma-alumina: A highly active catalyst for dimethyl ether synthesis. Powder Technology 199(2) (2010): 176-179.
[24] Hosseini, Z., Taghizadeh, M., and Yaripour, F. Synthesis of nanocrystalline γ-Al2O3 by sol-gel and precipitation methods for methanol dehydration to dimethyl ether. Journal of Natural Gas Chemistry 20(2) (2011): 128-134.
[25] Liu, C., Liu, Y., Ma, Q., and He, H. Mesoporous transition alumina with uniform pore structure synthesized by alumisol spray pyrolysis. Chemical Engineering Journal 163(1–2) (2010): 133-142.
[26] Inoue, M., Kominami, H., and Inui, T. Thermal reaction of aluminum alkoxide in glycols. Journal of the American Ceramic Society 73(4) (1990): 1100-1102.
[27] Inoue, M., Kominami, H., and Inui, T. Reaction of aluminium alkoxides with various glycols and the layer structure of their products. Journal of the Chemical Society, Dalton Transactions (12) (1991): 3331-3336.
[28] Inoue, M., Kominami, H., and Inui, T. Thermal Transformation of X-Alumina Formed by Thermal Decomposition of Aluminum Alkoxide in Organic Media. Journal of the American Ceramic Society 75(9) (1992): 2597-2598.
[29] Inoue, M., Kominami, H., and Inui, T. Novel synthetic method for the catalytic use of thermally stable zirconia: thermal decomposition of zirconium alkoxides in organic media. Applied Catalysis A: General 97(2) (1993): L25-L30.

[30] Inoue, M., Kondo, Y., and Inui, T. An ethylene glycol derivative of boehmite. Inorganic Chemistry 27(2) (1988): 215-221.
[31] Khom-in, J., Praserthdam, P., Panpranot, J., and Mekasuwandumrong, O. Dehydration of methanol to dimethyl ether over nanocrystalline Al2O3 with mixed γ- and χ-crystalline phases. Catalysis Communications 9(10) (2008): 1955-1958.
[32] Chaitree, W., Jiemsirilers, S., Mekasuwandumrong, O., Jongsomjit, B., Shotipruk, A., and Panpranot, J. Effect of nanocrystalline χ-Al2O3 structure on the catalytic behavior of Co/Al2O3 in CO hydrogenation. Catalysis Today 164(1) (2011): 302-307.
[33] Glinrun, T., Mekasuwandumrong, O., Panpranot, J., Chaisuk, C., and Praserthdam, P. Improvement of propane oxidation activity over Pt/Al2O3 by the use of MIXED γ- and χ-Al2O3 supports. Reaction Kinetics, Mechanisms and Catalysis 100 (2010): 441-448.
[34] Shinohara, Y., Nakajima, T., and Suzuki, S. A theoretical study of the dehydration and the dehydrogenation processes of alcohols on metal oxides using MOPAC. Journal of Molecular Structure: THEOCHEM 460(1–3) (1999): 231-244.
[35] Iwasawa, Y. Surface Catalytic Reactions Assisted by Gas Phase Molecules. Accounts of Chemical Research 30(3) (1997): 103-109.
[36] Allison, J.N. and Goddard Iii, W.A. Oxidative dehydrogenation of methanol to formaldehyde. Journal of Catalysis 92(1) (1985): 127-135.
[37] Santos, P.S., Santos, H.S., and Toledo, S.P. Standard transition aluminas. Electron microscopy studies. Materials Research 3 (2000): 104-114.
[38] Jiao, W.Q., Yue, M.B., Wang, Y.M., and He, M.-Y. Synthesis of morphology-controlled mesoporous transition aluminas derived from the decomposition of alumina hydrates. Microporous and Mesoporous Materials 147(1) (2012): 167-177.
[39] Chang, P.-L., Wu, Y.-C., Lai, S.-J., and Yen, F.-S. Size effects on χ- to α-Al2O3 phase transformation. Journal of the European Ceramic Society 29(16) (2009): 3341-3348.
[40] Wittayakhun, J. and Krisadanurak, N. (eds.). Catalysis: Fundamentals and Application. 1 ed. Thammasart university publishing: Thammasart university 2004.
[41] Cheng, L.-T., Tsai, M.-Y., Tseng, W.J., Hsiang, H.-I., and Yen, F.-S. Boehmite coating on θ-Al2O3 particles via a sol–gel route. Ceramics International 34(2) (2008): 337-343.
[42] Li, J., Pan, Y., Xiang, C., Ge, Q., and Guo, J. Low temperature synthesis of ultrafine α-Al2O3 powder by a simple aqueous sol–gel process. Ceramics International 32(5) (2006): 587-591.
[43] Ouyang, J., Kong, F., Su, G., Hu, Y., and Song, Q. Catalytic Conversion of Bio-ethanol to Ethylene over La-Modified HZSM-5 Catalysts in a Bioreactor. Catalysis Letters 132(1-2) (2009): 64-74.
[44] Hu, Y., et al. Selective dehydration of bio-ethanol to ethylene catalyzed by lanthanum-phosphorous-modified HZSM-5: Influence of the fusel. Biotechnology Journal 5(11) (2010): 1186-1191.

[45] Ramesh, K., Jie, C., Han, Y.-F., and Borgna, A. Synthesis, Characterization, and Catalytic Activity of Phosphorus Modified H-ZSM-5 Catalysts in Selective Ethanol Dehydration. Industrial & Engineering Chemistry Research 49(9) (2010): 4080-4090.

[46] Chen, G., Li, S., Jiao, F., and Yuan, Q. Catalytic dehydration of bioethanol to ethylene over TiO2/γ-Al2O3 catalysts in microchannel reactors. Catalysis Today 125(1–2) (2007): 111-119.

[47] Xiao, Y., Li, X., Yuan, Z., Li, J., and Chen, Y. Catalytic Dehydration of Ethanol to Ethylene on TiO2/4A Zeolite Composite Catalysts. Catalysis Letters 130(3-4) (2009): 308-311.

[48] Wu, L.-P., Li, X.-J., Yuan, Z.-H., and Chen, Y. The fabrication of TiO2-supported zeolite with core/shell heterostructure for ethanol dehydration to ethylene. Catalysis Communications 11(1) (2009): 67-70.

[49] Zhan, N., Hu, Y., Li, H., Yu, D., Han, Y., and Huang, H. Lanthanum–phosphorous modified HZSM-5 catalysts in dehydration of ethanol to ethylene: A comparative analysis. Catalysis Communications 11(7) (2010): 633-637.

[50] Bokade, V.V. and Yadav, G.D. Heteropolyacid supported on montmorillonite catalyst for dehydration of dilute bio-ethanol. Applied Clay Science 53(2) (2011): 263-271.

[51] Yang, Z., Li, J., Yang, X., Xie, X., and Wu, Y. Gas-phase oxidation of alcohols over silver: The extension of catalytic cycles of oxidation of alcohols in liquid-phase. Journal of Molecular Catalysis A: Chemical 241(1–2) (2005): 15-22.

[52] Guan, Y. and Hensen, E.J.M. Ethanol dehydrogenation by gold catalysts: The effect of the gold particle size and the presence of oxygen. Applied Catalysis A: General 361(1–2) (2009): 49-56.

[53] Gurgul, J., Zimowska, M., Mucha, D., Socha, R.P., and Matachowski, L. The influence of surface composition of Ag3PW12O40 and Ag3PMo12O40 salts on their catalytic activity in dehydration of ethanol. Journal of Molecular Catalysis A: Chemical 351(0) (2011): 1-10.

[54] Sander, M., Imbihl, R., and Ertl, G. Kinetic oscillations in catalytic CO oxidation on a cylindrical Pt single crystal surface. The Journal of Chemical Physics 97(7) (1992): 5193-5204.

[55] Corso, M., Schiller, F., Fernandez, L., Cordon, J., and Ortega, J.E. Electronic states in faceted Au(111) studied with curved crystal surfaces. J Phys Condens Matter. 21(35) (2009): 353001. doi: 10.1088/0953-8984/21/35/353001. Epub 2009 Jul 20.

[56] Mom, R.V., Hahn, C., Jacobse, L., and Juurlink, L.B.F. LEED analysis of a nickel cylindrical single crystal. Surface Science 613(0) (2013): 15-20.

[57] Martins, L., Cardoso, D., Hammer, P., Garetto, T., Pulcinelli, S.H., and Santilli, C.V. Efficiency of ethanol conversion induced by controlled modification of pore structure and acidic properties of alumina catalysts. Applied Catalysis A: General 398(1–2) (2011): 59-65.

[58] Ausavasukhi, A. and Sooknoi, T. Additional Brønsted acid sites in [Ga]HZSM-5 formed by the presence of water. Applied Catalysis A: General 361(1-2) (2009): 93-98.

[59] Mostafa, M.R., Youssef, A.M., and Hassan, S.M. Conversion of ethanol and isopropanol on alumina, titania and alumina-titania catalysts. Materials Letters 12(3) (1991): 207-213.
[60] Golay, S., Kiwi-Minsker, L., Doepper, R., and Renken, A. Influence of the catalyst acid/base properties on the catalytic ethanol dehydration under steady state and dynamic conditions. In situ surface and gas-phase analysis. Chemical Engineering Science 54(15–16) (1999): 3593-3598.
[61] Christiansen, M.A., Mpourmpakis, G., and Vlachos, D.G. Density Functional Theory-Computed Mechanisms of Ethylene and Diethyl Ether Formation from Ethanol on γ-Al2O3(100). ACS Catalysis 3(9) (2013): 1965-1975.
[62] Nguyen, T.M. and Le Van Mao, R. Conversion of ethanol in aqueous solution over ZSM-5 zeolites: Study of the reaction network. Applied Catalysis 58(1) (1990): 119-129.
[63] Phung, T.K., Lagazzo, A., Rivero Crespo, M.Á., Sánchez Escribano, V., and Busca, G. A study of commercial transition aluminas and of their catalytic activity in the dehydration of ethanol. Journal of Catalysis 311 (2014): 102-113.
[64] Kloprogge, J.T., Duong, L.V., Wood, B.J., and Frost, R.L. XPS study of the major minerals in bauxite: gibbsite, bayerite and (pseudo-)boehmite. J Colloid Interface Sci 296(2) (2006): 572-6.
[65] Sheng, Q., Ling, K., Li, Z., and Zhao, L. Effect of steam treatment on catalytic performance of HZSM-5 catalyst for ethanol dehydration to ethylene. Fuel Processing Technology 110 (2013): 73-78.
[66] Jingfa, D., Guirong, Z., Shuzhong, D., Haishui, P., and Huaiming, W. Acidic properties of ZSM-5 zeolite and conversion of ethanol to diethyl ether. Applied Catalysis 41(0) (1988): 13-22.
[67] Ciftci, A., Varisli, D., Cem Tokay, K., Aslı Sezgi, N., and Dogu, T. Dimethyl ether, diethyl ether & ethylene from alcohols over tungstophosphoric acid based mesoporous catalysts. Chemical Engineering Journal 207–208(0) (2012): 85-93.
[68] Roca, F.F., De Mourgues, L., and Trambouze, Y. Catalytic dehydration of ethanol over silica-alumina. Journal of Catalysis 14(2) (1969): 107-113.
[69] Matachowski, L., Zimowska, M., Mucha, D., and Machej, T. Ecofriendly production of ethylene by dehydration of ethanol over Ag3PW12O40 salt in nitrogen and air atmospheres. Applied Catalysis B: Environmental 123-124 (2012): 448-456.
[70] Le Van Mao, R., Nguyen, T.M., and Yao, J. Conversion of ethanol in aqueous solution over ZSM-5 zeolites: Influence of Reaction Parameters and Catalyst Acidic Properties as Studied by Ammonia TPD Technique. Applied Catalysis 61(1) (1990): 161-173.
[71] Rahmanian, A. and Ghaziaskar, H.S. Continuous dehydration of ethanol to diethyl ether over aluminum phosphate–hydroxyapatite catalyst under sub and supercritical condition. The Journal of Supercritical Fluids 78(0) (2013): 34-41.
[72] Badlani, M. and Wachs, I. Methanol: A “Smart” Chemical Probe Molecule. Catalysis Letters 75(3-4) (2001): 137-149.

[73] Zhang, X., et al. Studies of silver species for low-temperature CO oxidation on Ag/SiO2 catalysts. Separation and Purification Technology 72(3) (2010): 395-400.
[74] Kharlamova, T., et al. Silica-supported silver catalysts modified by cerium/manganese oxides for total oxidation of formaldehyde. Applied Catalysis A: General 467(0) (2013): 519-529.
[75] Shi, R., Wang, F., Mu, X., Li, Y., Huang, X., and Shen, W. MgO-supported Cu nanoparticles for efficient transfer dehydrogenation of primary aliphatic alcohols. Catalysis Communications 11(4) (2009): 306-309.
[76] Di Cosimo, J.I., Díez, V.K., Xu, M., Iglesia, E., and Apesteguía, C.R. Structure and Surface and Catalytic Properties of Mg-Al Basic Oxides. Journal of Catalysis 178(2) (1998): 499-510.
[77] Pestryakov, A.N. and Davydov, A.A. Active electronic states of silver catalysts for methanol selective oxidation. Applied Catalysis A: General 120(1) (1994): 7-15.
[78] Pestryakov, A.N. and Davydov, A.A. Study of supported silver states by the method of electron spectroscopy of diffuse reflectance. Journal of Electron Spectroscopy and Related Phenomena 74(3) (1995): 195-199.
[79] Bogdanchikova, N.E., Dulin, M.N., Davydov, A.A., and Anufrienko, V.F. Diffuse reflectance electron spectroscopic study of the state of silver clusters on SiO2. Reaction Kinetics & Catalysis Letters 41(1) (1990): 73-78.
[80] Pestryakov, A.N., Bogdanchikova, N.E., and Knop-Gericke, A. Alcohol selective oxidation over modified foam-silver catalysts. Catalysis Today 91–92(0) (2004): 49-52.
[81] Pestryakov, A.N. Modification of silver catalysts for oxidation of methanol to formaldehyde. Catalysis Today 28(3) (1996): 239-244.
[82] Zhang, L., Zhang, C., and He, H. The role of silver species on Ag/Al2O3 catalysts for the selective catalytic oxidation of ammonia to nitrogen. Journal of Catalysis 261(1) (2009): 101-109.
[83] Chen, D., et al. Comparative studies of silver based catalysts supported on different supports for the oxidation of formaldehyde. Catalysis Today 175(1) (2011): 338-345.
[84] Kim, Y.-C., Park, N.-C., Shin, J.-S., Lee, S.R., Lee, Y.J., and Moon, D.J. Partial oxidation of ethylene to ethylene oxide over nanosized Ag/α-Al2O3 catalysts. Catalysis Today 87(1–4) (2003): 153-162.
[85] Min, B.K. and Friend, C.M. Heterogeneous gold-based catalysis for green chemistry: Low-temperature CO oxidation and propene oxidation. Chemical Reviews 107(6) (2007): 2709-2724.
[86] Henzler, M. LEED-investigation of step arrays on cleaved germanium (111) surfaces. Surface Science 19(1) (1970): 159-171.
[87] Van Hove, M.A. and Somorjai, G.A. A new microfacet notation for high-Miller-index surfaces of cubic materials with terrace, step and kink structures. Surface Science 92 (1980): 489-518.
[88] Mom, R.V., Hahn, C., Jacobse, L., and Juurlink, L.B.F. LEED analysis of a nickel cylindrical single crystal. Surface Science 613 (2013): 15-20.

[89] Ortega, J.E., Corso, M., Abd-el-Fattah, Z.M., Goiri, E.A., and Schiller, F. Interplay between structure and electronic states in step arrays explored with curved surfaces. Physical Review B 83(8) (2011): 085411.
[90] Klaua, M. and Madey, T.E. The adsorption of H_2O on clean and oxygen-dosed silver single crystal surfaces. Surface Science 136(1) (1984): L42-L50.
[91] Stuve, E.M., Madix, R.J., and Sexton, B.A. The adsorption and reaction of H2O on clean and oxygen covered Ag(110). Surface Science 111(1) (1981): 11-25.
[92] Bange, K., Madey, T.E., Sass, J.K., and Stuve, E.M. The adsorption of water and oxygen on ag(110) - a study of the interactions among water-molecules, hydroxyl-groups, and oxygen-atoms. Surface Science 183(3) (1987): 334-362.
[93] Morgenstern, K. Scanning tunnelling microscopy investigation of water in submonolayer coverage on Ag(1 1 1). Surface Science 504(0) (2002): 293-300.
[94] Morgenstern, K. and Nieminen, J. Intermolecular bond length of ice on Ag(111). Physical Review Letters 88(6) (2002).
[95] Michaelides, A. and Morgenstern, K. Ice nanoclusters at hydrophobic metal surfaces. Nature Materials 6(8) (2007): 597-601.
[96] Mehlhorn, M., Simic-Milosevic, V., Jaksch, S., Scheier, P., and Morgenstern, K. The influence of the surface state onto the distance distribution of single molecules and small molecular clusters. Surface Science 604(19-20) (2010): 1698-1704.
[97] Morgenstern, M., Michely, T., and Comsa, G. Anisotropy in the adsorption of H2O at low coordination sites on Pt(111). Physical Review Letters 77(4) (1996): 703-706.
[98] Smoluchowski, R. Anisotropy of the Electronic Work Function of Metals. Phys. Rev. 60 (1941): 661-674.
[99] Avouris, P., Lyo, I.W., and Molinasmata, P. STM studies of the interaction of surface-state electrons on metals with steps and adsorbates. Chemical Physics Letters 240(5-6) (1995): 423-428.
[100] Heidorn, S. and Morgenstern, K. Spatial variation of the surface state onset close to three types of surface steps on Ag(111) studied by scanning tunnelling spectroscopy. New Journal of Physics 13 (2011).
[101] Scipioni, R., Donadio, D., Ghiringhelli, L.M., and Delle Site, L. Proton Wires via One-Dimensional Water Chains Adsorbed on Metallic Steps. Journal of Chemical Theory and Computation 7(9) (2011): 2681-2684.
[102] Michaelides, A., Ranea, V.A., de Andres, P.L., and King, D.A. General model for water monomer adsorption on close-packed transition and noble metal surfaces. Physical Review Letters 90(21) (2003): 216102.
[103] Ranea, V.A., Michaelides, A., Ramirez, R., Verges, J.A., de Andres, P.L., and King, D.A. Density functional theory study of the interaction of monomeric water with the Ag{111} surface. Physical Review B 69(20) (2004).
[104] Kolb, M.J., Calle-Vallejo, F., Juurlink, L.B.F., and Koper, M.T.M. Density Functional Theory Study of Adsorption of H2O, H, O and OH on stepped platinum surfaces. Journal of Chemical Physics accepted (2014).

APPENDIX

APPENDIX A

CALIBRATION CURVE OF PHASE PERCENT

The calibration curves of chi phase weight percent in alumina catalysts derived from the quantitative XRD of physical mixtures between pure γ- alumina, χ- alumina (determination from area of XRD peak at 43º) with various contents.

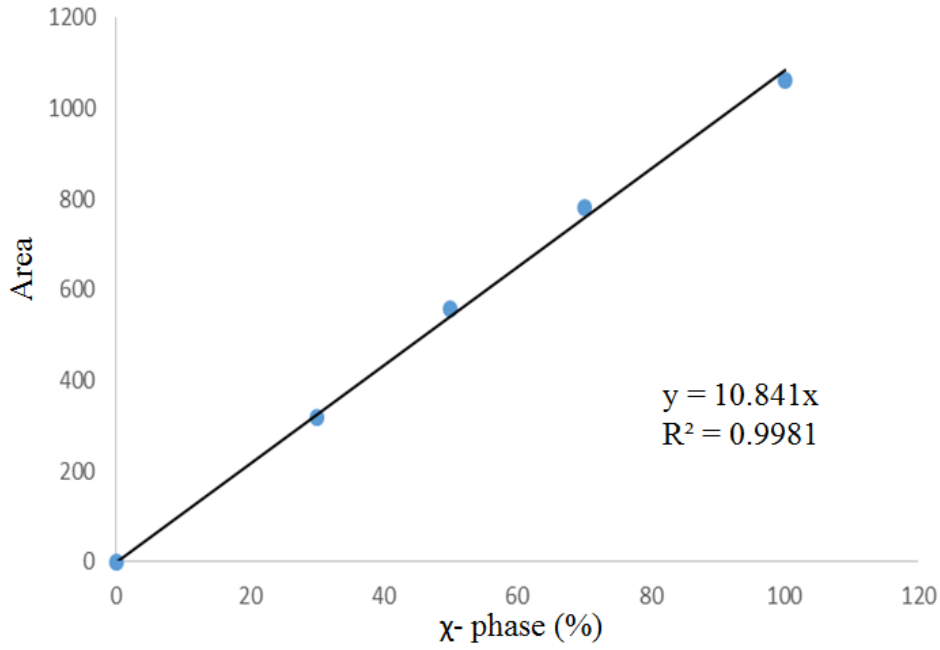

Figure A.1 The calibration curve of chi phase percent in alumina.

APPENDIX B
CALCULATION FOR CATALYST PREPARATION

Calculation of silver-lithium loading

Preparations of AgLi-Al_2O_3 by the incipient wetness impregnation method are shown as follows

Reagent: - Silver (I) nitrate ($AgNO_3$)

Molecular weight = 169.87 g/mol

Siver (Ag), Atomic weight = 107.88 g/mol

- Lithium nitrate ($LiNO_3$)

Molecular weight = 68.94 g/mol

- Aluminium oxide (Al_2O_3)

Molecular weight = 102 g/mol

- Support: - Mixed-phase alumina

- γ -phase alumina

- χ -phase alumina

The ratio of silver and lithium used for incipient wetness impregnation method are shown as follows

$$\frac{Al}{Ag} = \frac{40}{1} \quad \text{And} \quad \frac{Al}{Li} = \frac{15}{1}$$

Based on 1.9 g of aluminium oxide used, the composition of the catalyst will be as follows:

Aluminium oxide	=	1.90 g	
Al_2O_3	=	$\frac{1.90}{102}$ mol	= 0.01863 mol
Al	=	0.01863x2 mol	= 0.0373 mol

Silver was prepared from Silver (I) nitrate

Silver (I) nitrate required	=	$\frac{1}{40}$ x 0.0373 mol	= 9.325×10^{-4} mol
	=	$9.325 \times 10^{-4} \times 169.87$ g	= 0.1584 g

Lithium was prepared from Lithium (nitrate

Lithium nitrate required	=	$\frac{1}{15}$ x 0.0373 mol	= 2.487×10^{-3} mol
	=	$2.487 \times 10^{-3} \times 68.94$ g	= 0.1714 g

Since the pore volume of aluminium oxide support is 1.0287 ml/g. Thus, the total volume of impregnation solution which must be used is 1.954 ml for aluminium oxide by the requirement of incipient wetness impregnation method, the de-ionized water is added until equal pore volume for dissolve silver (I) nitrate and lithium nitrate.

APPENDIX C
CALCULATION OF PARTIAL PRESSURE OF ETHANOL

Set the partial vapor pressure of the reactants to the requirement by adjusting the temperature of saturator according to the Antoine equation;

$$\log P = A - \frac{B}{(T + C)}$$

The variable in Antoine equation are define as follow ;

P = vapor pressure of ethanol, mmHg

T = temperature, ˚C

A = 8.04494

B = 1554.3

C = 222.65

The saturator is performed at 45 ˚C

.

$$\log P = 8.04494 - \frac{1554.3}{(45 + 222.65)}$$

P = 172.87 mmHg

The pressure of argon gas was adjusted to 2 bar (2.0x760 = 1520 mmHg)

$$\text{Mole fraction of ethanol} = \frac{172.87}{1520 + 172.87}$$

$$= 0.1021\%$$

APPENDIX D

CALIBRATION CURVES

This appendix exhibited calibration curves of reactant and products in ethanol dehydration reaction. There curves were used calculation of composition. The ethanol is reactant while the ethylene is main product but, the diethylether and acetaldehyde are byproducts of this reaction.

The capillary column DB-5 of flame ionization detector (FID), gas chromatography Shimadzu model FID 14B and TCD 8Awas used to analyze the concentration of ethanol, ethylene, diethylether and acetaldehyde. The conditions uses in GC are presented in **Table B.1**

Table B. 1 Conditions use in GC-FID-14B and TCD 8A.

Parameters	Condition
Width	5
Slope	100
Drift	0
Min.area	300
T.DBL	1000
Stop time	12 min
Atten	2
Speed	3
Method	Normalization
SPL.WT	100
IS.WT	1

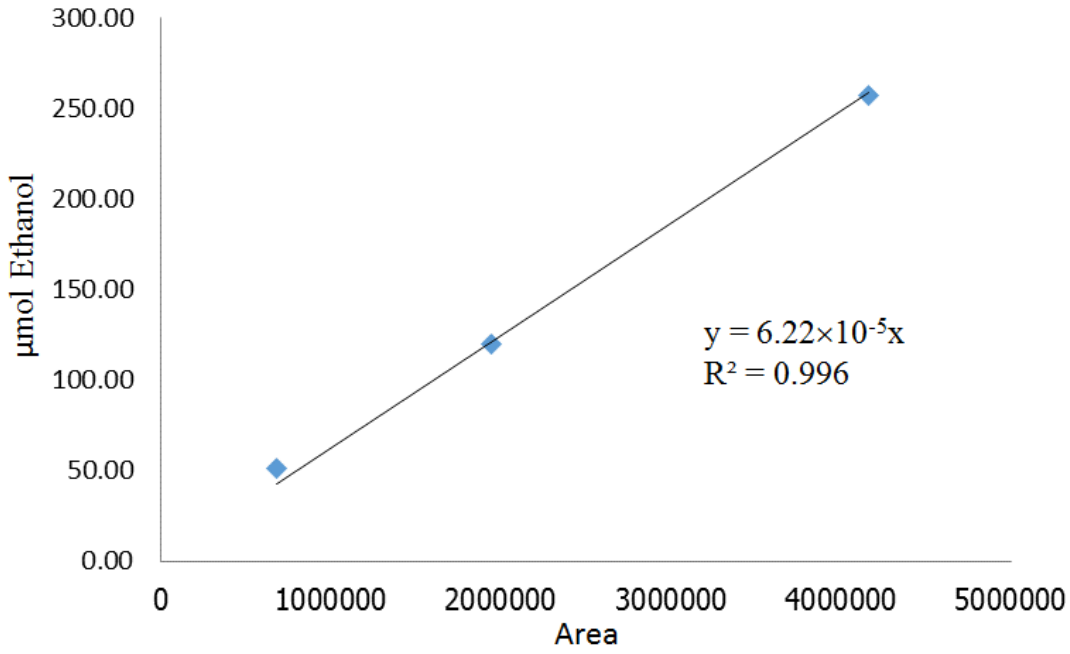

Figure D.1 The calibration curve of ethanol.

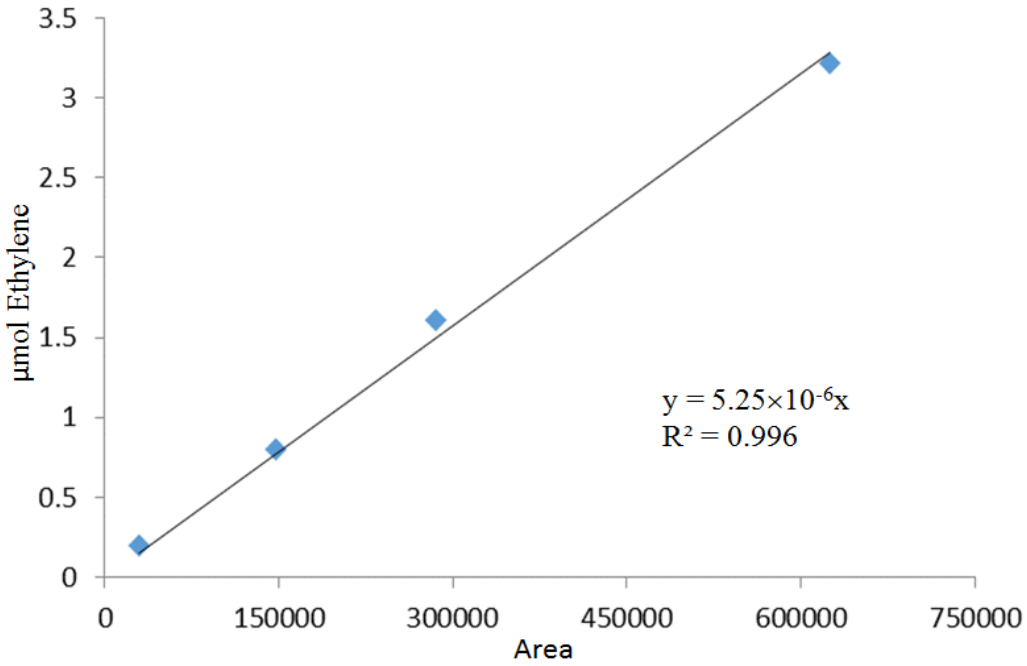

Figure D.2 The calibration curve of ethylene.

.

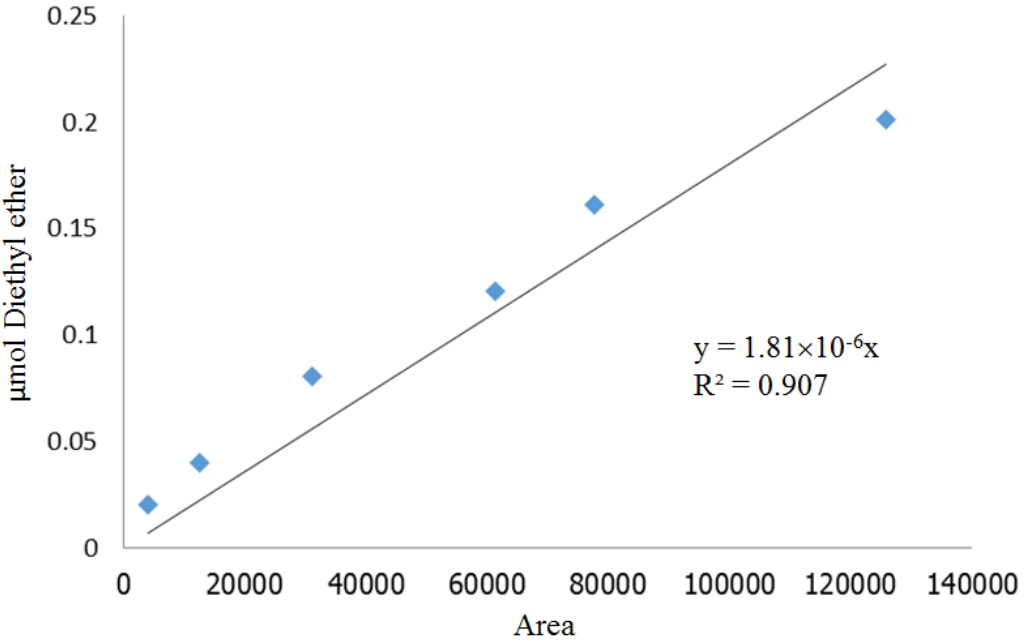

Figure D.3 The calibration curve of diethyl ether.

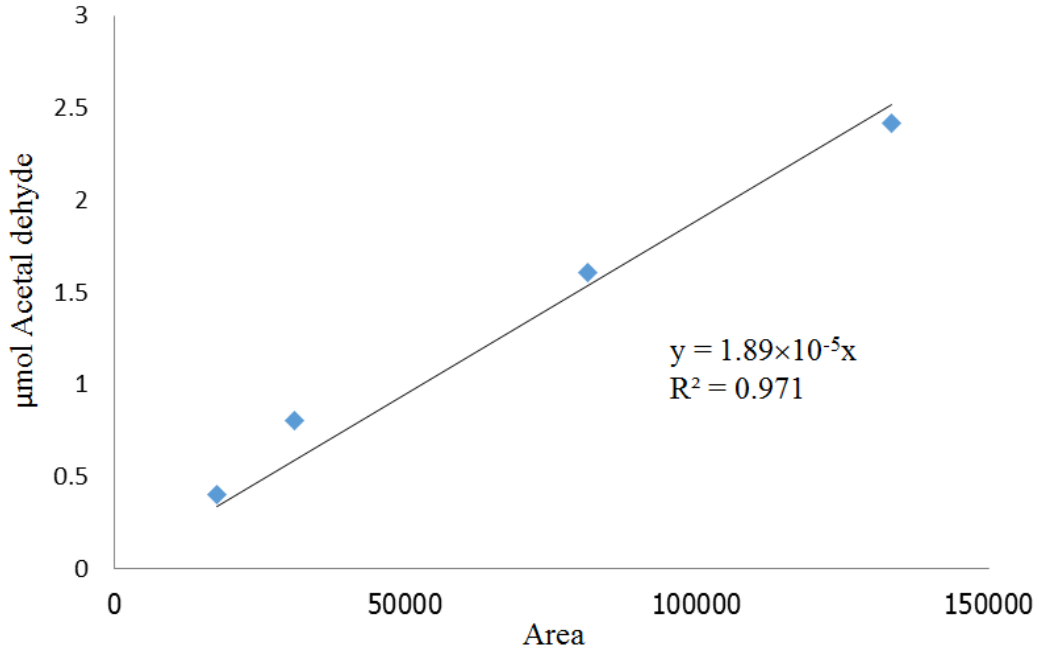

Figure D.4 The calibration curve of acetaldehyde

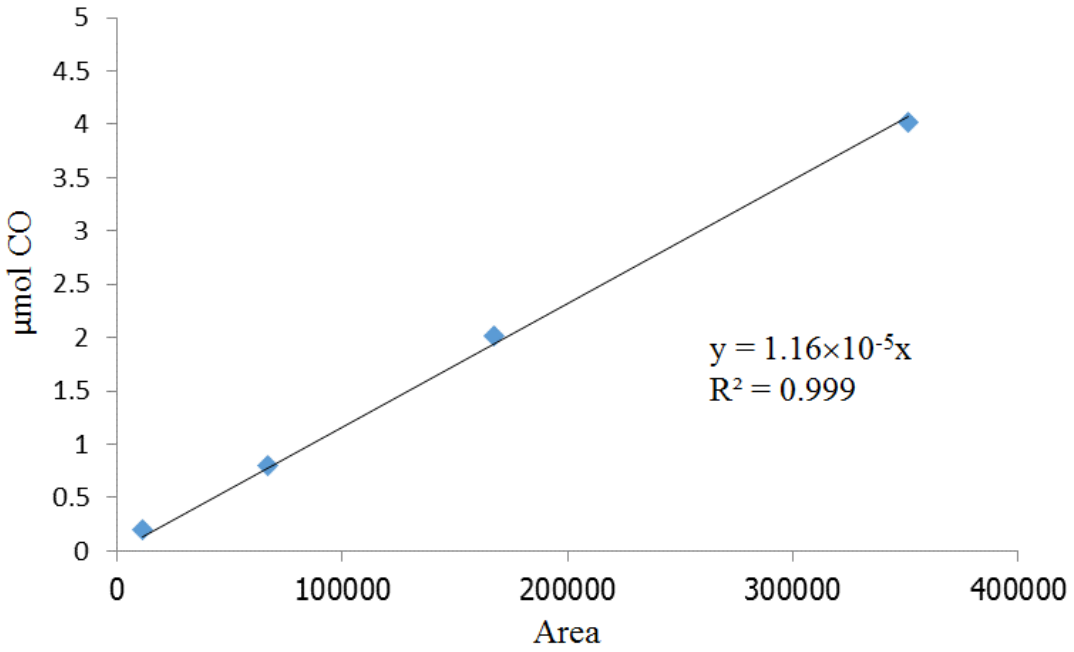

Figure D.5 The calibration curve of carbon monoxide

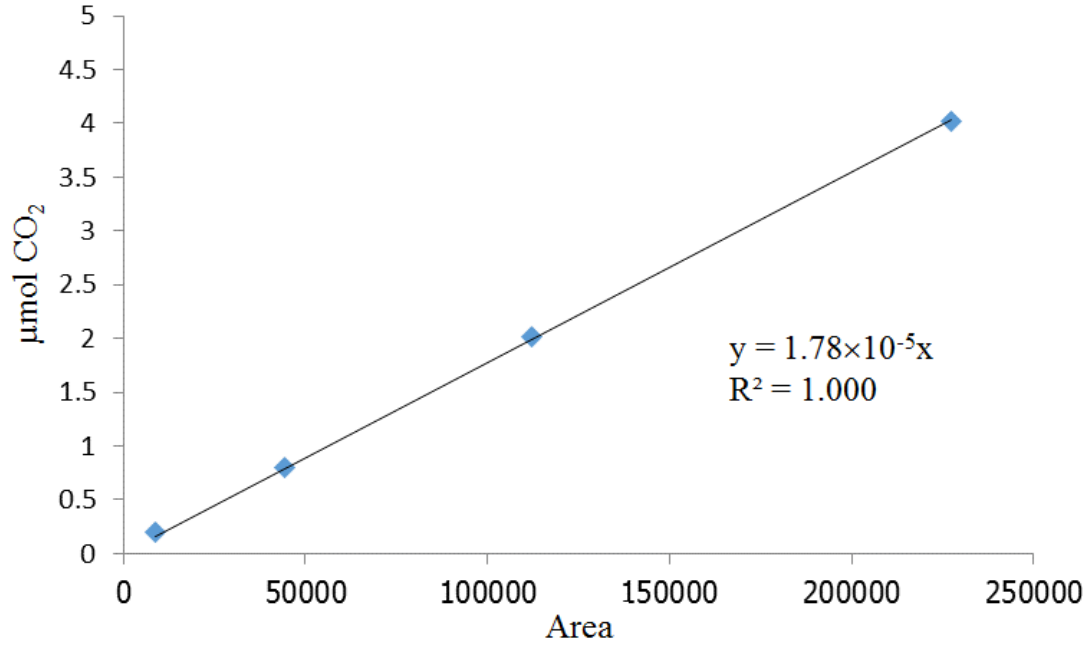

Figure D.6 The calibration curve of carbon dioxide

APPENDIX E
CALCULATION OF ETHANOL CONVERSION AND SELECTIVITY

The conversion of reactant and selectivity of products exhibited the performance of catalyst. Then, there were used demonstrated the catalytic activity for dehydration and oxidative dehydrogenation of ethanol.

Ethanol conversion

The ethanol conversion was assigned that mole of ethanol converted with respect to ethanol in feed:

$$Ethanol\ conversion\ (mole\%) = \frac{[mole\ of\ ethanol\ in\ feed - mole\ of\ ethanol\ in\ product] \times 100}{mole\ of\ ethanol\ in\ feed}$$

Selectivity of product

The product selectivity is assigned that mole of product (A) formed with respect to mole of total products:

$$\text{Selectivity of A (\%)} = \frac{\text{mole of product Ax100}}{\text{mole of total products}}$$

APPENDIX F
CALCULATION OF ACIDITY

Calculation of total acidity.

Total acidity is calculated from the NH_3-TPD profiles as the following step.

The NH_3-TPD profiles:

- The area of the NH_3-TPD profiles of the sample = A
- The mole of NH_3 was calculated from the calibration curve of NH_3 as formula:

The mole of NH_3 of the sample = $0.294 \times A$ mmole.

- Amount of sample = B g.

$$\text{The total acidity of sample} = \frac{\text{mmole of } NH_3 \text{ of the sample}}{\text{Amount of dry catalyst}}$$

$$= \frac{0.294 \times A}{B} \quad \text{mmol } NH_3\text{/g catalyst}$$

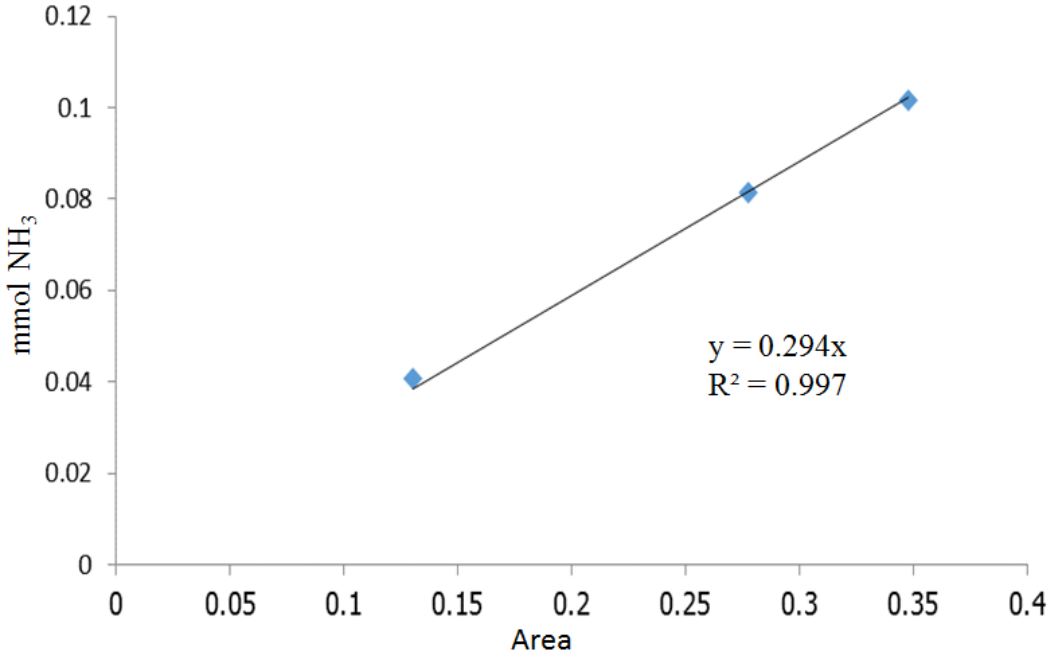

Figure F.1 The calibration curve of ammonia from Micromeritics Chemisorp 2750

APPENDIX G
CALCULATION OF BASICITY

Calculation of total basicity.

Total basicity is calculated from the CO_2-TPD profiles as the following step.

The CO_2-TPD profiles:

- The area of the CO_2-TPD profiles of the sample = A
- The mole of CO_2 was calculated from the calibration curve of CO_2 as formula:

The mole of CO_2 of the sample = $0.0176 \times A$ mmole.

- Amount of sample = B g.

$$\text{The total basicity of sample} = \frac{\text{mmole of } CO_2 \text{ of the sample}}{\text{Amount of dry catalyst}}$$

$$= \frac{0.0176 \times A}{B} \quad \text{mmol } CO_2\text{/g catalyst}$$

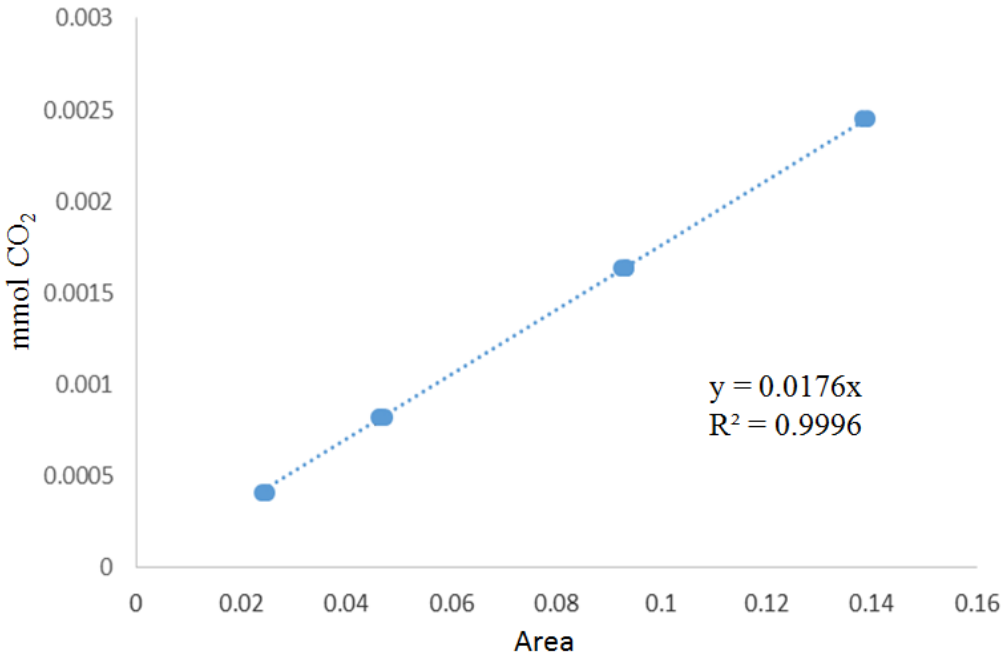

Figure G.1 The calibration curve of carbon dioxide from Micromeritics Chemisorp 2750

APPENDIX H
LIST OF PUBLICATIONS

1. Jakrapan Janlamool, Dima Bashlakov, Otto Berg, Piyasan Praserthdam, Bunjerd Jongsomjit and Ludo B.F. Juurlink. Desorption of Water from Distinct Step Types on a Curved Silver Crystal. 2014, Molecules 19, 10845-10862 (Impact factor = 2.095, Q3)

2. Jakrapan Janlamool, Piyasan Praserthdam and Bunjerd Jongsomjit. The effect of phase composition between nanocrystalline χ- and γ-alumina on the catalytic ethanol dehydration under review in Applied Catalysis A: General (Impact factor = 3.674, Q1)

3. Jakrapan Janlamool, and Bunjerd Jongsomjit Oxidative dehydrogenation of ethanol over Ag-Li-Al_2O_3 catalysts with different phases of alumina will be submitted to Catalysis Communications (Impact factor = 3.320, Q2)

VITA

Mr. Jakrapan Janlamool was born on October 30th, 1983 in Pichit province, Thailand. He finished high school from Pichit Pittayakom School in 2002. He received the bachelor's degree of General science and Biochemistry from Faculty of Science, Kasetsart University in 2006 and 2007, respectively. He received the master's degree of Chemical Engineering from Faculty of Engineering, Chulalongkorn University in 2010. He continued his doctoral's study at Department of Chemical Engineering, Faculty of Engineering, Chulalongkorn University in July, 2010.